

## Use Authorization

In presenting this dissertation in partial fulfillment of the requirements for an advanced degree at Idaho State University, I agree that the Library shall make it freely available for inspection. I further state that permission to download and/or print my dissertation for scholarly purposes may be granted by the Dean of the Graduate School, Dean of my academic division, or by the University Librarian. It is understood that any copying or publication of this dissertation for financial gain shall not be allowed without my written permission.

Signature \_\_\_\_\_

Date \_\_\_\_\_

Characterizing Basin and Range Fault Activity  
near Challis, Idaho, using Novel Remote Sensing Techniques

By

Ashley Shields

A thesis submitted in partial fulfillment of the requirements for a  
Master of Science in Geographic Information Science.  
Idaho State University  
Fall 2017

To the Graduate Faculty:

The members of the committee appointed to examine the thesis of Ashley Shields find it satisfactory and recommend that it be accepted.

---

Donna Delparte, PhD, Assistant Professor,  
Department of Geosciences, Idaho State University  
Major Advisor

---

David Pearson, PhD, Assistant Professor  
Department of Geosciences, Idaho State University  
Major Advisor

---

H. Carrie Bottenberg, PhD, Assistant Lecturer  
Department of Geosciences, Idaho State University  
Allied Graduate Faculty

---

John Edwards, PhD, Assistant Professor  
Informatics and Computer Science, Idaho State University  
Graduate Faculty Representative

Date: \_\_\_\_\_

## Table of Contents

List of Figures .....	vi
List of Tables .....	vii
Abstract .....	viii
Chapter 1: Introduction .....	1
Overview .....	1
Research Goals and Objectives .....	5
Broader Impacts .....	6
Chapter 2: Literature Review .....	7
Geologic Background.....	7
Basin and Range Development.....	7
Basin and Range Fault Segmentation and Generalized Geometries .....	8
Lost River Fault System .....	9
Seismicity along the Lost River Fault .....	10
Review of Remote Sensing Approaches for Geological Mapping.....	11
Multiscale Data Sources .....	11
Radar Data Analysis .....	14
Multispectral Classification and Geologic Unit Mapping .....	16
Chapter 3: Remote Sensing Applications for Geologic Analyses .....	24
Introduction .....	24
Methods.....	28
Estimating Study Area Boundaries based on Seismicity.....	28
Data Sources .....	29
Terrain Based Geological Feature Detection.....	30
Multispectral Data Classification Approaches for Geologic Mapping.....	31
Results .....	38
Candidate Fault Locations .....	38
Topographic Analysis Results .....	39
Multispectral Analysis Results .....	41
Field Results .....	69
Discussion .....	69
Remote Sensing .....	69
Study Limitations.....	74

Geological Explanations .....	76
Recommendations for Future Research.....	77
Chapter 4: Geologic Scouting Using Unmanned Aircraft Systems .....	79
Introduction .....	79
Methods.....	82
Results .....	86
Discussion .....	89
Chapter 5: Recommendations for Future Work.....	94
Chapter 6: Conclusions .....	98
References.....	100

## List of Figures

Figure 1: Study areas north and south of Challis, Idaho, near the Lost River fault system	2
Figure 2: A comparison of the northern surface expression of the Lost River fault system and the seismic cluster of interest .....	3
Figure 3: Schematic diagram of a horsetail fault. ....	4
Figure 4: Two study areas to search for evidence of an active fault.....	38
Figure 5: Elevation information for the western study area.....	39
Figure 6: Elevation information for the eastern study area.....	40
Figure 7: Brightness values of the radar signal received by the Sentinel-1 sensor.....	41
Figure 8: WorldView-2 false color composite image of the western study area.....	42
Figure 9: WorldView-2 false color composite image of the eastern study area .....	43
Figure 10: WorldView New Iron Index of the western study area .....	44
Figure 11: WorldView New Iron Index of the eastern study area .....	45
Figure 12: WorldView Non-Homogeneous Feature Index of the western study area .....	46
Figure 13: WorldView Non-Homogeneous Feature Index of the eastern study area .....	47
Figure 14: WorldView-2 Improved Vegetation Index of the western study area.....	48
Figure 15: WorldView Improved Vegetation Index of the eastern study area .....	49
Figure 16: Optimized Soil Adjusted Vegetation Index of the western study area.....	50
Figure 17: Optimized Soil Adjusted Vegetation Index of the eastern study area .....	50
Figure 18: ASTER Maximum Likelihood Analysis (MLA) classification of the western study area .....	53
Figure 19: ASTER Maximum Likelihood Analysis (MLA) classification of the eastern study area .....	54
Figure 20: ASTER Support Vector Machine (SVM) classification of the western study area.....	55
Figure 21: ASTER Support Vector Machine (SVM) classification of the eastern study area .....	56
Figure 22: ASTER Minimum Distance (MD) classification of the western study area ...	57
Figure 23: ASTER Minimum Distance (MD) classification of the eastern study area ....	58
Figure 24: Sentinel-2 Support Vector Machine (SVM) classification of the western study area.....	60
Figure 25: Sentinel-2 Support Vector Machine (SVM) classification of the eastern study area.....	61
Figure 26 (Previous Page): Sentinel-2 Maximum Likelihood Analysis (MLA) classification of the western study area .....	62
Figure 27: Sentinel-2 Maximum Likelihood Analysis (MLA) classification of the eastern study area .....	62
Figure 28: Sentinel-2 Minimum Distance (MD) classification of the western study area	63
Figure 29: Sentinel-2 Minimum Distance (MD) classification of the eastern study area	64
Figure 30: Natural color NAIP imagery of the western study area .....	65
Figure 31: Natural color NAIP imagery of the eastern study area.....	65
Figure 32: NAIP Normalized Difference Vegetation Index of the western study area ....	66
Figure 33: NAIP Normalized Difference Vegetation Index of the eastern study area. ....	67
Figure 34: NAIP decorrelation stretch image of the western study area .....	68
Figure 35: NAIP decorrelation stretch image of the eastern study area .....	69

Figure 36: Map showing the study area for UAS data collection .....	85
Figure 37: The orthophoto produced from the UAS data collection. ....	87
Figure 38: The DSM produced from the UAS data collection. ....	88
Figure 39: The hypothesized fault trace, overlain with the orthophoto result .....	91
Figure 40: The hypothesized fault trace, overlain with the DSM result .....	92
Figure 41: The hypothesized fault trace overlain with 10 m topographic contours.....	93

## List of Tables

Table 1: Band designations for the WorldView-2 sensor .....	17
Table 2: Band designations for the ASTER sensor.....	19
Table 3: Band designations for the Sentinel-2 sensor.....	21
Table 4: Band designations for the NAIP Sensor .....	22
Table 5: Spectral data sources.....	30
Table 6: Band equations applied to ASTER imagery to delineate lithologies and mineralogies. Band designations are defined in Table 2. ....	35
Table 7: Sentinel-2 indices, from Van der Meer et al. (2014) .....	36
Table 8: Results from the ASTER classification confusion matrices .....	51
Table 9: Results from the Sentinel-2 classification confusion matrices .....	58
Table 10: A cumulative overview of the remote sensing results .....	70
Table 11: Comparison of classification accuracies between ASTER and Sentinel-2 results .....	71

## Abstract

The Lost River fault system is part of the northern Basin and Range province. Though its northern mapped trace ends east of Challis, Idaho, a linear cluster of seismicity occurred in 2014-2016 five km to the northwest. This work applied remote sensing methods to evaluate whether there is a previous, unmapped active fault north of Challis responsible for recent seismicity and to determine how the fault system changes toward its northern extent. Preliminary mapping was unable to identify an active fault. However, investigation of a southern study area using an unmanned aircraft system (UAS) identified a fault trace that may represent an unmapped portion of the Lost River fault system. These results suggest that: 1) displacement along the northern trace of the fault system occurs along multiple, lower fault strands; and 2) a blind fault may be responsible for recent seismicity beyond the northern extent of the fault system.

## Chapter 1: Introduction

### Overview

A cluster of increased seismicity from 2014-2016 was identified north of Challis, Idaho, northwest of the mapped traces of active Basin and Range normal faults (Figure 1) (Stickney, 2016). There is no evidence for an anthropogenic cause of the seismicity, such as active mining or fracking efforts. This seismicity has a linear distribution with a northwest trend that is similar to that of the Lost River fault (Figure 2). This seismicity may result from northwestward growth of the Basin and Range province, but there is no prior evidence of recent (i.e., <10 ka) surface rupture in this area. The seismicity and possible presence of an unidentified active fault(s) here have implications for the seismic hazard for the community of Challis and for our understanding of how extensional deformation propagates along-strike.

Historic earthquake activity along nearby Basin and Range faults includes the  $M_w$  6.9 magnitude event at Borah Peak in 1983, which produced a 36 km-long surface rupture, ground breakage as wide as 140 m, and scarps reaching nearly 5 m high (Crone and Haller, 1991; Payne et al., 2004). Aftershocks continued after the Borah Peak event, including the  $M_w$  5.8 magnitude Devil's Canyon aftershock (Payne et al., 2004). The linear trend of the recent seismicity and its apparent alignment with the northwestern trace of the Lost River fault zone support the hypothesis that this seismicity may be related to an unmapped strand of the Lost River fault, hinting that this is an actively developing fault system resulting from northwestward propagation of the Basin and Range province beyond its known extent. If this seismicity reflects activity along a branch at the northern termination of the fault such as a horsetail fault (Figure 3), it is

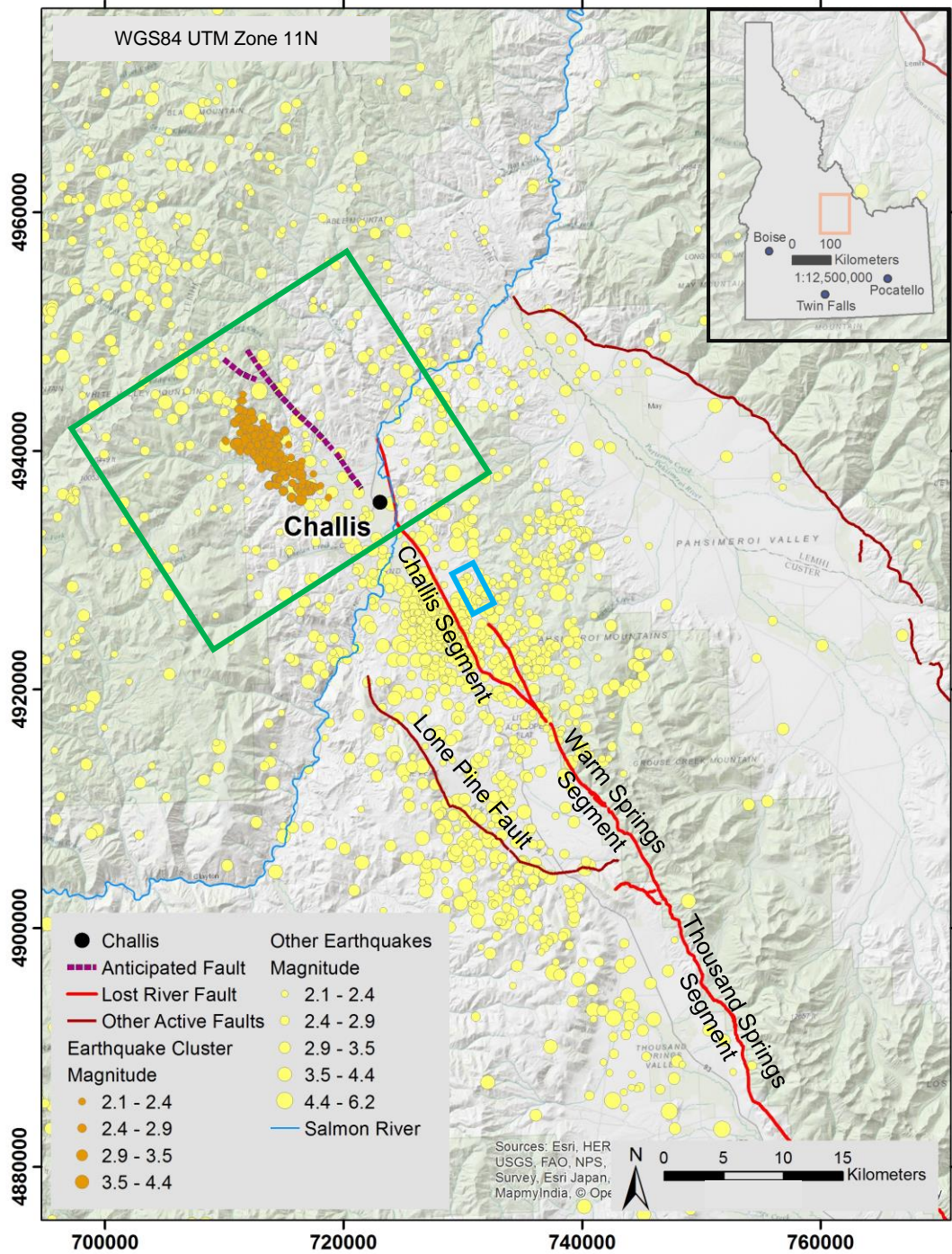


**Figure 1:** Study areas north and south of Challis, Idaho, near the Lost River fault system. The northern area of interest is highlighted by a green box and the southern area of interest is highlighted by a blue box. (WGS1984 UTM 11N)

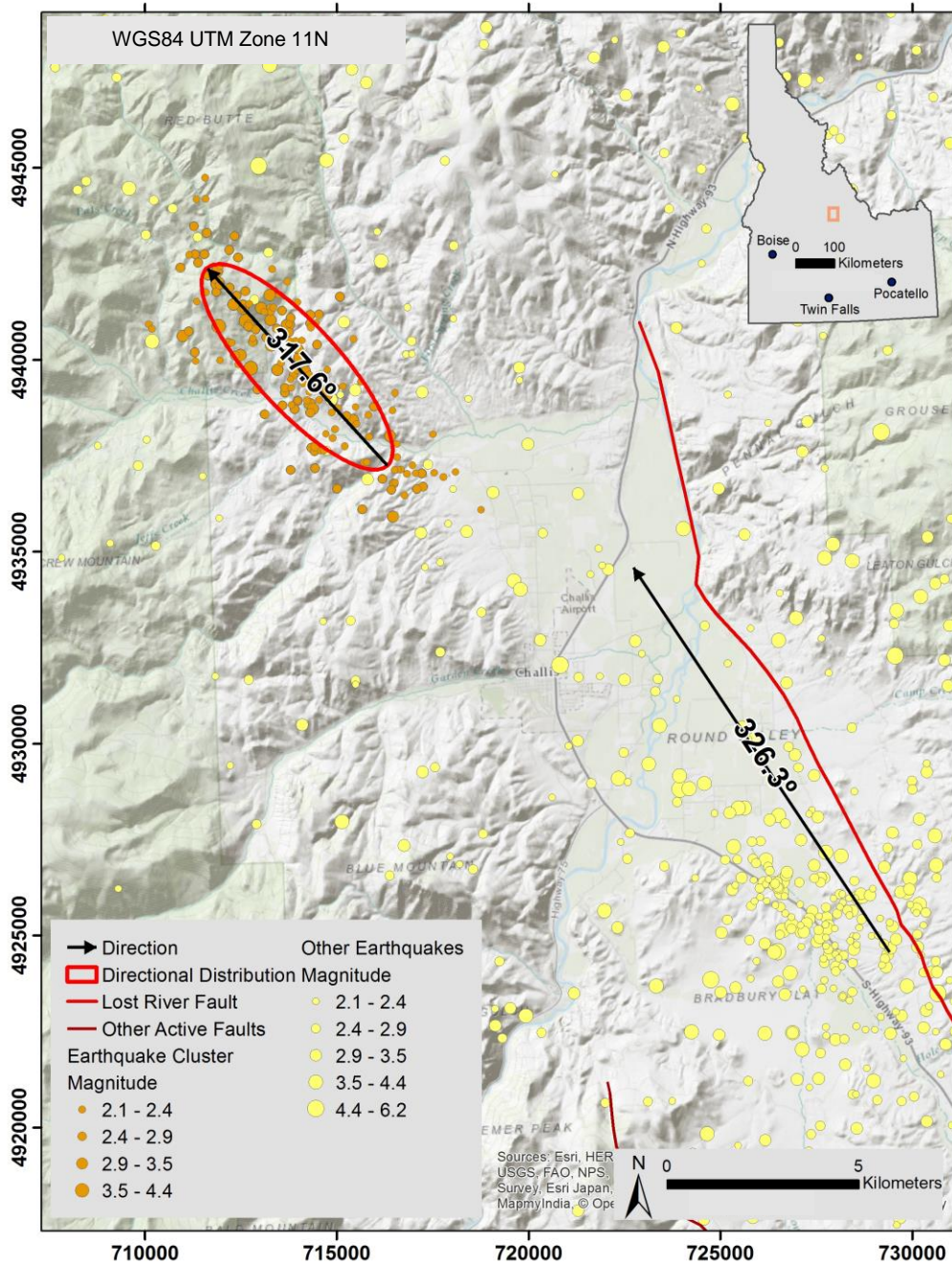


**Figure 2:** A comparison of the northern surface expression of the Lost River fault system and the seismic cluster of interest, showing an azimuthal difference of less than 9°. The mean trend of the northern half of the Lost River fault has an azimuth of 326.3°. The major axis of the directional distribution ellipse for the seismic cluster of interest has an azimuth of 317.6°.

hypothesized that there may have been prehistoric surface rupture or other evidence of older fault activity (Anders and Schlische, 1994). Although the northern extent of the Basin and Range province is thought to terminate southeast of this cluster of seismicity, the Lost River fault may continue farther to the north than it is currently mapped (Susong et al., 1990; Anders and Schlische, 1994; Payne et al., 2004).

There are several hypotheses about why Basin and Range faults may not continue farther west, including the possibility of a relatively strong crust due to the presence of



**Figure 3:** Schematic diagram of a horsetail fault, splaying toward its terminus (Fossen, 2010).

intrusions and metamorphism in the Idaho batholith (McCaffrey et al., 2013). The occurrence of this seismicity calls into question the presence of a barrier to northwestward propagation of Basin and Range faults. By constraining the geometry of faults at the northwestern boundary of the Basin and Range, we will determine if the fault associated with this

seismicity is an extension of the Basin and Range province, north of the Salmon River.

Development of the northeastern Basin and Range province is thought to be partially driven by gravitational potential energy that resulted from over thickened crust from prior orogenic events (Colgan, 2013). It has also been noted that the development of the Basin and Range province to the northeast is temporally linked to the migration of the Yellowstone hotspot, located just beyond the northeastern extent of Basin and Range faulting (Rodgers et al., 2002; Pierce and Morgan, 2009). If recent seismicity is indeed an expression of Basin and Range normal faulting, then the province must extend beyond

the mapped boundary, north of the Lost River fault's proposed termination, and into what is known as the Trans-Challis fault system (Bennett, 1986; Payne et al., 2004).

The large spatial extent of the Lost River fault poses a challenge for traditional geological mapping on foot. Remote sensing is a proven technique to supplement traditional field-based mapping, improving the efficiency of lithologic and structural mapping. Classification techniques such as maximum likelihood analysis and support vector machines applied to large spatial areas can assist in differentiating lithologic compositions and effectively assist in the creation of maps depicting surficial exposures of lithologic units and deformational features. Geometric characteristics of faults, such as strike and dip, can be extracted and quantified from looking at interactions between the topography and the fault trace (Bemis et al., 2014; Chen et al., 2015).

## Research Goals and Objectives

The first research question that this thesis will investigate is: is there any surface expression of a fault associated with the recent seismicity that we can identify using remote sensing techniques? We hypothesize that there is a surficial expression of faulting from prior activity along the structure responsible for the recent seismicity that is identifiable using remote sensing classification techniques. This work seeks to answer this question using a multiscale approach that identifies lithologic composition and lineations in remotely sensed imagery, including DigitalGlobe's WorldView-2, NASA's Advanced Spaceborne Thermal Emission and Reflection Radiometer (ASTER), and data acquired using an unmanned aircraft system (UAS) (Rowan and Mars, 2003; Ruisi et al., 2011; Bemis et al., 2014; Chen et al., 2015). The US Geological Survey's National

Elevation Dataset (NED) and radar data (European Space Agency's Sentinel-1) were processed for the entire area so that the topography (e.g. terrain roughness, cliffs, and linear depressions) could be compared to the imagery, mapped lithologies, geologic structures (Gesch et al., 2002; Guerrieri et al., 2010). Satellite imagery was processed and classified using principal component analysis and supervised classifications. Maximum likelihood analysis, support vector machine, and minimum distance algorithms are three types of supervised classification algorithms that can be applied to the imagery to assess patterns (Grebby, 2011).

The second research question that this thesis investigates pertains to an area southeast of Challis (Figure 1), where we hypothesize that an unmapped trace of the Lost River fault system is located. For this portion of the work, we investigate the applicability of a low cost unmanned aircraft system platform and describe the methods used to collect, process, and interpret the data. Based on regional geology, and data collected during field observations and processed UAS data, as well as the lithologic and structural classification results from processing remotely sensed data, this thesis investigates evidence for the continuity of the eastern strand of the Challis segment of the Lost River fault system, beyond its current mapped terminus. This information contributes to a better understanding of the Lost River fault system and suggests a workflow for conducting geologic scouting using the Parrot Disco delta wing UAS platform.

### Broader Impacts

Challis is located in Custer County, Idaho and has a population of 4,087 and a population density of 0.83 persons per square mile (United States Census Bureau, 2015).

Evaluating the forces that influence the development and extent of the northeastern Basin and Range province, as well as seismic hazards, could have implications for safe and sustainable development of the community of Challis and nearby infrastructure, such as the Challis Airport and US Highway 93. The project aims to develop and implement new techniques in remote sensing and GIS analytics to investigate the cause of this cluster of seismicity as well as how the northeastern Basin and Range province grows in spatial extent. Possible faults are interpreted using imagery obtained via remote sensing platforms, such as satellite-based sensors and unmanned aircraft systems (UAS). Linear features, observed in the processed data, may represent surface deformation (e.g. surface displacement or vegetation anomalies) and lead to the implementation and development of new remote sensing workflows for lithologic discrimination and geologic structure detection.

## Chapter 2: Literature Review

### Geologic Background

#### Basin and Range Development

The Basin and Range is a tectonic province that consists of a system of predominantly normal faults occurring from northeastern Idaho and western Montana to Mexico (Bennett et al., 2003; Dickinson, 2006). The Basin and Range province has developed from 16 Ma through the present, and is progressing to the northeast on both the north and south margins of the Snake River Plain, at the same rate as the migration of rhyolitic volcanic centers associated with the Yellowstone hotspot (Rodgers et al., 2002). Surface ruptures associated with Basin and Range faulting have been previously

delineated elsewhere with the use of remote sensing techniques (Dadon et al., 2011; Bemis et al., 2014; Chen et al., 2015).

The propagation mechanisms of the northern extent of the Basin and Range province are not entirely understood, but are proposed to be the result of a combination of influence from the migration of the Yellowstone hotspot and the gravitational collapse of the overthickened crust that developed during the Mesozoic Sevier orogeny (Rodgers et al., 2002; Colgan, 2013). Regional GPS velocities of the region support a clockwise rotation of the regions surrounding the batholith: the area west of the Idaho batholith is undergoing shortening, whereas the region on the eastern side of the batholith is undergoing extension (Payne et al., 2012; McCaffrey et al., 2013). The batholith may be more strongly connected to the mantle than these surrounding regions and so the gravitational collapse of the overthickened crustal material in the area migrates westward around the batholith (Colgan, 2013; McCaffrey et al., 2013).

#### Basin and Range Fault Segmentation and Generalized Geometries

Normal faults are often segmented along-strike, with segments typically around 20-25 km long; longer segments correspond to thicker crust (Gawthorpe and Leeder, 2000). The boundaries between these types of segments typically are characterized by an increased occurrence of small faults (similar to what is portrayed in the horsetail fault in Figure 3) rather than a single strand at their terminus, where these smaller faults accommodate stress changes between segments (Gawthorpe and Leeder, 2000; Payne et al., 2004). Segmented faults are associated with episodic fault growth, which results in clustered earthquakes as segments rupture. This has been previously described in the study area by

Payne et al. (2004) and is what we hypothesize is occurring to produce the earthquakes shown in Figure 1.

In the proximity of the Snake River Plain, Basin and Range faults dip between 25-60 degrees west or southwest and are categorized by either (1) widely spaced and segmented half graben containing basins up to 3.5 km deep or (2) closely spaced half graben with little offset and without basins (Rodgers et al., 2002). The northwest-striking Basin and Range normal faults in east-central Idaho result from northeast-southwest crustal extension.

### Lost River Fault System

North of the Snake River Plain, the Basin and Range province is characterized by the Lost River, Lemhi, and Beaverhead faults, which are each approximately 120 km long (Rodgers et al., 2002). The Lost River fault is composed of at least six segments, each ranging in length from 15-30 km, with the central segments being the most active; the central segment has an overall dip of approximately 50 degrees (Susong et al., 1990; Link and Janecke, 1999; Rodgers et al., 2002). The northwestern mapped extent of the Lost River fault system consists of the southern Warm Spring segment and northern Challis segment (Figure 1) (Payne et al., 2004). Subparallel to these two segments but defining the southwestern side of the valley is the northeast-dipping Lone Pine fault (Payne et al., 2004). Together, the northern Lost River fault system and the Lone Pine fault thus define a graben, which is in contrast to any other prominent Basin and Range fault systems in east-central Idaho. The northern segment of the Lost River fault, known as the Challis segment, is composed of at least three parallel strands: the Western, Central, and Eastern strands (Payne et al., 2004).

The northern mapped extent of the Lost River fault system (Challis segment) terminates near Challis, Idaho; the cause of this terminus may be due to the Idaho batholith, an alternative fault system, or deformation may simply become diffuse as stresses are distributed along smaller faults near the fault terminus (Bennett, 1986; Anders and Schlische, 1994; Payne et al., 2004; McCaffrey et al., 2013). Evidence for the effect of the Idaho batholith on Basin and Range extension is supported by a lack of extensional deformation in the batholith as documented by GPS data (McCaffrey et al., 2013). It is also possible that the seismicity is being transferred along an alternate fault system, such as the Trans-Challis fault system or onto a reactivated fault (Bennett, 1986; Payne et al., 2004).

#### Seismicity along the Lost River Fault

Approximately 70 km southeast of the seismic cluster shown in Figure 1, a significant earthquake occurred near Borah Peak. In October of 1983 this earthquake occurred on the Lost River fault, with a magnitude of  $M_w$  6.9, resulting in a surface rupture with a length of 36 km (Crone et al., 1987; Payne et al., 2004; McCaffrey et al., 2013). This earthquake resulted in a series of aftershocks, which interpreted to result from readjustment as seismicity propagated to the northwest (Crone et al., 1987; Susong et al., 1990). Late aftershocks from this earthquake, beginning in August of 1984, known as the Devil's Canyon aftershock sequence, included an event with a magnitude of  $M_L$  5.8, which nucleated at depth between two strands of the Lost River fault, near Challis, Idaho, with a strike similar to the Lost River fault (Payne et al., 2004). Several earthquakes that occurred at the same time as this 1984-1985 aftershock sequence (Payne

et al., 2004) had epicenters that spatially overlap with the 2014-2016 linear seismic cluster of interest shown in Figure 1.

## Review of Remote Sensing Approaches for Geological Mapping

### Multiscale Data Sources

Remotely sensed imagery is acquired from airborne, spaceborne, or unmanned aircraft systems (UAS), resulting in a perspective that cannot be achieved from land-based observations (Matthews, 2008). Geological interpretations are made by combining remotely sensed imagery with topographic information, geological maps, and seismicity data (Chen et al., 2015). The combination of multiscale data sources is applied to infer surficial and subterranean geological components that are used to produce geologic maps, cross sections, and improve our understanding of geologic structures and seismic sources (Dadon et al., 2011; Grebby et al., 2011; Ruisi et al., 2011; Bemis et al., 2014; Chen et al., 2015). This multiscale data approach benefits research because it allows us to identify patterns that can be identified on both regional and small scales and results in a greater diversity of sensors to contribute to analyses (Ben Hamza et al., 2005).

UAS imagery is collected using fixed wing or rotor platforms, which have a range of spatial resolutions from ~3 cm - 12 cm. Fixed wing platforms collect data more efficiently than rotor platforms because they glide at higher altitudes, but the height at which they fly results in data with comparably lower spatial resolution than their rotor counterparts (Remondino et al., 2011; Siebert and Teizer, 2014). Rotor platforms have shorter flight durations but have better maneuverability than fixed wing platforms and can operate at lower altitudes, collecting imagery with higher spatial resolution (Remondino et al., 2011; Siebert and Teizer, 2014). UAS data is typically processed with

ground control points (GCP) using software platforms such as Agisoft Photoscan or Pix4Dmapper to output digital surface models (DSM) and orthorectified imagery (Westoby et al., 2012; Bemis et al., 2014).

Satellite platforms often collect imagery with a lower spatial resolution (~0.5 m – 90 m) than UAS platforms, but the imagery they acquire covers a larger spatial extent and commonly distributed to users with much of the preprocessing completed, such as orthorectification and mosaicking. Despite the lower spatial resolution of these spaceborne platforms, sensors such as WorldView-2 and ASTER imagery have been successfully implemented for lithologic discrimination and spectral classification (Rowan and Mars, 2003; Dadon et al., 2011; Ruisi et al., 2011; Chen et al., 2015). WorldView-2 data has been successfully used to solve geologic problems, including constraining bedding orientation as well as aiding in identification of folds and faults (Ruisi et al., 2011). WorldView-2 is a commercial platform that has an advantage over ASTER data, with a much higher spatial resolution of <2 m; this data is used in combination with other imagery sets to identify areas of interest to target areas for UAS data collection (Ruisi et al., 2011; Digital Globe, 2016).

Manned airborne systems collect data at spatial resolutions ranging from ~0.3 m to 2 m, which are typically much higher than satellite-based sensors (Yu et al., 2006). Trefois et al. (2004) applied unsupervised classification techniques to Compact Airborne Spectrographic Imager (CASI) airborne hyperspectral imagery to identify soil and vegetation changes related to faults based on characteristic of the images without using training data. By vectorizing known features in the imagery, regions of interest (ROI) are established and used for classification analysis (Dadon et al., 2011; Grebby et al., 2011).

Maximum likelihood analysis is a technique that uses ROIs to classify imagery using a covariance algorithm; Grebby et al. (2011) successfully used this technique for the remote classification of lithologies in vegetated terrain.

Terrain data is available from multiple sources. In this work, elevation data was sourced from the national elevation dataset (NED) and UAS imagery, but it can also be acquired using airborne LiDAR or extracted from UAS imagery and used to make observations of the topographical characteristics of an area (Matthews, 2008). LiDAR is the best resource for vegetated terrain because it is an active sensor with return time data and so vegetation can be eliminated from terrain characteristics to produce a bare earth model, but in sparsely vegetated areas UAS based DSMs are comparable with LiDAR for identifying joints, discontinuities, and orientations of rock units (Fonstad et al., 2013; Bemis et al., 2014). Scale and geographic locations can be applied to UAS-based terrain data during postprocessing by using georeferenced ground control points, resulting in georeferenced datasets that are appropriate for spatial analyses (Matthews, 2008; Bemis et al., 2014). Using digital surface models, topographic contours are extracted and compared to the surface extent of geologic units, seismic data, and linear traces, such as vegetation anomalies and offset features, to calculate the orientation and dip of bedding and structures (Trefois et al., 2004; Dadon et al., 2011; Grebby, 2011; Otoo et al., 2011; Bemis et al., 2014; Chen et al., 2015). Essentially, the contacts or traces of these features are compared to the topographic contours so that their subterranean characteristics are identified using their surficial expression (Dadon et al., 2011; Chen et al., 2015). Synthetic aperture radar (SAR) from Sentinel-1 satellite data may also be used to identify structural features in the study area (Guerrieri et al., 2010).

## Radar Data Analysis

Walters et al. (2011), Rucci et al. (2012), and Garthwaite et al. (2013), each used InSAR techniques to quantify displacement and deformation rates, unrelated to seismic events. Garthwaite et al. (2013) applied interferometric synthetic aperture radar (InSAR) as a geodetic remote sensing method. They observed changes in repeat pass satellite radar data to quantify interseismic surface displacement related to low-strain tectonic deformation. By doing this, Garthwaite et al. (2013) produced tectonic deformation metrics as small as a few millimeters per year and produced a displacement velocity map over their 1,000 km long region of interest in central Tibet. Walters et al. (2011) applied InSAR to produce displacement rate maps for the North Anatolian fault in Turkey. Their use of interferogrammetry allowed them to quantify strain in two directions. Rucci et al. (2012) applied Sentinel-1 InSAR data to the quantification of surface deformation related to hydrocarbon reservoirs by searching for lineaments in the processed radar data, for carbon dioxide monitoring and sequestration. They implemented a statistical approach to process the phase and amplitude data from series of InSAR scenes, collected from different viewing angles, to produce a vertical displacement map.

Wen et al. (2016), Xu et al. (2016), Wang et al. (2017), Polcari et al. (2016), Mora et al. (2016) and Grandin et al. (2015) applied radar data for monitoring ground changes related to seismic events. Wen et al. (2016) used radar data from Sentinel-1 and Advanced Land Observing Satellite 2 (ALOS-2) to process coseismic interferograms to detect and map surface deformation related to a  $M_w$  6.5 earthquake in western China. Xu et al. (2016) processed Sentinel-1 Terrain Observation with Progressive Scans Synthetic Aperture Radar (TOPSAR) data, producing interferograms to map the coseismic

deformation related to an  $M_w$  8.5 earthquake in Chile. Wang et al. (2017) used a combination of Sentinel-1 TOPS and ALOS-2 data to produce a slip model for a  $M_w$  6.6 earthquake in western China, using interferograms. Polcari et al. (2016) used interferograms, produced from InSAR data, from Sentinel-1, as well as GPS data to identify and measure the earthquake displacement field, related to an  $M_w$  6.0 earthquake in Napa Valley, California. Mora et al. (2016) used interferograms, produced with Sentinel-1 TOPSAR data to monitor earthquakes in Japan and apply them for geologic hazard assessment and produced maps showing vertical displacement as well as the east/west direction of ground displacement. Grandin et al. (2015) used interferograms created using InSAR from Sentinel-1 and ALOS-2 to analyze fault rupture and segmentation processes in the Himalayan Thrust Belt related to the  $M_w$  7.9 Gorkha earthquake.

A simple use of radar data is the detection of lineaments by observing patterns in the brightness values in the imagery. Senske et al. (1991) applied this method for planetary geology, identifying faults on Venus by identifying linear trends in brightness values. Lepage et al. (2000) described the high geological potential of radar-derived lineaments, stating that radar brightness values often represent topographical trends. From this, we can infer the need to observe the topography in relation to brightness values, omitting lineaments that directly relate to topographic characteristics that are likely to result in high amounts of backscatter, such as prominent ridges. Van Zyl (2001) used a combination of radar and gravitational data to detect lineaments beneath ice sheets and interpreted them as geologic structures. Theilen-Willige et al. (2016) used Sentinel-1 to visually detect lineaments in western India, and interpreted them as faults and geologic

structures. Pour and Hashim, (2016) used a similar process as Theilen-Willige et al. (2016), except they interpreted lineaments with a particular trend as having potential for gold exploration in the Central Gold Belt of Malaysia.

### Multispectral Classification and Geologic Unit Mapping

Using multispectral imagery, geologic unit contacts are extracted by enhancing differences in spectral characteristics (Dadon et al., 2011; Chen et al., 2015). The units can be classified using regions of interest (ROI) and data processing techniques such as maximum likelihood classification, minimum distance classification, and support vector machine classifications (Oommen et al., 2008; Grebby, 2011). Grebby (2011) used classification techniques along with principal component analysis (PCA) and minimum noise fractionation (MNF) to map lithologies based on remotely sensed data. For this study, multispectral data sources included WorldView-2, Advanced Spaceborne Thermal Emission and Reflection Radiometer (ASTER), Sentinel-2, and National Agriculture Imagery Program (NAIP).

DigitalGlobe, a commercial satellite company, operates the WorldView-2 satellite that collects multispectral data. WorldView-2 data is an 8 band multispectral dataset that includes 4 standard colors (red, blue, green, near-infrared (NIR)) and 4 new colors (red edge, coastal blue, yellow, and a second NIR band), as well as one panchromatic band (Digital Globe, 2016). The band designations for this sensor are shown in Table 1. It has a ground sampling distance (GSD) of 0.46 m for its panchromatic band at nadir or 0.52 m at 20° off-nadir, and a GSD of 1.84 m for its multispectral bands at nadir or 2.4 m at 20° off-nadir (Digital Globe, 2016).

Pan sharpening WorldView-2 data improves the resolution of imagery using a panchromatic band so that the image processing results are comparable to sharpened imagery. Pan sharpened data is useful for making visual comparisons between the data and the resultant maps (Kamal et al., 2015). Pan sharpening has

<b>Table 1: Band designations for the WorldView-2 sensor</b>		
<u>Band</u>	<u>Spectra</u>	<u>Response (<math>\mu\text{m}</math>)</u>
1	Coastal Blue	0.400-0.450
2	Blue	0.450-0.510
3	Green	0.510-0.580
4	Yellow	0.585-0.625
5	Red	0.630-0.690
6	Red Edge	0.705-0.745
7	Near-Infrared 1	0.770-0.895
8	Near-Infrared 2	0.860-1.040
PAN	Panchromatic	0.450-0.800

been used successfully to produce false color composite images for comparison to an urban landcover classifications (Jawak et al., 2013). Fast Line-of-sight Atmospheric Analysis of Spectral Hypercubes (FLAASH) atmospheric correction resolves atmospheric interference between the satellite and the ground (Manakos et al., 2011). Manakos et al. (2011) compared WorldView-2 imagery corrected with the Atmospheric Correction (ATCOR), Simple Regression Analysis (SRA), and FLAASH algorithms to in-situ spectral measurements. They found that FLAASH and SRA outperformed ATCOR, when compared to the in-situ results (Manakos et al., 2011).

Kamal et al. (2015) applied FLAASH atmospheric correction to WorldView-2 imagery in Queensland and Indonesia as part of their workflow for classifying imagery with Trimble's eCognition software, using indices for separating areas with and without vegetation. Another study by Upadhyay et al. (2012) applied a variation of the Normalized Difference Vegetation Index (NDVI) to work in Uttar Pradesh, India, where they applied a support vector machine (SVM) to classify crop types. Jawak et al. (2013) applied the SVM algorithm to WorldView-2 data for urban landcover mapping.

Chen et al. (2011) applied an ISODATA algorithm to WorldView-2 data to statistically identify clustered pixel values and give the clusters thematic values before applying an unsupervised classification to the data (Ruisi et al., 2011). Puetz et al. (2009) applied a spectral angle mapper (SAM) algorithm to WorldView-2 data in Maui, Hawaii, where they used training data to classify urban, coastal, and mountain environments. Tarantino et al. (2012) applied a maximum likelihood algorithm to WorldView-2 data in southern Italy, using a land use map as training data and delineated water, bare land, vegetated land, and artificial landscapes. Ruisi et al. (2011) applied WorldView-2 data to structural geology problems, by identifying faults and folds in false color composite images. Folds were recognized by banded features an symmetrically curved, elongated, or oval bedding planes (Ruisi et al., 2011). Faults were detected by observing linear features in the imagery, such as lithologic offset (i.e. different types and ages of types juxtaposed together), abrupt topographic discontinuities, topographic depressions, scarps, shifts in drainage courses, and abrupt changes in vegetation (Ruisi et al., 2011). The advantage of WorldView-2 over ASTER data is that it is higher resolution in all its bands, and includes coastal blue, red edge, and an additional NIR band. The advantage of ASTER over WorldView-2, is that ASTER includes short wave infrared (SWIR) and thermal infrared (TIR), which is where minerals have distinctive absorption features (Jet Propulsion Laboratory, 2004; Digital Globe, 2016).

ASTER imagery has much lower spatial resolution (15 m in the Visible-NIR bands) than WorldView-2 (<2.5 m), but has a greater diversity of spectral response, as shown in Table 1 (WorldView-2) and Table 2 (ASTER). ASTER imagery is effective for mapping surface geology because of its 14 bands of spectral information, including four

<u>Band</u>	<u>Spectra</u>	<u>Response (<math>\mu\text{m}</math>)</u>	<u>Resolution (m)</u>
1	Green	0.52-0.60	15
2	Red	0.63-0.69	15
3	NIR	0.78-0.86	15
4	SWIR 1	1.600-1.700	30
5	SWIR 2	2.145-2.185	30
6	SWIR 3	2.185-2.225	30
7	SWIR 4	2.235-2.285	30
8	SWIR 5	2.295-2.365	30
9	SWIR 6	2.360-2.430	30
10	TIR 1	8.125-8.475	90
11	TIR 2	8.475-8.825	90
12	TIR 3	8.925-9.275	90
13	TIR 4	10.25-10.95	90
14	TIR 5	10.95-11.65	90

VNIR bands, six SWIR bands, and five thermal bands (Jet Propulsion Laboratory, 2004).

This sensor's VNIR bands are effective for detecting vegetation and iron oxides, its SWIR bands are effective for soil and lithologic mapping, while its TIR bands can help delineate silicic and carbonate lithologies (Ninomiya, 2004; Gad and Kusky, 2007).

Mineral indices enhance a variety of spectral characteristics. These indices have been applied to ASTER data and used for geologic mapping and mineral exploration using qualitative observations from creating false color composites and quantitatively assessed using classification algorithms, such as Maximum Likelihood Analysis (MLA) and Spectral Angle Mapper (SAM) (Gomez et al., 2005; Gabr et al., 2010).

ASTER is useful for geologic mapping worldwide. It has been used with relative band difference techniques to apply it for lithologic mapping in the Chocolate Mountains of southern California (Rowan and Mars, 2003). Spectral indices are applied to delineate and map carbonate, quartz and mafic lithologies in Yushishan, Xigaze, and Mt. Fitton in

China (Ninomiya et al., 2005). ASTER indices have also been applied to remotely identify hydroxyl, kaolinite, alunite, and calcite-bearing lithologies in Mountain Pass, in southern California (Zhang et al., 2007). Gad and Kusky (2007) used the imagery to map metamorphosed volcanic and sedimentary rocks of the Wadi Kid metamorphic belt in southeastern Sinai, Egypt.

ASTER imagery has been used with unsupervised classification techniques for lithologic mapping in Iron Hills, Colorado (Rowan, 1998). Gabr et al. (2010) implemented ASTER imagery for gold exploration in northeast Egypt, using principal component analysis (PCA) and spectral indices which delineated hydroxyl-bearing, kaolinite, alunite, and calcite bearing lithologies. Pour and Hashim (2012) used ASTER imagery to detect porphyry copper and epithermal deposits using spectral indices, to delineate hydroxyl, kaolinite, alunite, calcite, and quartz bearing lithologies as well as carbonate and mafic lithologies, as well as the spectral angle mapper (SAM) algorithm and principal component analysis. Ninomiya (2004) used the imagery for lithologic mapping in Nevada's Cuprite Hills and Stonewall Mountain by applying band math techniques that delineate vegetation, calcite, silica, carbonates, quartz, and minerals bearing hydroxyl and alunite.

Sentinel-2 data is applied to mineralogic exploration because of its ability to delineate iron containing minerals (van der Werff and van der Meer, 2015). Sentinel-2 data is a multispectral sensor that is qualitatively comparable to Landsat 8 in function, but it has a higher spatial resolution; Landsat 8 has a spatial resolution of 30 m in the visible-NIR spectra, while Sentinel-2 has a spatial resolution of 10 – 20 m in the visible-NIR

spectra (van der Werff and van der Meer, 2016). The Sentinel-2 band designations are shown in Table 3.

**Table 3: Band designations for the Sentinel-2 sensor**

<u>Band</u>	<u>Spectra</u>	<u>Response (<math>\mu\text{m}</math>)</u>	<u>Resolution (m)</u>
1	Coastal Aerosol	0.433-0.453	60
2	Blue	0.457-0.523	10
3	Green	0.543-0.578	10
4	Red	0.650-0.680	10
5	Red Edge 1	0.698-0.713	20
6	Red Edge 2	0.733-0.748	20
7	Red Edge 3	0.773-0.793	20
8	NIR	0.785-0.900	10
8A	Red Edge 4	0.855-0.875	20
9	Water Vapor	0.935-0.955	60
10	SWIR 1 (Cirrus)	1.365-1.395	60
11	SWIR 2	1.565-1.655	20
12	SWIR 3	2.100-2.280	20

Sentinel-2 data is applied to mineral exploration because of its coverage of the iron absorption feature, located near 0.9 micrometers (van der Werff and van der Meer, 2015). Iron detection is the most common geological application of Sentinel-2 data that appears in literature. Van der Meer et al. (2014) presents a set of band ratios and applied them to Sentinel-2 data using a variety of iron indices to solve geological problems by using a multirange spectral feature fitting classification and comparing the results to a geologic map; these indices delineate different kinds of iron, including ferric iron, ferrous iron, laterite, gossan, ferrous silicate, and ferric oxides.

NAIP is a widely used resource for vegetation analysis, due to its high spatial resolution and the presence of the red and near infrared bands (Table 4: Band designations for the NAIP Sensor) that are used to calculate Normalized Difference Vegetation Index (NDVI). Though NAIP imagery is generally used for vegetation

analysis, one geologic application was demonstrated by Dinger et al. (2007). They applied a decorrelation stretch to NAIP data as a cost effective way of identifying potential sinkholes in an area of karst geology. Falkowski et al. (2017) demonstrated application of this sensor is using the NDVI equation to identify changes in

habitat for the purposes of conservation management of prairie grouse, identifying changes in sagebrush habitat to woody vegetation, by extracting tree canopy cover.

Potter and Li (2014) also used NAIP for

biological conservation, using NDVI to assess vegetation cover as a tool in mitigating habitat loss in renewable energy projects. Tagestad and Downs (2007) used NAIP-derived NDVI for the Bureau of Land Management (BLM) for vegetation classification, by identifying anomalies in the NDVI distribution.

Swetnam et al. (2013) used NDVI from NAIP imagery to characterize riparian vegetation, producing colorized maps of the distribution of NDVI values. Knight et al. (2013) used a combination of data sources, including elevation data, LiDAR, radar, and NAIP data for the purposes of wetland classification. ROIs established using NAIP imagery and wetlands were classified using a See5 classifier. Bishop et al. (2014) implemented NAIP imagery for the purposes of classifying fire-caused tree mortality in a redwood forest. They used a combination of techniques including principal component analysis (PCA), unsupervised classification, and NDVI for their assessment. Bales et al. (2011) used PCA and NDVI to identify vegetation densities and the locations of trees in order to assess soil moisture response to snowmelt in the Sierra Nevada mixed-conifer

<u>Band</u>	<u>Spectra</u>	<u>Response (µm)</u>
1	Red	0.608-0.662
2	Green	0.533-0.587
3	Blue	0.428-0.492
4	NIR	0.833-0.887

forest. Strand et al. (2013) implemented NAIP imagery for fire management in Lava Beds National Monument, by identifying pixels representing six land cover types and applying Maximum Likelihood Analysis to produce a series of maps for each landcover type.

Minerals tend to have similar reflectance patterns in the VNIR spectra, but having a diverse response in the SWIR and TIR range and so they can be delineated by enhancing their absorption features in those ranges (Kruse, 2002). Both ASTER and Sentinel-2 have SWIR sensors, making them the most appropriate for lithologic classifications. ASTER also has the benefit of having TIR bands, which are especially effective for delineating siliceous lithologies (Kruse, 2002). Vegetation is most responsive in the NIR spectral range (Knipling, 1970). The spatial resolution in the near infrared bands for ASTER (15 m) and Sentinel-2 (10 m) make them less suited for detecting vegetation in the Challis area, because the pixel size is significantly larger than the sagebrush plants (~1 m or smaller) that dominate the community of vegetation. Though NAIP and WorldView-2 lack SWIR and TIR bands, they have NIR sensors with spatial resolutions (0.5 m for NAIP and <2 m for WorldView-2) much closer in size to individual sagebrush plants. This combination multiscale sensors allows us to use the best tools available to perform spectral differentiation of rock types as well as the capability to observe vegetation patterns as evidence for the presence of geologic structures.

## Chapter 3: Remote Sensing Applications for Geologic Analyses

### Introduction

As an increasing variety of new sensors emerge, remote sensing is becoming an effective tool for geological exploration and the identification of geologic structures in challenging environments where there is land cover. Using a variety of sensors, this study uses remote sensing to identify the surface expression of a fault that corresponds to a cluster of seismicity located north of Challis, Idaho (Figure 1). Faults are identified by observing the offset of spectral and topographical patterns in the study area, via classification algorithms, spectral indices, and image decorrelation (i.e. PCA and decorrelation stretching). Using combinations of these techniques, information was inferred from WorldView-2, ASTER, Sentinel-1 (radar) and Sentinel-2 (multispectral), and NAIP data. As these results were compared to one another, the surface expression of the hypothesized fault was extracted from the imagery and is included on a map as a newly identified active fault.

Principal component analysis (PCA) used by Grebby et al. (2011) identified spectral differences in imagery scenes; this along with decorrelation stretches applied to the imagery provides a basis for classification techniques. Both PCA and decorrelation stretching enhance spectral data for classifications of lithologic compositions and vegetation patterns. Decorrelation stretches are most effective for data sets with a small number of bands, as it is limited to three bands. Decorrelation stretches result in a decorrelated band for each input band, where pixel brightness values correspond to how each band correlates to the others (i.e. high brightness values relate to low correlation). PCA on the other hand can be applied to any number of bands and results in the same

number of output bands as input bands (e.g. PCA1, PCA2, PCA3), where PCA1 has the greatest contrast of features and this contrast generally declines in each subsequent output.

ASTER VNIR bands are effective for detecting vegetation and iron oxides, its SWIR bands are effective for soil and lithologic mapping, while its TIR bands can help delineate silicic and carbonate lithologies (Ninomiya, 2004; Gad and Kusky, 2007). Many lithologic discrimination indices have been published, which are applied to enhance spectral patterns in the data. The imagery can be also be statistically processed using principal component analysis (PCA), where the results of the statistical analyses are used for classification (Gabr et al., 2010). Classification algorithms are successfully applied to this imagery in order to extract geological information (Gomez et al., 2005; Gabr et al., 2010).

WorldView-2 data was used by Ruisi et al. (2011) to qualitatively assess geologic structures by qualitatively observing a 8-5-1 False Color Composite (FCC) image using near-infrared 2 (red), red (green), and coastal blue (blue) for evidence of faults. Kamal et al. (2015), Upadhyay et al. (2012), applied indices to WorldView-2 data to enhance spectral patterns in the imagery. Similar techniques to these are applied to WorldView-2 imagery, in the study area north of Challis, Idaho. By qualitatively assessing imagery and FCC images, evidence of geologic structures based on linear patterns in vegetation and attitude of bedding planes provide clues to fault locations.

The use of radar for fault detection includes the detection of geologic structures as well as quantification of surface deformation related to them. Unlike other sensors discussed in this work, radar is an active sensor. The satellite emits a signal, which

interacts with the ground before reflecting to the satellite. The amplitude and/or intensity of the signal are used to make interpretations about the ground. These intensity changes may be due to roughness and the dielectric constant of the surface. Surface roughness affects the intensity, because of the signal scattering in many directions by the roughness of the surface, and so the odds of the scattered signal returning to the sensor are much higher than they are for a smooth surface, which scatters the signal in fewer directions. Brightness values in the data help identify geological phenomena, especially the observation of lineaments in the brightness values. For example, Senske et al. (1991) applied this method for planetary geology, identifying faults on Venus by identifying linear trends in brightness values. Van Zyl (2001) used a combination of radar and gravitational data to detect lineaments beneath ice sheets interpreted as geologic structures. Theilen-Willige et al. (2016) used Sentinel-1 to visually detect lineaments that were interpreted as faults and geologic structures.

Van der Werff and van der Meer (2016) conducted their comparison by applying Sentinel-2 data for geologic exploration, masking out vegetation using normalized difference vegetation indices (NDVI) and creating false color composite images that were compared to geological maps. Mandanici and Bitelli (2016) enhanced Sentinel-2 imagery for general surface exploration, using the normalized difference water index (NDWI), NDVI, and a ferrous iron index. Van der Werff and van der Meer (2015) analyzed Sentinel-2 data and found that it was applicable for iron exploration, by fitting known iron-bearing pixels to the spectral curves of bronzite, goethite, jarosite, and hematite. Mielke et al. (2014) uses Sentinel-2 to identify iron mineralization associated with copper deposits. Mielke, Bösche, et al. (2014) describes a 3-point band ratio technique to

enhance iron absorption features around 0.9 micrometers, utilizing the red, SWIR, and NIR bands.

NAIP is a widely used resource for vegetation analysis, due to its high spatial resolution of 0.5 m and the presence of the red and near infrared bands that are applied to the Normalized Difference Vegetation Index (NDVI) equation. Methods for enhancing the spectral features in NAIP data include the implementation of a decorrelation stretch, to enhance the spectral differences in the data, as well NDVI, for purposes ranging from sinkhole detection to habitat conservation (Dinger et al., 2007; Tagestad and Downs, 2007; Potter and Li, 2014). It is also a useful tool for characterizing riparian vegetation, identifying fire-caused tree mortality, and assessing vegetation density (Bales et al., 2011; Swetnam et al., 2013; Bishop et al., 2014). Because of the 0.5 m resolution of this sensor and the relationship between vegetation patterns and fault presence, as described by Ruisi et al. (2011), NAIP imagery is a useful tool for geological assessment.

The purpose of this work is to identify the potential surface expression of a fault that corresponds to a cluster of seismicity located north of Challis, ID (Figure 1) using remote sensing techniques. Expected surface expressions include two-dimensional or three-dimensional offset of lithologic units and lineations in the topography, as well as, the six features discussed by Ruisi et al. (2011) including: (1) layers of different types and ages of rock units sit side-by-side (offset), (2) abrupt topographic discontinuities of landforms, (3) depressions along the fault trace (broken rock is more easily eroded), (4) scarps or cliffs, (5) sudden shifts of drainage courses, and (6) abrupt changes in vegetation patterns. Remote sensing analysis techniques provide evidence for locations of these features (e.g. Maximum Likelihood Analysis, Support Vector Machine, and

Principal Component Analysis (PCA)). These techniques were applied to multiscale remotely sensed imagery, including Sentinel-2, ASTER, WorldView-2, and NAIP data. Assessments of topographic information to delineate lithologic offsets are based on elevation data sourced from the US National Elevation Dataset (NED) and Sentinel-1. By using a variety of classification techniques, the results are compared to one another for quality, increasing the chance for geologic features to be identified and targeted for further data acquisition and field observations. This multiscale approach allowed us to delineate areas of interest that relate to structural features. Based on the analyses, we inferred the probable locations of faults in the area that may be related to the seismic cluster shown in Figure 1. This process results in a map of candidate fault locations, based on the image analysis. By identifying the trace of the fault and its relationship to spectral patterns in the imagery, we can infer the geometry of the fault and gain a better understanding of active faulting in this region.

## Methods

### Estimating Study Area Boundaries based on Seismicity

The probable distance of the active fault that corresponds to the observed seismicity in the study area was identified using the minimum and maximum depths of earthquake hypocenters in the seismic cluster of interest. The dips of nearby portions of the Lost River fault system were measured by comparing the trace of the fault to elevation contours that were generated using elevation data from the National Elevation Dataset, with 10 m resolution. Elevation contours were generated using ArcMap and compared to the trace of the Challis segment. A location was identified where two

elevation contours intersect the Lost River fault. The distance between the intersections between the fault and the elevation contours were measured and the elevation change was noted and input into Equation 1 to calculate the dip. Using Equation 1, with an elevation change of 20 m over a distance of 33.3 m, the resultant dip is 59°. Using a similar methodology, we can identify the probable distance of the earthquakes from the seismic cluster of interest. Using the measured dip of 59°, a minimum earthquake depth and a maximum earthquake depth are used to calculate the minimum and maximum distance of the fault from the seismicity using Equation 2.

$$Dip = \tan^{-1}\left(\frac{\text{Elevation Change}}{\text{Distance}}\right) \quad (1)$$

$$\text{Surface Distance} = \frac{\text{Earthquake Depth}}{\tan(59)} \quad (2)$$

After identifying a target area where surface expression of the fault would be expected, potential study area boundaries are delineated that have the highest potential for the fault's location.

## Data Sources

This multiscale data approach includes several different spectral data sources (Table 5). This includes ASTER data, with a spatial resolution ranging from 15 m – 90 m, Sentinel-2 data, with a spatial resolution ranging from 10 m – 60 m, NAIP data, with a spatial resolution of 0.5 m, WorldView 2 at <2.5 m resolution, and UAS data with a

spatial resolution of 7.41 cm. Each of these sensors includes a unique set of spectral responses that are applied to the delineation of geologic structures.

<b>Table 5: Spectral data sources</b>				
<u>Data Source</u>	<u>Type</u>	<u>Number of Bands</u>	<u>Spatial Resolution</u>	<u>Spectral Response</u>
<u>ASTER</u> NASA Land Processes Distributed Active Archive Center (LP DAAC), USGS/Earth Resources Observation and Science (EROS) Center, Sioux Falls, South Dakota	VNIR	3	15 m	0.52 - 0.86 $\mu\text{m}$
	SWIR	6	30 m	1.600 - 2.430 $\mu\text{m}$
	TIR	5	90 m	8.125 - 11.650 $\mu\text{m}$
<u>Sentinel-2</u> European Space Agency	VNIR	10	10-20 m	0.433 - 0.955 $\mu\text{m}$
	SWIR	3	20-60 m	1.365 - 2.280 $\mu\text{m}$
<u>WorldView-2</u> DigitalGlobe Foundation	UV	1	< 2 m	0.400 - 0.450 $\mu\text{m}$
	VNIR	7	< 2 m	0.450 - 1.040 $\mu\text{m}$
<u>NAIP</u> U. S. Department of Agriculture, Farm Service Agency	VNIR	4	0.5 m	0.608 – 0.887 $\mu\text{m}$
<u>UAS</u> Parrot Disco	RGB	3	7.41 cm	Natural Color

## Terrain Based Geological Feature Detection

### *Digital Elevation Model Data*

A hillshade was produced from the national elevation dataset (NED) and the elevation was colorized and draped on top of that hillshade. Qualitative information was inferred from this output, by observing any scarps or cliffs, depressions within the hypothesized fault area, and topographic discontinuities.

### *LiDAR Data*

LiDAR Data was not available for the particular areas of interest, but it was available along the Salmon River, east of Challis where the course changes from southwestward to southward. This “Challis Valley” LiDAR dataset was acquired from the Bureau of Reclamation. It was assessed for topographic lineaments that could relate to the surface expression of a fault between our area of interest and the mapped northern extent of the Lost River fault system.

### *Radar Data*

This study explored several methods to assess which approach would identify ground surface change from Sentinel-1 data; however, as the sensor was not launched until April 2014, the time-period to evaluate change using interferogrammetry or intensity algorithms is limited. Instead, lineaments were identified in the imagery using the brightness of the vertical-horizontal (VH) .tiff image that was included in the Sentinel-1 SLC package. The brightness values that corresponded to the Lost River fault system were observed and interpreted as a minimum threshold for fault detection. Pixels that were brighter than that minimum value were symbolized, and identified in the area where an active fault may potentially be located.

## Multispectral Data Classification Approaches for Geologic Mapping

### *WorldView-2*

The WorldView imagery was preprocessed using the Gram-Schmidt pan sharpening tool for qualitative assessment of the study area in ENVI 5.3 (Harris Corporation, USA). Pan sharpening applies the panchromatic band to the multispectral

imagery to improve the image quality, simulating a higher spatial resolution than is truly present. It is not applicable for processing purposes, but is a useful tool for improving the aesthetics of the imagery. The original, unsharpened, data was converted to radiance and atmospherically corrected using ENVI's Fast Line-of-sight Atmospheric Analysis of Spectral Hypercubes (FLAASH®) that is part of the atmospheric correction module. The presence of iron is commonly used to delineate lithologies in remote sensing (van der Werff and van der Meer (2015) and Qiu et al. (2015)). To extract these patterns in the WorldView-2 imagery, the new iron index (Exelis Visual Information Solutions Inc., 2017b), using Equation 3.

$$[(\text{Green} * \text{Yellow}) / (\text{Blue} * 1000)] \quad (3)$$

Vegetation patterns were extracted from the imagery using the optimized soil adjusted vegetation index (OSAVI) using Equation 4.

$$[(1 + L) * (\text{Red} - \text{NIR}) / (\text{NIR} + \text{Red} + L)] \quad (4)$$

L is a factor that estimates the amount of bare soil (MicroImages Inc., 2015) and is automatically determined by the ENVI software.

The WorldView improved vegetation index (Exelis Visual Information Solutions Inc., 2017a) was applied to enhance spectral differences in the WorldView-2 imagery, using Equation 5.

$$[(\text{NIR2} - \text{Red})/(\text{NIR} + \text{Red})] \quad (5)$$

The non-homogeneous feature index is a normalized difference index (Exelis Visual Information Solutions Inc., 2017c), which utilizes the red edge and coastal bands to delineate features that have a brighter response than the “background” pixels (Wolf, 2010), was applied to enhance spectral differences, using Equation 6.

$$[(\text{Red Edge} - \text{Coastal Blue}) / (\text{Red Edge} + \text{Coastal Blue})] \quad (6)$$

Following the methods of Ruisi et al. (2011), an 8-5-1 (NIR2, yellow, coastal blue) FCC band combination along with the WorldView New Iron Index, the Non-homogeneous Feature Index, the WorldView Improved Vegetation Index, and the Optimized Soil Adjusted Vegetation indices were compared along 10 m national elevation data and assessed for evidence of faulting.

Each product was assessed for relevant evidence of faulting. Each index was overlain onto a hillshade, derived from the 10 m National Elevation Dataset, to enhance the visualization of corresponding anomalies between the indices and topographic patterns. The FCC results were assessed for each of the seven criteria, while the other indices were only assessed for the information that is relative to their indices. The New Iron Index and Non-Homogeneous Feature Index are assessed for lineaments, lithologic offset, and shifts in drainages, while the WorldView New Vegetation Index and OSAVI are assessed for lineaments, shifts in drainage courses, and changes in vegetation.

### *ASTER Data Analyses*

The ASTER scene for the study area was processed for classification using PCA and spectral indices. All 14 bands of the ASTER Level 1 Precision Terrain Corrected Registered At-Sensor Radiance (L1T) data was stacked, and a PCA was performed on the stacked bands. The data was processed using 16 indices, shown in the resultant indices were stacked. A mask was made using the stacked index data, masking out all locations in the mask area where any of the stacked bands have a cell with no value. This mask was applied in all further processing. A PCA was performed on the stacked and masked index data. The first four bands of both PCA are stacked for classification, resulting in an 8-band stack.

Using a false color composite of the first three bands from the PCA and the Challis Quadrangle, regions of interest (ROI) were created for five lithologic compositions: (1) alluvium, (2) sedimentary rock, (3) metamorphosed sedimentary rock, (4) felsic-intermediate rock, and (5) mafic-intermediate rock. The sedimentary rock ROI includes examples of dolomite, limestone, mudstone, siltstone, sandstone, chert, and argillite. The metamorphosed sedimentary rock ROI includes examples of quartzite, pebbly quartzite, feldspathic quartzite, and phyllite; in some cases the quartzites contain argillite laminations. These classes are based on lithologic compositions described in the 1:62,500-scale Geologic Map of the Challis Quadrangle (McIntyre and Hobbs, 1987). This is preferable over using lithologic units, because the Challis Quadrangle is the highest quality map available and it does not cover the entire study area. Using the 5 ROI, three classification techniques were applied to the imagery: maximum likelihood analysis (MLA), support vector machine (SVM), and minimum distance (MD). The accuracy of the results was analyzed using a confusion matrix to assess overall accuracy percentage

and kappa coefficient. Each classification is assessed for lineaments, lithologic offset, and shifts in drainage patterns.

<b>Table 6:</b> Band equations applied to ASTER imagery to delineate lithologies and mineralogies. Band designations are defined in Table 2.		
<b>Index</b>	<b>Band Math</b>	<b>References</b>
Alunite	$(7 / 5) * (7 / 8)$	(Zhang et al., 2007); (Gabr et al., 2010); (Pour and Hashim, 2012)
	$(7 * 7) / (5 * 5)$	(Ninomiya, 2004)
Carbonate	13 / 14	(Ninomiya, 2004); (Ninomiya et al., 2005); (Ninomiya and Fu, 2010); (Pour and Hashim, 2012)
Dolomite	$(6 + 8) / 7$	(Rowan and Mars, 2003)
Hydroxyl bearing	$(7 / 6) * (4 * 6)$	(Zhang et al., 2007); (Gabr et al., 2010); (Pour and Hashim, 2012)
	$(4 * 7) / (6 * 6)$	(Ninomiya, 2004)
	$(4 * 7) / (5 * 5)$	(Ninomiya, 2004)
Iron Oxides	2 / 1	(Rowan and Mars, 2003)
Kaolinite	$(4 / 5) * (8 / 6)$	(Zhang et al., 2007); (Gabr et al., 2010); (Pour and Hashim, 2012)
Limestone	$(7 + 9) / 8$	(Rowan and Mars, 2003)
Mafic	12 / 13	(Ninomiya et al., 2005); (Pour and Hashim, 2012)
	$(12 * 14 * 14 * 14) / (13 * 13 * 13 * 13)$	(Ninomiya and Fu, 2010)
Muscovite	$(5 + 7) / 6$	(Rowan and Mars, 2003)
Quartz	$(11 * 11) / (10 * 12)$	(Ninomiya, 2004); (Ninomiya et al., 2005); (Ninomiya and Fu, 2010); (Pour and Hashim, 2012)
Silica + Carbonates	12 / 13	(Ninomiya, 2004)
Silica (igneous)	$(12 * 14) / 13$	(Ninomiya, 2004)

### *Sentinel-2*

The Sentinel-2 scene for the study area was processed for classification using PCA and spectral indices. All 12 bands of the Sentinel-2 data were stacked, and a PCA

was performed on the stacked bands. The data was processed using 8 indices, shown in Table 7 the resultant indices were stacked. A PCA was performed on the stacked and index data. The first four bands of raw data both PCA and the first three bands of the index PCA are stacked for classification, resulting in a seven-band stack.

Using the same ROI's that were applied in the ASTER processing, the same five lithologic compositions were used for classifying the imagery. Three classification techniques were applied to the imagery: maximum likelihood analysis (MLA), support vector machine (SVM), and minimum distance (MD). The accuracy of the results was analyzed using a confusion matrix to assess overall accuracy percentage and kappa coefficient. Each classification is assessed for lineaments, lithologic offset, and shifts in drainage patterns.

**Table 7:** Sentinel-2 indices, from Van der Meer et al. (2014). Band designations are defined in Table 3.

Type	Index	Band Math
Mineral	Ferric Iron	4 / 3
	Ferrous Iron	$(12 / 8) + (3 / 4)$
	Laterite and Silicate Alteration	11 / 12
	Gossan	11 / 4
	Ferrous Silicates	12 / 11
	Ferric Oxides	11 / 8
Vegetation	Vegetation	8 / 4
	NDVI	$(8 - 4) / (8 + 4)$

### NAIP

Two NAIP scenes that cover the study area were processed to produce natural color composite images, false color composites produced from decorrelation stretched

results, and Normalized Difference Vegetation Index (NDVI). A was NDVI calculated for both images using Equation 7.

$$[(\text{float}(b4) - \text{float}(b1)) / (\text{float}(b4) + \text{float}(b1))] \quad (7)$$

A decorrelation stretch was applied to the NAIP imagery to enhance the differences between bands. Decorrelated images were output using band 4 (NIR), band 3 (blue), and band 2 (green). The NDVI and decorrelation stretch images are displayed in ArcMap 10.4.1 (Esri, USA), using a histogram equalize stretch to enhance the colors of the images and reduce the presence of the seam between the images. The natural color image and decorrelation stretch results are assessed for lineaments, lithologic offset, shifts in drainage patterns, and changes in vegetation. The NDVI results are assessed for lineaments, shifts in drainages, and changes in vegetation patterns.

Fieldwork was conducted in the western study area, where we performed transects to assess the area to evaluate evidence of significant, active faults. We hiked approximately perpendicular to the trend of the Lost River fault, within the Spring creek drainage, starting near the confluence of Spring creek and Darling creek and continued eastward beyond the sharp bend in the Spring creek drainage and then hiked eastward along the southern ridge. During these transects, the area was assessed for offset lithological units, slicken lines, fault gouge, and fault breccia.

## Results

### Candidate Fault Locations

The probable distance of the active fault constraining boundaries for the northern study area was determined using the minimum and maximum depths of the seismic cluster of interest. Using the measured dip of  $59^\circ$ , the minimum map distance of 1.73 km and a maximum map distance of 9.98 km from the clustered seismicity epicenters. Two areas of interest within the northern study area were identified as the best candidates for the fault location. They are referred to as the “western study area” (Figure 4A) and the “eastern study area” (Figure 4B).

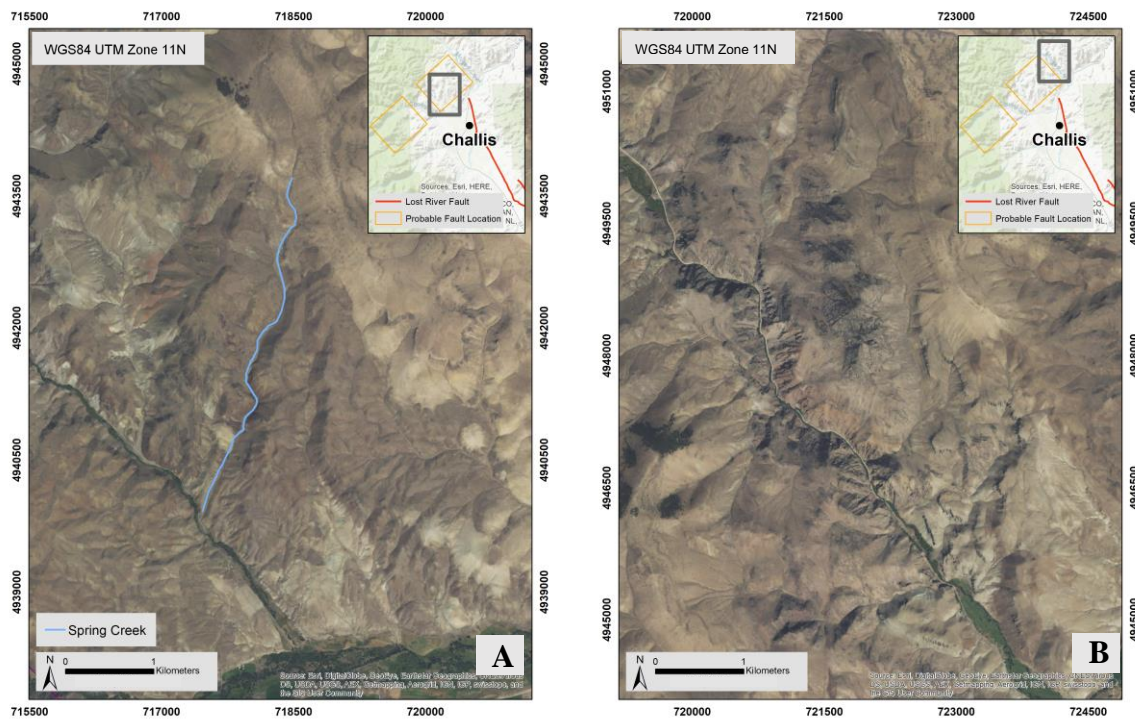


**Figure 4:** Two study areas to search for evidence of an active fault. Figure A is the western study area and figure B is the eastern study area.

## Topographic Analysis Results

In the western study area (Figure 5), the 10 m National Elevation Dataset topographic data revealed depressions along the trace of the hypothesized fault along with topographic discontinuities, and a shift of the course of a drainage as it intersects the hypothesized fault trace. No scarps or cliffs were observed. In the eastern study area (Figure 6) a depression along the trace of the hypothesized fault was also observed. There were no observable topographic discontinuities, shifts of drainage course, scarps, or cliffs. Though the existing LiDAR data along the Salmon River was assessed for topographic lineaments between the Lost River fault system and the northern area of interest, none were observed.

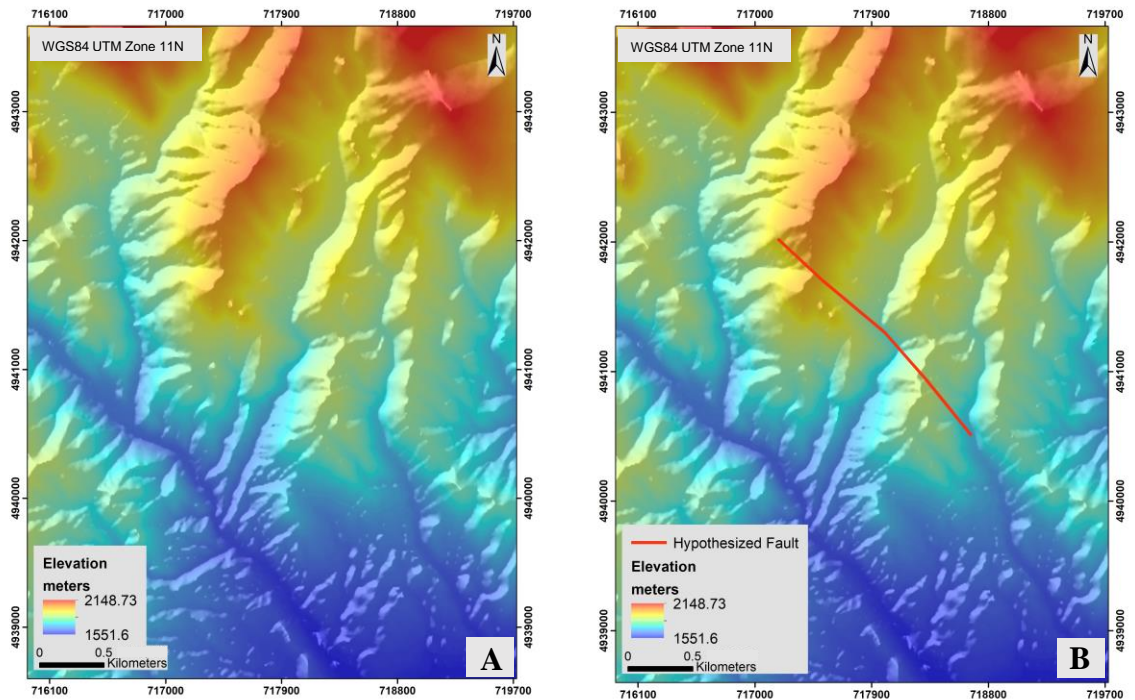


**Figure 5:** Elevation information for the western study area, derived from the USGS National Elevation Database (NED), draped over a hillshade. Maps A and B are identical, except map B is overlain by the hypothesized fault.

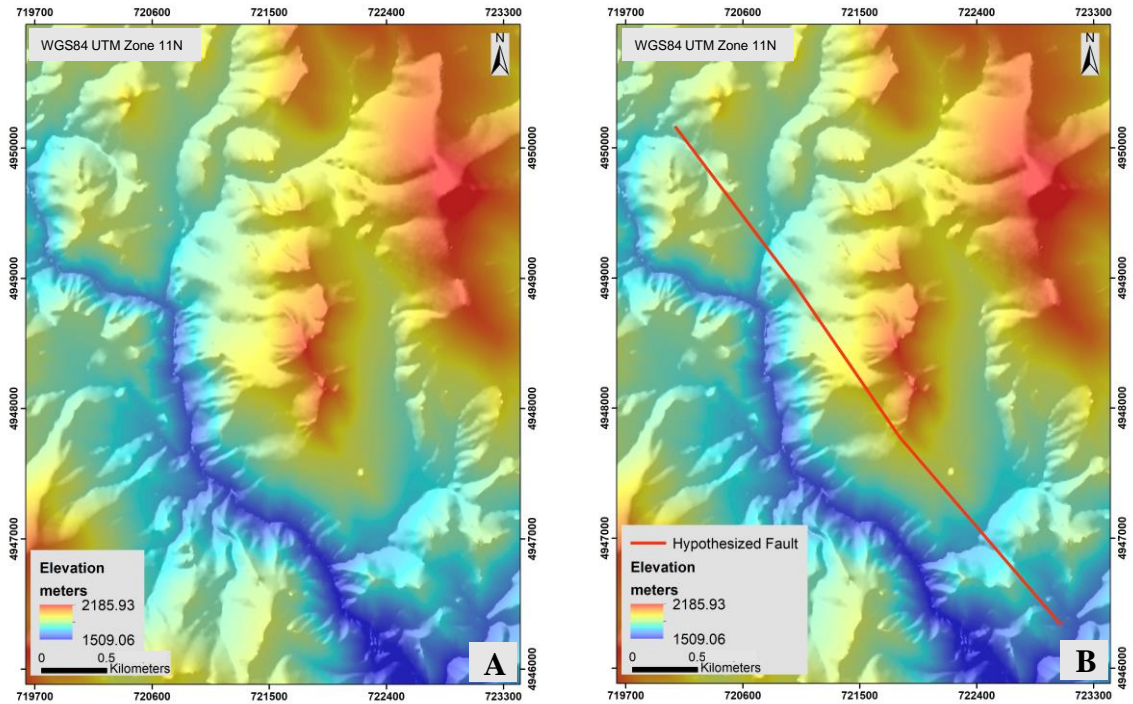


**Figure 6:** Elevation information for the eastern study area, derived from the USGS National Elevation Database (NED), draped over a hillshade. Maps A and B are identical, except map B is overlain by the hypothesized fault.

The brightness of the SAR signal sensed by the Sentinel-1 satellite were symbolized and observed for lineations. Because these lineations are prominent along the Lost River fault system, they may also be identified along an active fault north of the Salmon River. The western study area (Figure 7a) did not have any lineaments that are observed in the SAR data, but the eastern study area (Figure 7b) has a prominent set of lineaments. The northeastern lineament in the eastern study area corresponded to and followed topographic high and closely resembles the drainage patterns. It is unlikely to correspond to a fault. The southeastern lineation in the eastern area was not interpreted as a product of topography, because it cross-cuts the topographical trends that are observed in the NED results.

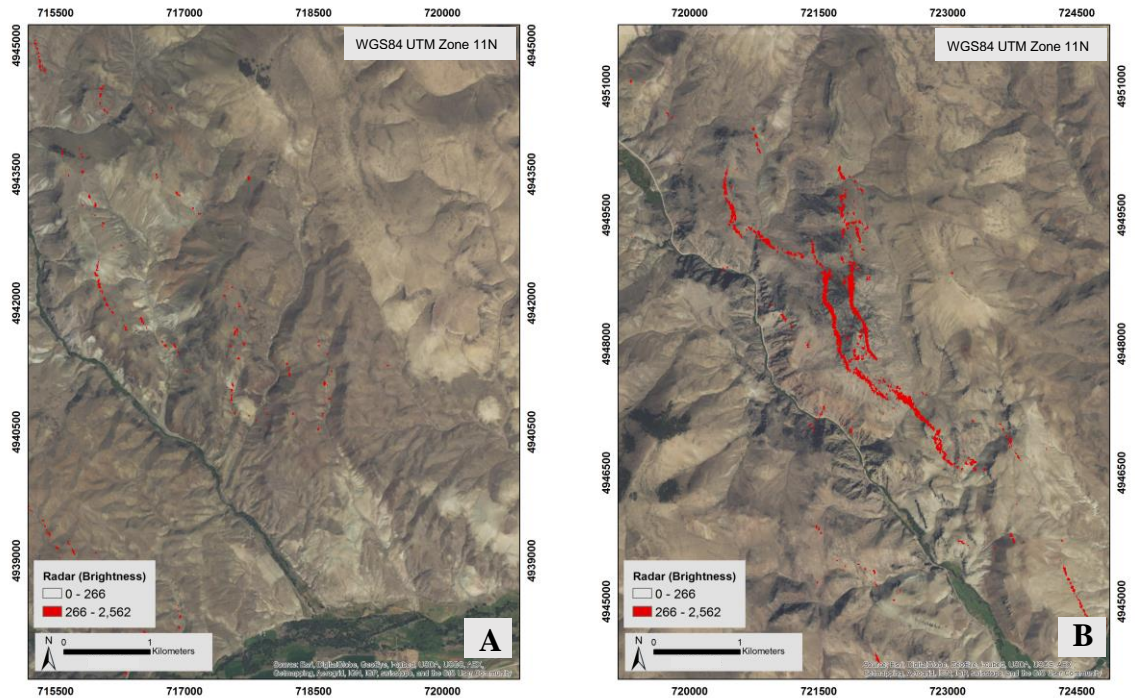


**Figure 7:** Brightness values of the radar signal received by the Sentinel-1 sensor, the brightest pixels are shown in red. Map A is the western study area and Map B is the eastern study area.

### Multispectral Analysis Results

In the WorldView-2 false color composite images of the two study areas (Figures 8 and 9), band 8 (NIR2) is assigned to red, band 5 (yellow) is assigned to green, and band 1 (coastal blue) is assigned to blue. In these results, the red coloration is vegetation and the rest of the coloration differences correspond to the surface lithologies. Evidence for a fault is observed in both study areas. In the western study area (Figure 8), lineaments and shifts in drainage patterns are observed that correspond with the trend of the hypothesized fault. Topographic information was inferred from this image, such as topographic discontinuities that correspond to the hypothesized fault and depressions along the hypothesized fault trace. There are no observable lithologic offsets, changes in vegetation, scarps, or cliffs. In the eastern study area (Figure 9) lineaments were observed

as well as a subtle topographic depression along the hypothesized fault trace. There was no observable evidence for lithologic offset, topographic discontinuities, scarps, cliffs, shifts in drainage patterns, or changes in vegetation. In this false color composite, faintly red colored pixels southwest of the east fault appear to be composed of poorly consolidated lithologic material, when compared to the Google Earth imagery; vegetation in the imagery appears red, and so this may relate to the presence of vegetation in the loose material.

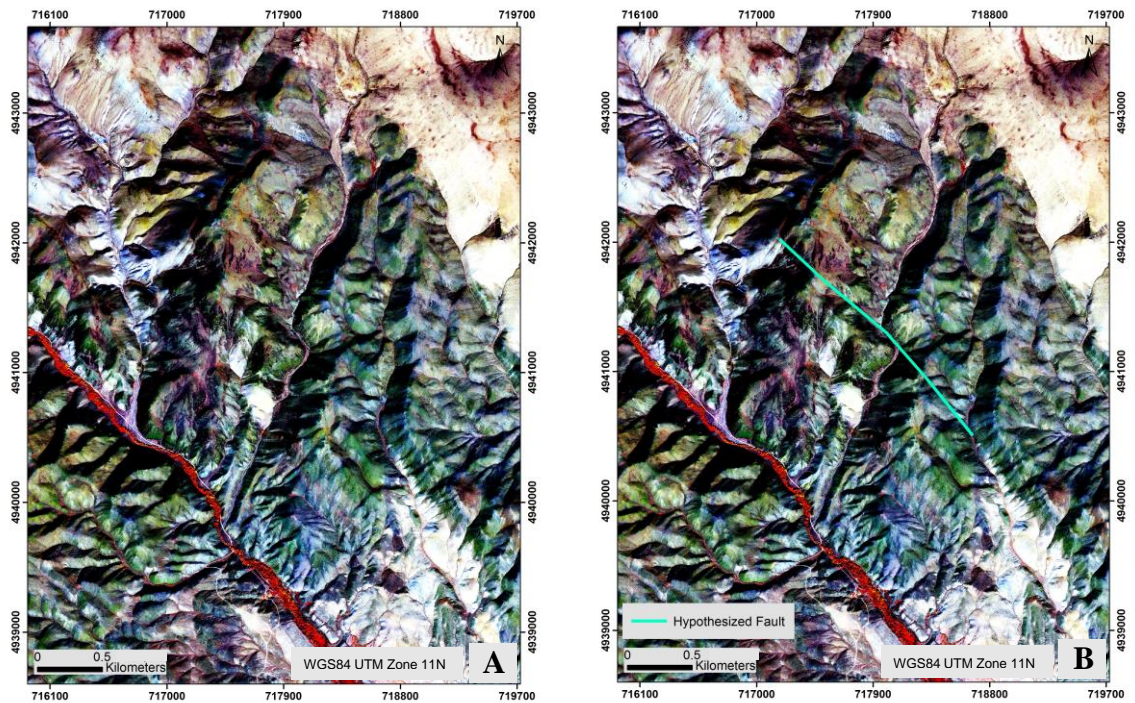


**Figure 8:** WorldView-2 false color composite image of the western study area, where band 8 (NIR2) is assigned to red, band 5 (yellow) is assigned to green, and band 1 (coastal blue) is assigned to blue. Maps A and B are identical, except map B is overlain by the hypothesized fault. Image Source: Worldview-2 satellite images courtesy of the DigitalGlobe Foundation.

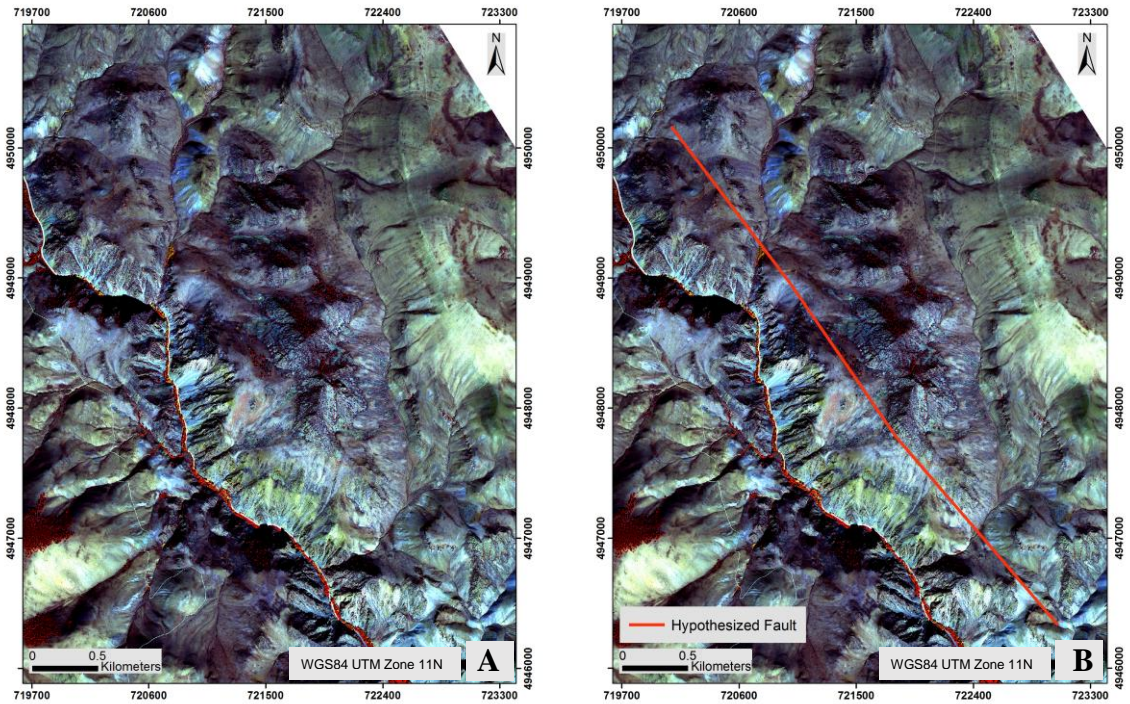


**Figure 9:** WorldView-2 false color composite image of the eastern study area, where band 8 is assigned to red, band 5 is assigned to green, and band 1 is assigned to blue. Maps A and B are identical, except map B is overlain by the hypothesized fault. Image Source: Worldview-2 satellite images courtesy of the DigitalGlobe Foundation.

In the result for the western study area’s WorldView New Iron Index (Figure 10) lineaments were observed in the pixel brightness values along with shifts in the major drainage course that correspond to the trace of the hypothesized fault. There was some evidence of lithologic offset that corresponded to the hypothesized fault as well, but when these patterns were compared to the aspect of the hills, the low iron values seemed to correlate to north facing aspects and thus the result was likely an artifact of shadowing. In the eastern study area (Figure 11), the only feature that supported the presence of a fault is a lineament, observed as a trend of abrupt changes of brightness values in the resultant index along the location of the hypothesized fault.

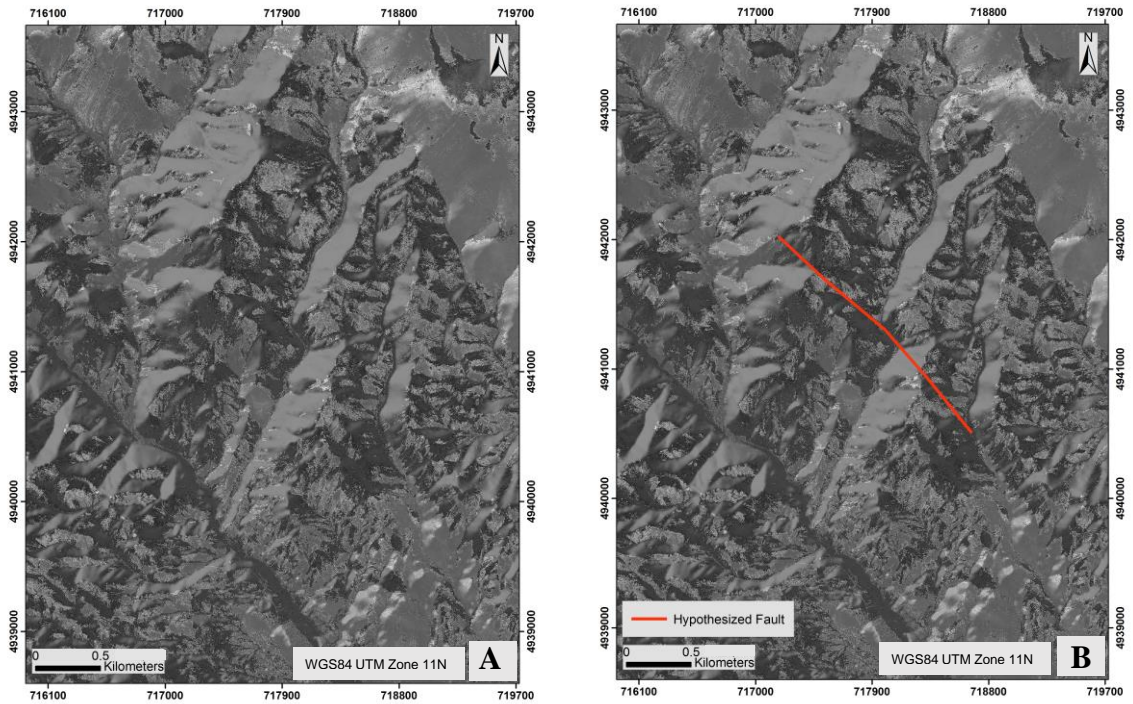


**Figure 10:** WorldView New Iron Index of the western study area. Maps A and B are identical, map B is overlain by the hypothesized fault. Image Source: Worldview-2 satellite images courtesy of the DigitalGlobe Foundation.

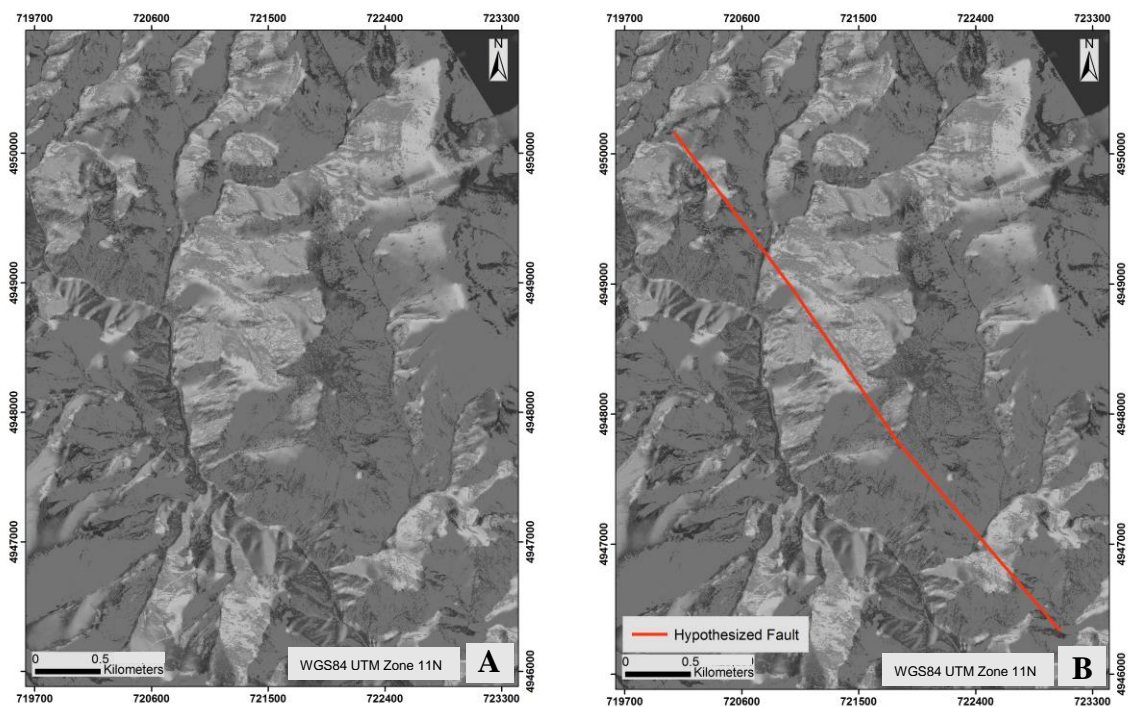


**Figure 11 (Previous Page):** WorldView New Iron Index of the eastern study area. Maps A and B are identical, map B is overlain by the hypothesized fault. Image Source: Worldview-2 satellite images courtesy of the DigitalGlobe Foundation.

In the results for the Non-Homogeneous Feature Index of the western study area (Figure 12), lineations in the brightness values were observed along the trend of the hypothesized fault as well as shifts in drainage patterns. There was evidence of lithologic offset, but just like in the WorldView New Iron Index, these trends related to the north aspects of slopes, and so it was likely an artifact from shadowing. In the Non-Homogeneous Feature Index result for the eastern study area (

Figure 13), the hypothesized fault occurred along a linear trend of brightness value changes, where dramatically different brightness values were divided by the hypothesized fault. When comparing this index result to Google Earth imagery, the dark pixels corresponded to shadowed areas (due to the terrain or presence of trees), intermediate pixels related to areas with scrubby or sparse vegetation, while light pixels corresponded to drainages and washes that lacked vegetation.

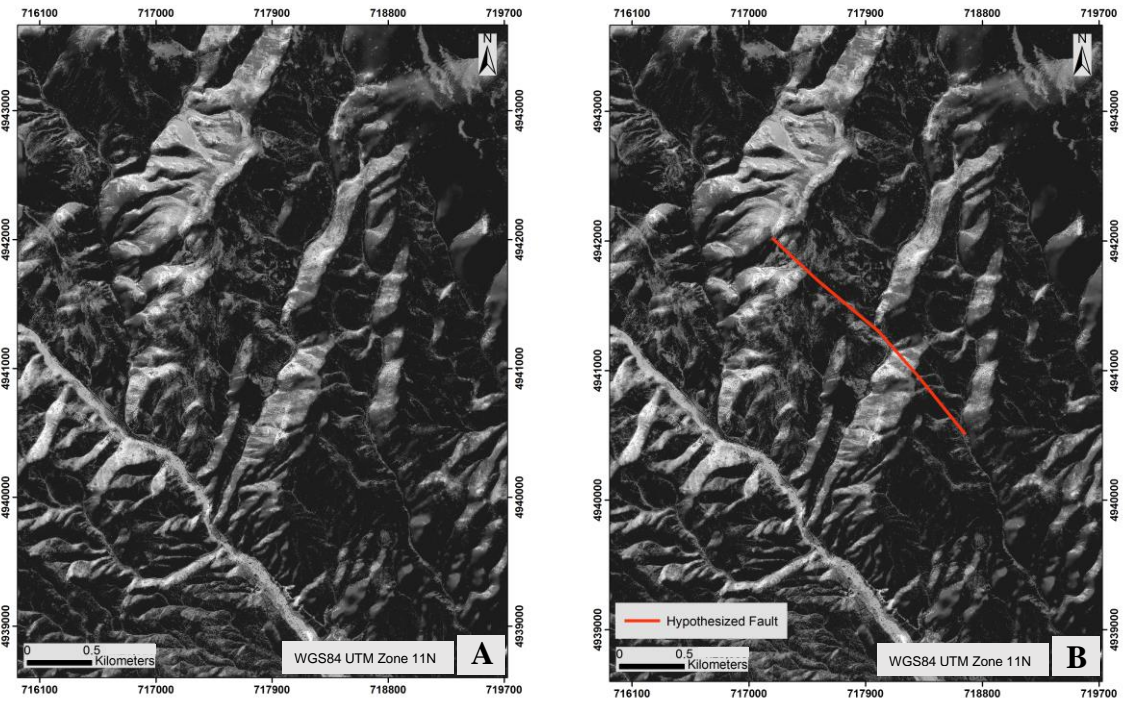


**Figure 12:** WorldView Non-Homogeneous Feature Index of the western study area. Maps A and B are identical, except map B is overlain by the hypothesized fault. Image Source: Worldview-2 satellite images courtesy of the DigitalGlobe Foundation.

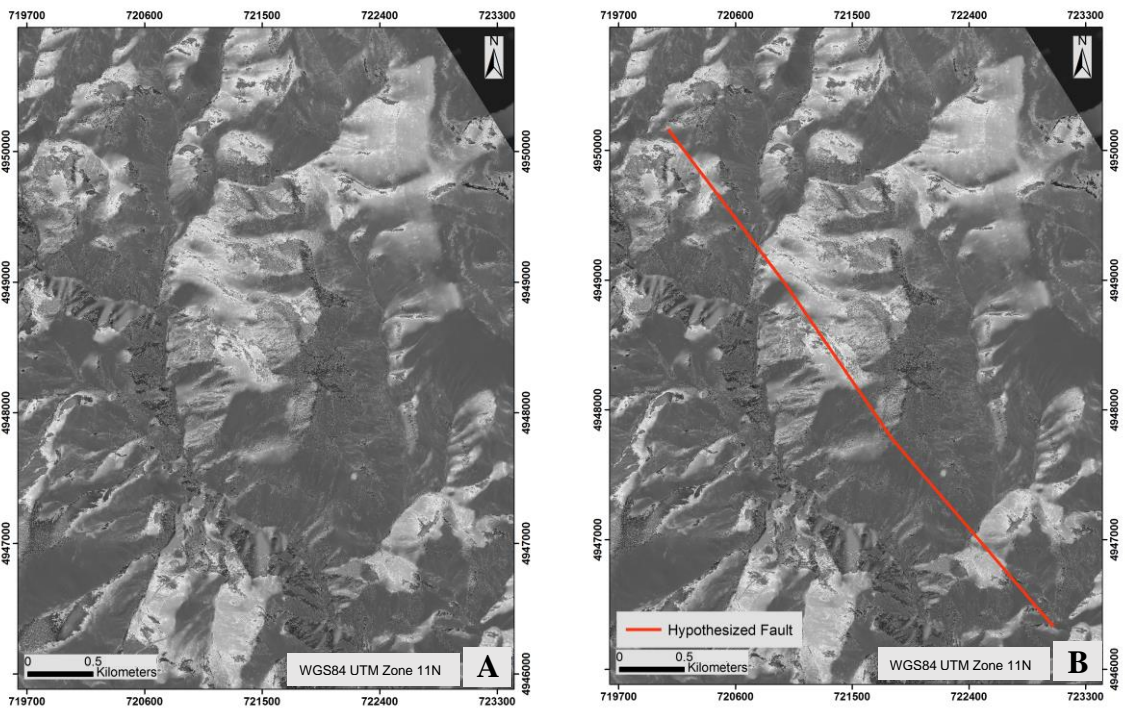


**Figure 13 (Previous Page):** WorldView Non-Homogeneous Feature Index of the eastern study area. Maps A and B are identical, except map B is overlain by the hypothesized fault. Image Source: Worldview-2 satellite images courtesy of the DigitalGlobe Foundation.

In the western study area for the WorldView Improved Vegetation Index (Figure 14) high brightness values correspond to the presence of vegetation. Lineaments in vegetation patterns (and hence changes in vegetation patterns) correspond to the location of the hypothesized fault. Vegetation is also enhanced that corresponds to a drainage that shifts suddenly as it crosses over the hypothesized fault. In the WorldView Improved Iron Index result for the eastern study area (Figure 15) linear changes in vegetation patterns are observed along the path of the hypothesized fault. When this index result is compared to Google Earth's imagery, the brightest pixels correspond to trees, intermediate pixels respond to scrubby vegetation, dark-intermediate respond to bare rock, and the darkest pixels correspond to shadowed areas.

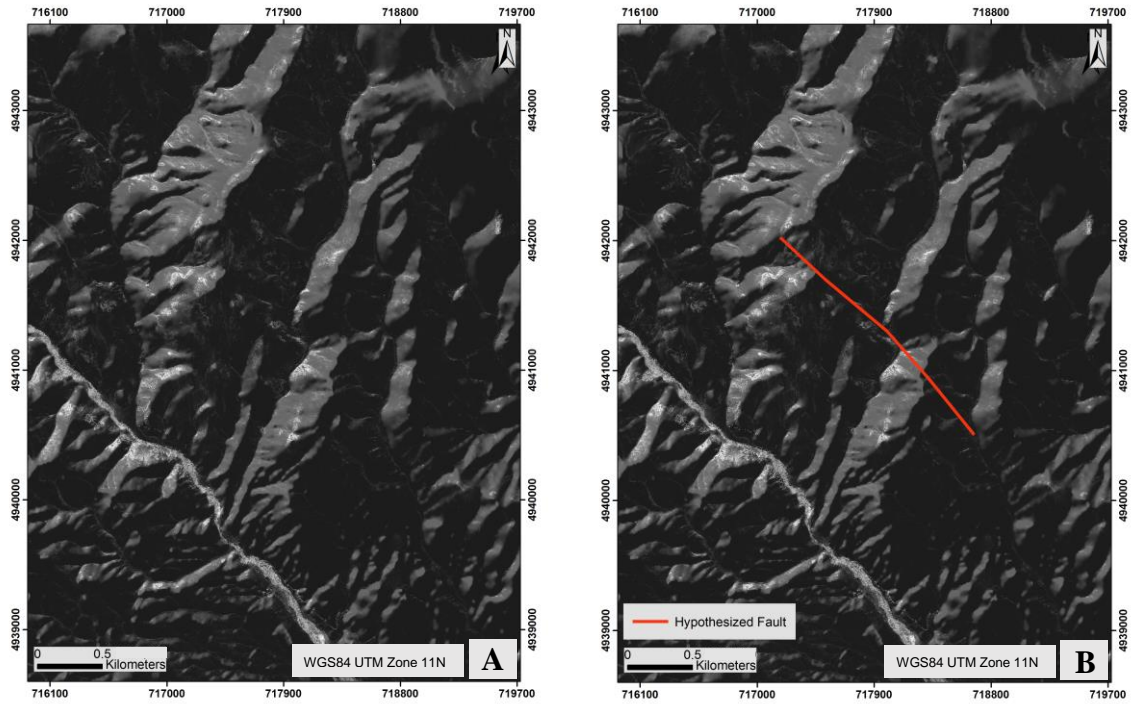


**Figure 14:** WorldView-2 Improved Vegetation Index of the western study area. Maps A and B are identical, except map B is overlain by the hypothesized fault location. Image Source: Worldview-2 satellite images courtesy of the DigitalGlobe Foundation.

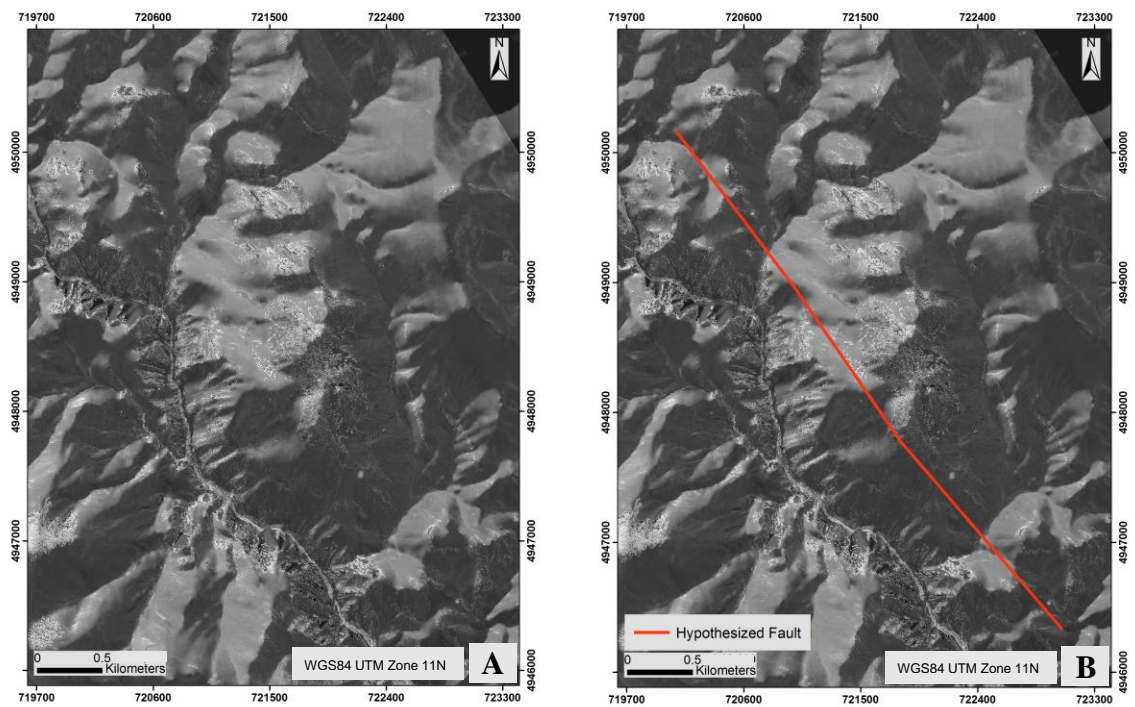


**Figure 15 (Previous Page):** WorldView Improved Vegetation Index of the eastern study area. Maps A and B are identical, except map B is overlain by the hypothesized fault location. Image Source: Worldview-2 satellite images courtesy of the DigitalGlobe Foundation.

In the western study area for the Optimized Soil Adjusted Vegetation Index (OSAVI) result (Figure 16), neither lineaments nor changes in vegetation were observed that corresponded to the hypothesized fault. In the eastern study area OSAVI result (Figure 17), linear patterns in vegetation changes were observed that corresponded to the hypothesized fault, either as areas of high vegetation or dividing changes in vegetation. When this index result was compared to Google Earth's imagery, the brightest pixels corresponded to trees, intermediate pixels corresponded to scrubby vegetation, dark-intermediate corresponded to bare rock, and the darkest pixels corresponded to shadowed areas.

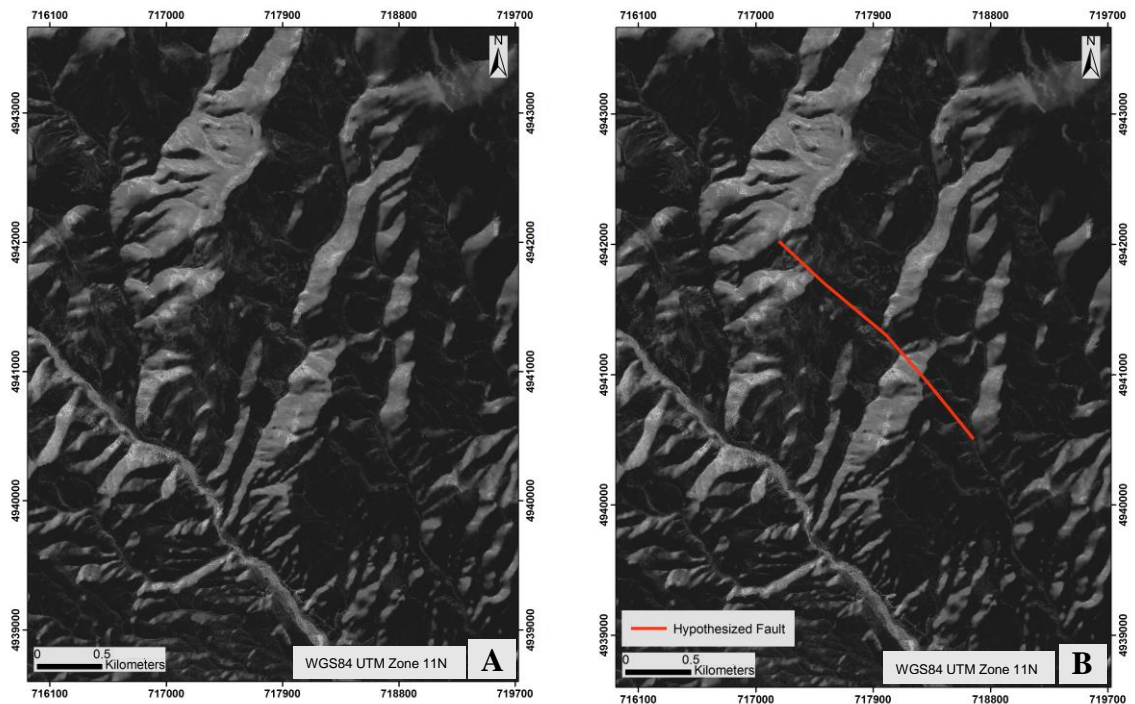


**Figure 16 (Previous Page):** Optimized Soil Adjusted Vegetation Index of the western study area. Maps A and B are identical, except map B is overlain by the hypothesized fault. Image Source: Worldview-2 satellite images courtesy of the DigitalGlobe Foundation.

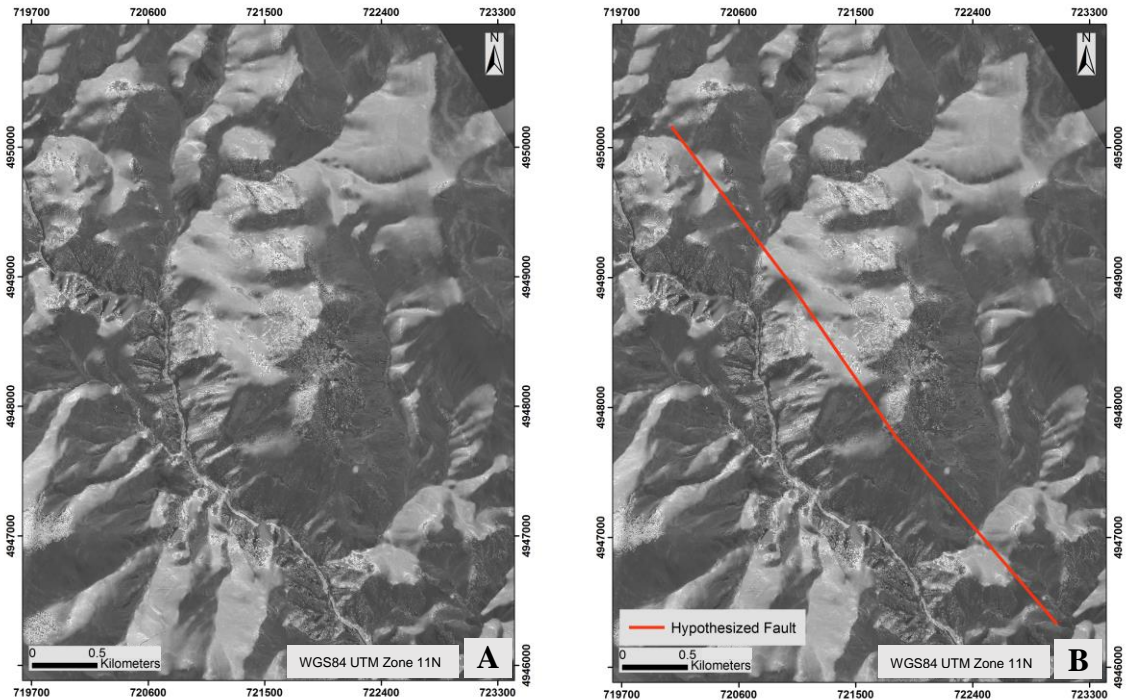


**Figure 17:** Optimized Soil Adjusted Vegetation Index of the eastern study area. Maps A and B are identical, except map B is overlain by the hypothesized fault. Image Source: Worldview-2 satellite images courtesy of the DigitalGlobe Foundation.

### *ASTER*

The accuracy results from the confusion matrices of the ASTER classifications are presented in Table 8. The Maximum likelihood analysis classification had an overall accuracy of 96.22% and a kappa coefficient of 0.94 and the support vector machine (SVM) classification had an overall accuracy of 94.83% and a kappa coefficient of 0.92. Both MLA and SVM classifications were dominated by intermediate-mafic and felsic-intermediate compositions, while alluvium, sedimentary and metamorphosed sedimentary rocks made up a small component of the results. The minimum distance (MD)

classification had an overall accuracy of 72.21% and a kappa coefficient of 0.60. The MD results were more compositionally diverse than the other two classification techniques.

**Table 8:** Results from the ASTER classification confusion matrices. The classes are alluvium (**A**), felsic-intermediate (**FI**), intermediate mafic (**IM**), meta-sedimentary (**MS**), and sedimentary (**S**). The columns are commission percent (**c**), omission percent (**o**), user accuracy percent (**u**), and producer accuracy percent (**p**).

Method	SVM				MLA				MD			
Overall Accuracy	94.83%				96.22%				72.21%			
Kappa Coefficient	0.92				0.94				0.60			
Class	c	o	u	p	c	o	u	p	c	o	u	p
A	13.57	2.55	97.45	86.43	0.32	0.00	100.00	99.68	45.60	0.00	100	54.40
FI	3.14	4.15	95.85	96.86	1.73	4.34	95.66	98.27	7.04	29.82	70.18	92.96
MI	3.14	2.75	97.25	96.84	2.93	2.71	97.29	97.07	1.80	11.42	88.58	98.20
MS	13.50	17.88	82.12	86.50	18.60	9.35	90.65	81.40	88.61	84.86	15.14	11.39
S	18.73	16.10	83.90	81.27	10.78	1.49	98.51	89.22	85.53	59.60	40.40	14.47

In results for the western area, there were very few pixels classified as metamorphosed sedimentary rocks. However, in the eastern study area, a significant portion of the study area was classified as metamorphosed sedimentary rock. The intermediate-mafic classification was more prevalent in the western study area, where it appeared to correspond to areas with moderate topographic relief and higher elevations. In the eastern study area, pixels with an intermediate classification composed a relatively small area. In both study areas, the felsic-intermediate classification comprised a large portion of the study area, where it tended to form relatively rounded hills and gentle topography. In the eastern study area, there are a few small patches that were classified as sedimentary, corresponded to topographic lows. In the western study area, the pixels that

were classified as sedimentary appeared to skirt around the metamorphosed sedimentary classification. In these classifications, either no pixels were classified as alluvium in either study area or they composed areas that were otherwise classified as sedimentary.

In the Maximum Likelihood Analysis result for the western study area (Figure 18), the Support Vector Machine classification for the western study area (Figure 20), and the Minimum Distance Classification result for the western study area (Figure 22), lineaments were observed as the changes in lithology on either side of the hypothesized fault, but no offset lithologies were definitively inferred from this classification. A second piece of evidence for a fault that was observed in this classification was a shift in the drainage course, where the felsic-intermediate classification mimics the drainage and abruptly changes course as it intersects the hypothesized fault. In the Maximum Likelihood Analysis result for the eastern study area (Figure 19), the Support Vector Machine result for the eastern study area (Figure 21), and the Minimum Distance result for the eastern study area (

Figure 23), lineaments were observed as lithologic changes appeared to occur along the trend of the hypothesized fault. There were some minor shifts in lithologies that were observed, but they are too subtle to serve as definitive evidence for the presence of a fault. There were no changes in drainage courses that corresponded to the hypothesized fault in this study area.

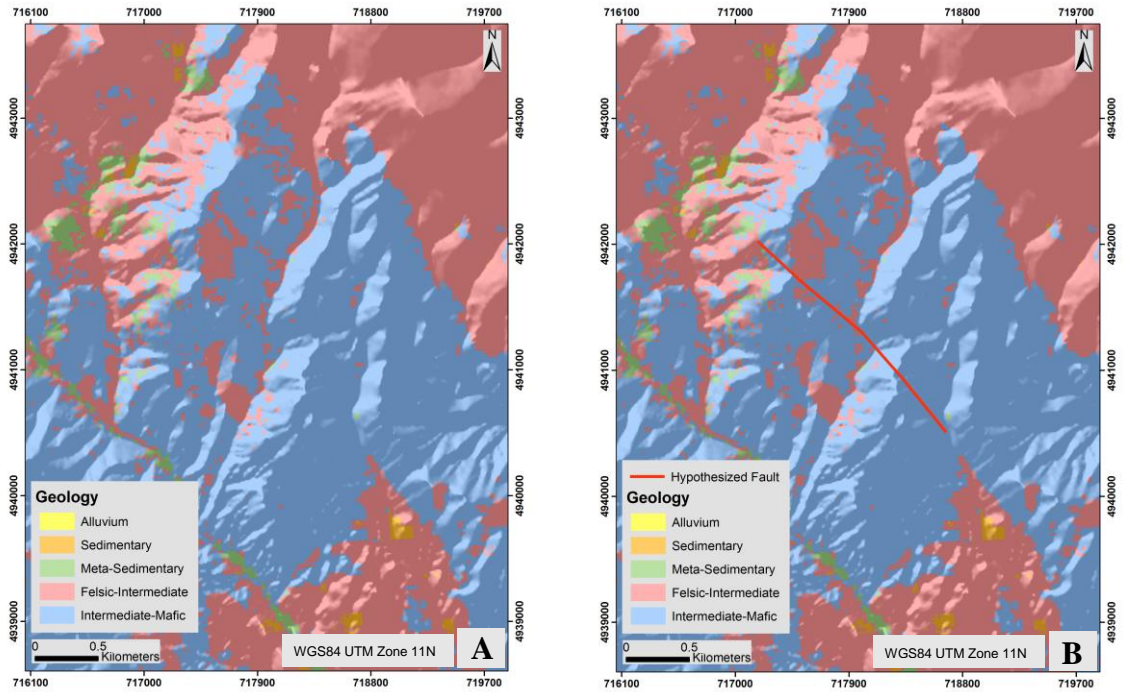


**Figure 18:** ASTER Maximum Likelihood Analysis (MLA) classification of the western study area. The MLA results have an overall accuracy of 96.22% and a kappa coefficient of 0.94. Maps A and B are identical, map B is overlain by the hypothesized fault that was identified in the WorldView-2 data. Image Source: ASTER data products were retrieved from the online Data Pool, courtesy of the NASA Land Processes Distributed Active Archive Center (LP DAAC), USGS/Earth Resources Observation and Science (EROS) Center, Sioux Falls, South Dakota, [https://lpdaac.usgs.gov/data\\_access/data\\_pool](https://lpdaac.usgs.gov/data_access/data_pool)

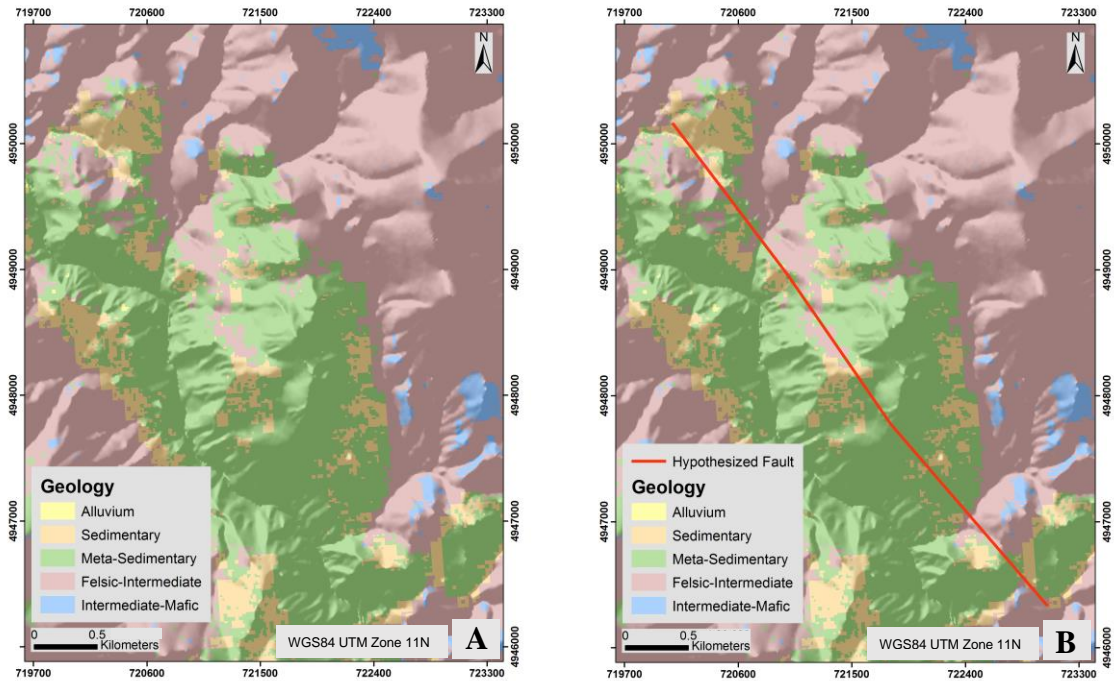


**Figure 19:** ASTER Maximum Likelihood Analysis (MLA) classification of the eastern study area. The MLA results have an overall accuracy of 96.22% and a kappa coefficient of 0.94. Maps A and B are identical, map B is overlain by the hypothesized fault that was identified in the WorldView-2 data. Image Source: ASTER data products were retrieved from the online Data Pool, courtesy of the NASA Land Processes Distributed Active Archive Center (LP DAAC), USGS/Earth Resources Observation and Science (EROS) Center, Sioux Falls, South Dakota, [https://lpdaac.usgs.gov/data\\_access/data\\_pool](https://lpdaac.usgs.gov/data_access/data_pool)

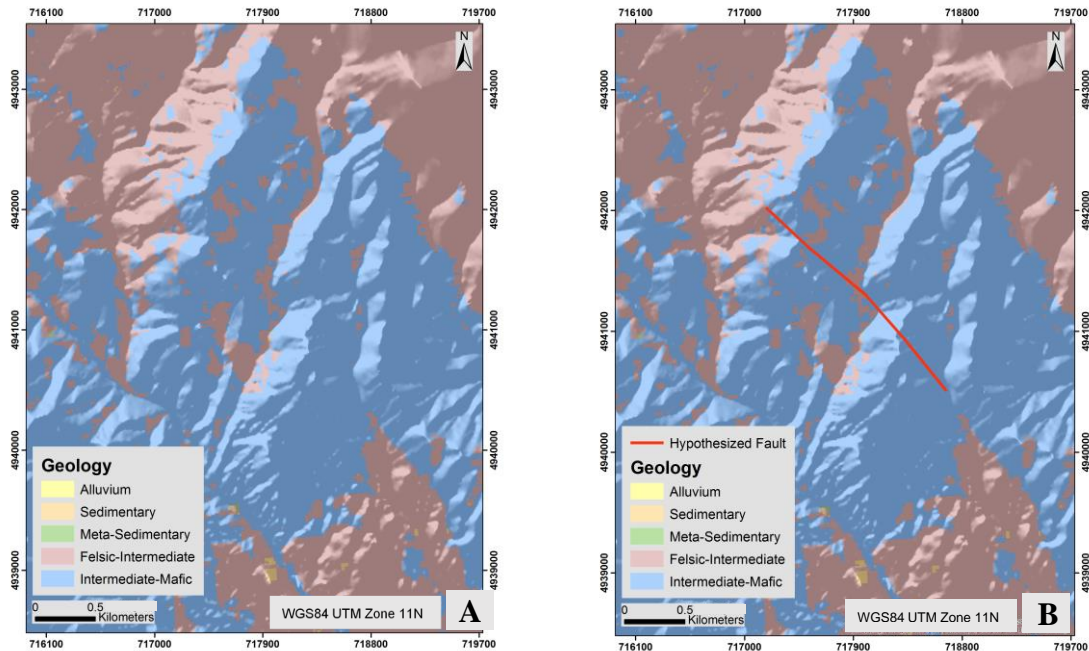


**Figure 20:** ASTER Support Vector Machine (SVM) classification of the western study area. The SVM results have an overall accuracy of 94.83% and a kappa coefficient of 0.92. Maps A and B are identical, except map B is overlain by the hypothesized fault that was identified in the WorldView-2 data. Image Source: ASTER data products were retrieved from the online Data Pool, courtesy of the NASA Land Processes Distributed Active Archive Center (LP DAAC), USGS/Earth Resources Observation and Science (EROS) Center, Sioux Falls, South Dakota, [https://lpdaac.usgs.gov/data\\_access/data\\_pool](https://lpdaac.usgs.gov/data_access/data_pool)

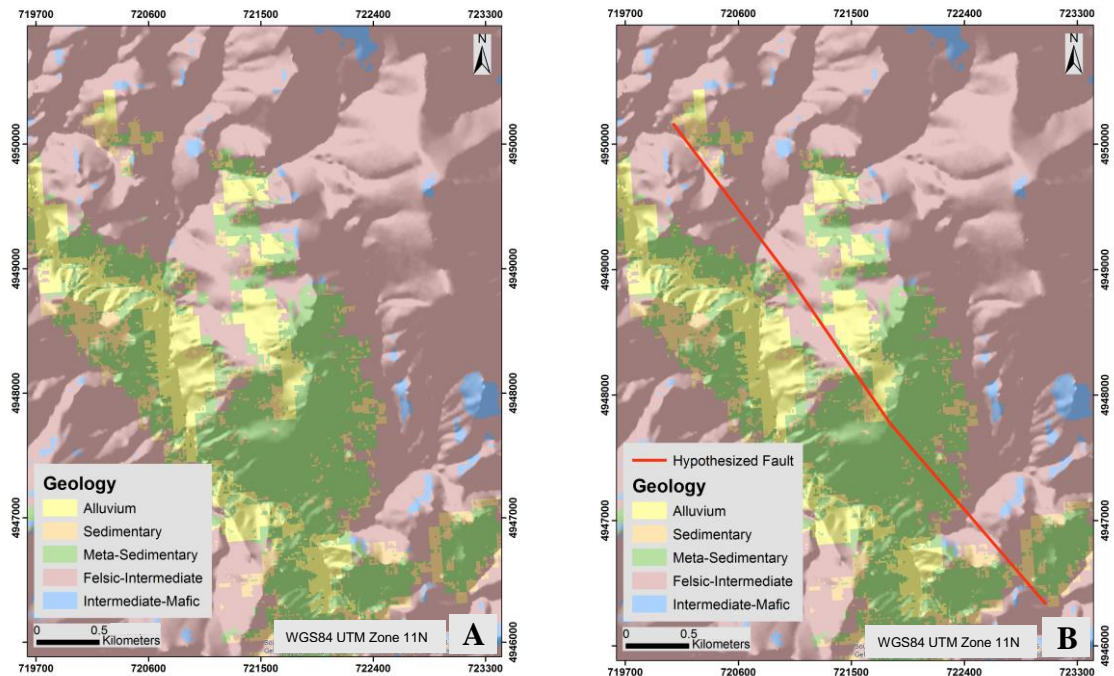


**Figure 21:** ASTER Support Vector Machine (SVM) classification of the eastern study area. The SVM results have an overall accuracy of 94.83% and a kappa coefficient of 0.92. Maps A and B are identical, except map B is overlain by the hypothesized fault that was identified in the WorldView-2 data. Image Source: ASTER data products were retrieved from the online Data Pool, courtesy of the NASA Land Processes Distributed Active Archive Center (LP DAAC), USGS/Earth Resources Observation and Science (EROS) Center, Sioux Falls, South Dakota, [https://lpdaac.usgs.gov/data\\_access/data\\_pool](https://lpdaac.usgs.gov/data_access/data_pool)

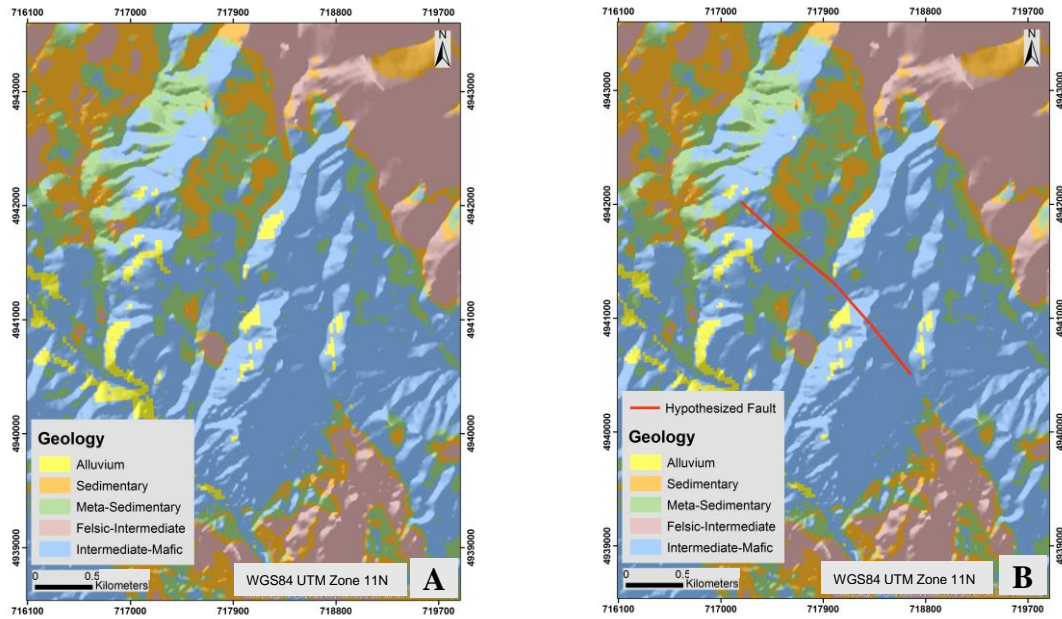


**Figure 22:** ASTER Minimum Distance (MD) classification of the western study area. The MD results have an overall accuracy of 72.21% and a kappa coefficient of 0.60. Maps A and B are identical, except map B is overlain by the hypothesized fault that was identified in the WorldView-2 data. Image Source: ASTER data products were retrieved from the online Data Pool, courtesy of the NASA Land Processes Distributed Active Archive Center (LP DAAC), USGS/Earth Resources Observation and Science (EROS) Center, Sioux Falls, South Dakota, [https://lpdaac.usgs.gov/data\\_access/data\\_pool](https://lpdaac.usgs.gov/data_access/data_pool)

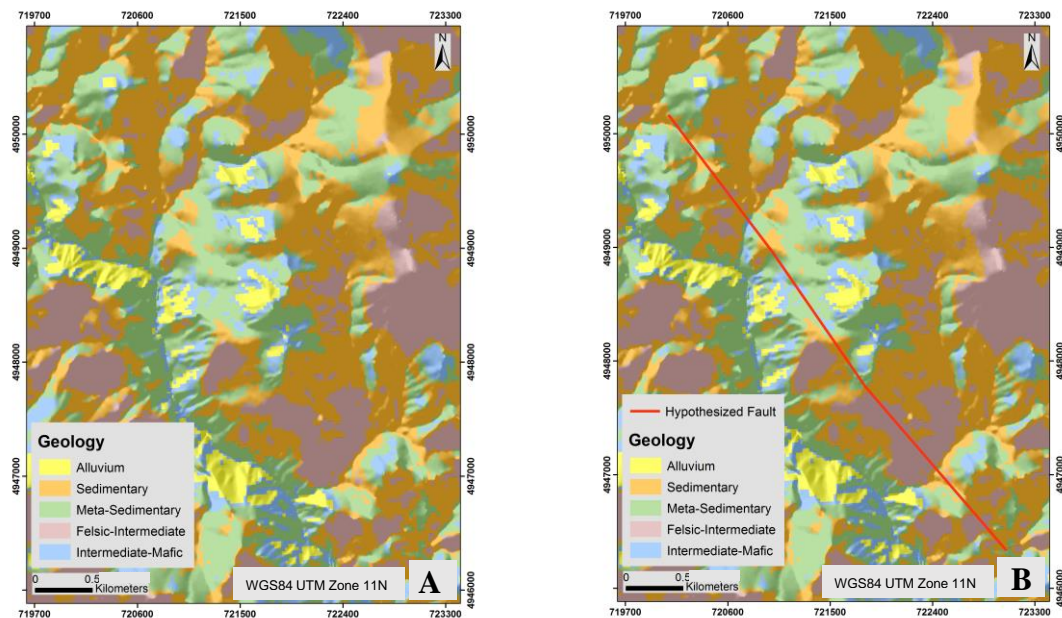


**Figure 23 (Previous Page):** ASTER Minimum Distance (MD) classification of the eastern study area. The MD results have an overall accuracy of 72.21% and a kappa coefficient of 0.60. Maps A and B are identical, except map B is overlain by the hypothesized fault that was identified in the WorldView-2 data. Image Source: ASTER data products were retrieved from the online Data Pool, courtesy of the NASA Land Processes Distributed Active Archive Center (LP DAAC), USGS/Earth Resources Observation and Science (EROS) Center, Sioux Falls, South Dakota, [https://lpdaac.usgs.gov/data\\_access/data\\_pool](https://lpdaac.usgs.gov/data_access/data_pool)

*Sentinel-2*

The accuracy results from the confusion matrices of the Sentinel-2 classifications are presented in Table 9. The Maximum Likelihood Analysis classification had an overall accuracy of 89.09% and a kappa coefficient of 0.83 and the Support Vector Machine classification had an overall accuracy of 90.13% and a kappa coefficient of 0.84. Both Maximum Likelihood Analysis and Support Vector Machine classifications produced similar results and were dominated by intermediate-mafic and felsic-intermediate compositions, while alluvium, sedimentary and metamorphosed sedimentary rocks made

**Table 9:** Results from the Sentinel-2 classification confusion matrices. The classes are alluvium (**A**), felsic-intermediate (**FI**), intermediate mafic (**IM**), meta-sedimentary (**MS**), and sedimentary (**S**). The columns are commission percent (**c**), omission percent (**o**), user accuracy percent (**u**), and producer accuracy percent (**p**).

Method	SVM				MLA				MD			
Overall Accuracy	90.13%				89.09%				71.36%			
Kappa Coefficient	0.84				0.83				0.58			
Class	c	o	u	p	c	o	u	p	c	o	u	p
A	0.00	0.00	100.00	100.00	0.00	0.00	100.00	100.00	0.00	7.94	92.06	100.00
FI	10.48	4.73	95.27	89.52	2.14	12.71	87.29	97.86	10.91	26.77	73.23	89.09
MI	6.35	3.50	96.50	93.65	8.00	7.24	92.76	92.00	17.10	17.87	82.13	82.90
MS	20.93	62.84	37.16	79.07	28.04	25.68	74.32	71.96	90.27	84.15	15.85	9.73
S	24.00	31.79	68.21	76.00	45.97	7.18	92.82	54.03	72.57	50.77	49.23	27.43

up a lesser extent in the results. The Minimum Distance classification had an overall accuracy of 71.36% and a kappa coefficient of 0.58. The minimum distance results were more compositionally diverse than the other two classification techniques.

In these results for the western area, pixels classified as having a metamorphosed sedimentary composition appeared to skirt around the pixels classified as intermediate-mafic. The intermediate-mafic classification was prevalent in both study areas where it appeared to correspond to areas with moderate to high topographic relief and higher elevations. In both study areas, the felsic-intermediate classification composed a large portion of the study area, where it tended to form relatively rounded hills and gentle topography. In the eastern study area, the pixels classified as sedimentary corresponded to topographic lows. In the western study area, the pixels that were classified as sedimentary appeared to skirt around the metamorphosed sedimentary classification. In these classifications, either no pixels were classified as alluvium in either study area or they composed areas that are otherwise classified as sedimentary.

In the Support Vector Machine classification for the western study area (Figure 24), the Maximum Likelihood Analysis result for the western study area (Figure 26), and the Minimum Distance Classification result for the western study area (Figure 28), lineaments were observed as the changes in lithology on either side of the hypothesized fault, but no offset lithologies were definitively inferred from this classification. A second piece of evidence for a fault that was observed in this classification was a shift in the drainage course, where the felsic-intermediate classification mimicked the drainage and abruptly changed course as it intersects the hypothesized fault. In the Support Vector Machine result for the eastern study area (Figure 25) and the Maximum Likelihood

Analysis result for the eastern study area (Figure 27), lineaments were observed as lithologic changes appeared to occur along the trend of the hypothesized fault. There were some minor shifts in lithologies that were observed, but they were too subtle to serve as definitive evidence for the presence of a fault. In the Minimum Distance result for the eastern study area (Figure 29), there were lineaments observed as lithologic changes that occurred along the trend of the hypothesized fault, but no evidence of lithologic offset. There were no changes in drainage courses that correspond to any of the hypothesized faults in eastern study area.

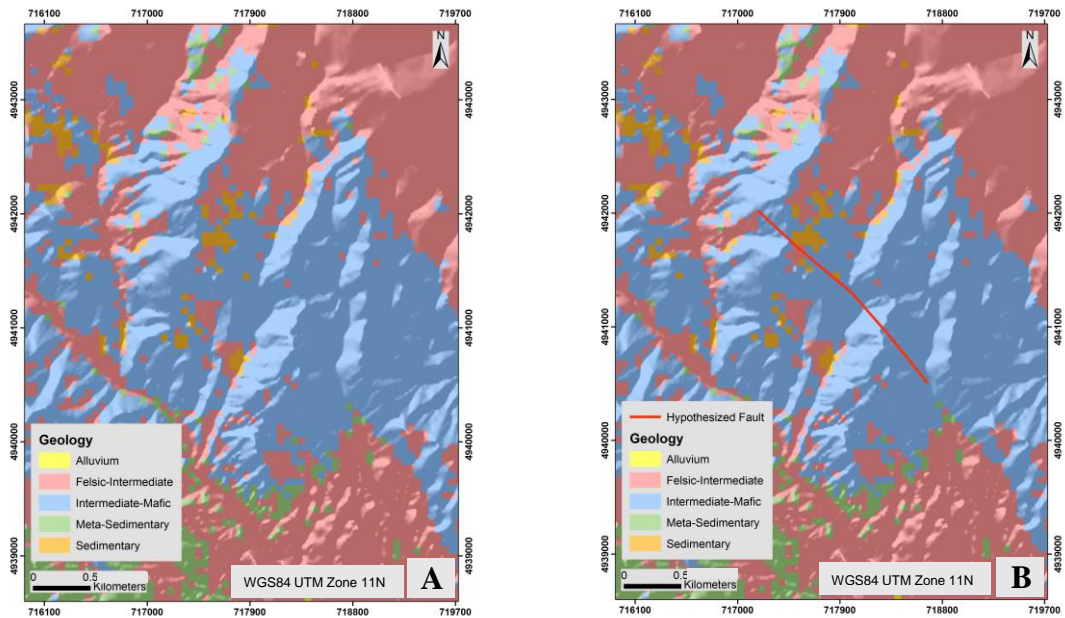


**Figure 24:** Sentinel-2 Support Vector Machine (SVM) classification of the western study area. The SVM results have an overall accuracy of 90.12% and a kappa coefficient of 0.84. Maps A and B are identical, except map B is overlain by the hypothesized fault that was identified in the WorldView-2 data. Image Source: Sentinel-2: Contains modified Copernicus Sentinel data [2016].

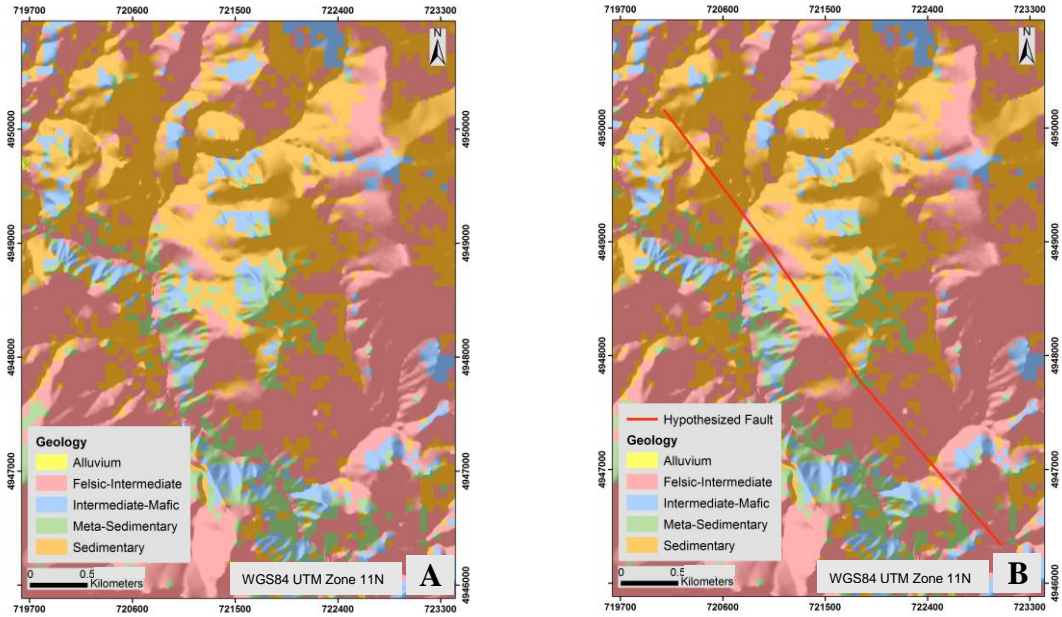


**Figure 25:** Sentinel-2 Support Vector Machine (SVM) classification of the eastern study area. The SVM results have an overall accuracy of 90.12% and a kappa coefficient of 0.84. Maps A and B are identical, except map B is overlain by the hypothesized fault that was identified in the WorldView-2 data. Image Source: Sentinel-2: Contains modified Copernicus Sentinel data [2016].

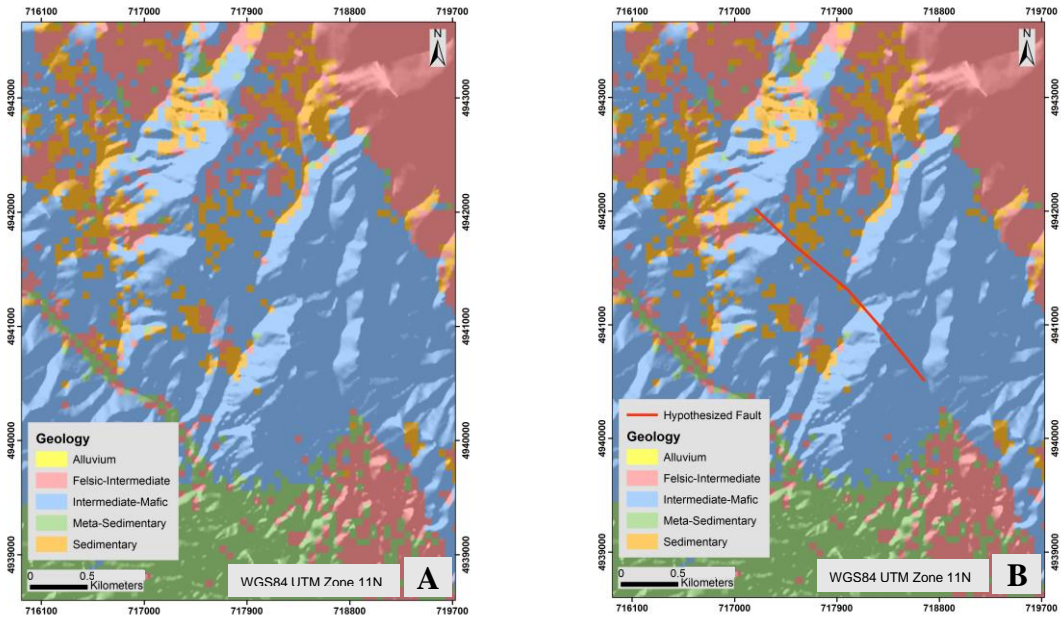


**Figure 26 (Previous Page):** Sentinel-2 Maximum Likelihood Analysis (MLA) classification of the western study area. The MLA results have an overall accuracy of 89.09% and a kappa coefficient of 0.83. Maps A and B are identical, except map B is overlain by the hypothesized fault that was identified in the WorldView-2 data. Image Source: Sentinel-2: Contains modified Copernicus Sentinel data [2016].

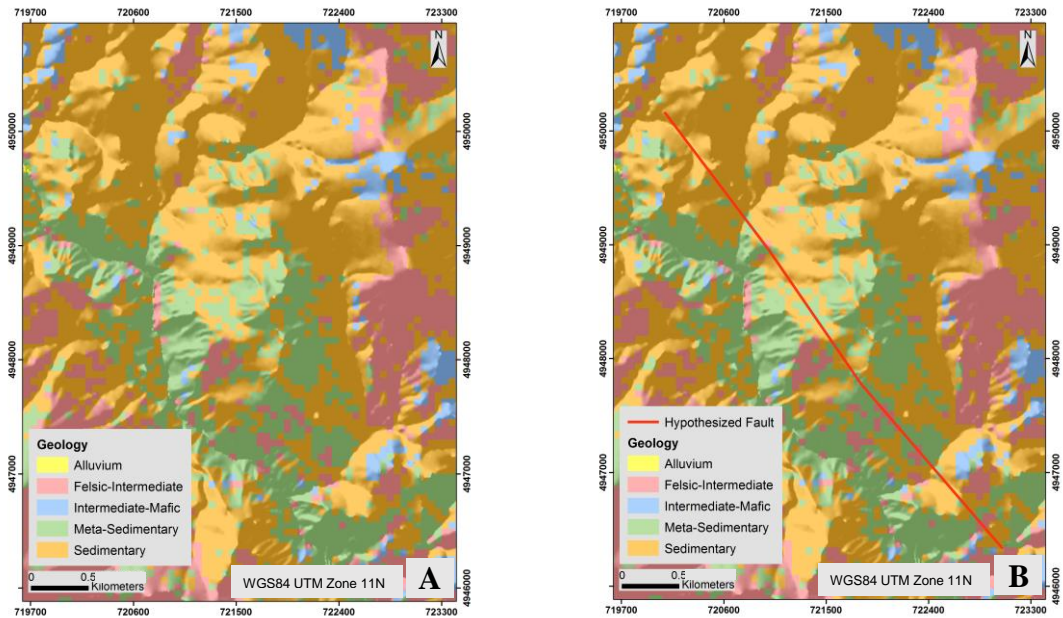


**Figure 27:** Sentinel-2 Maximum Likelihood Analysis (MLA) classification of the eastern study area. The MLA results have an overall accuracy of 89.09% and a kappa coefficient of 0.83. Maps A and B are identical, except map B is overlain by the hypothesized fault that was identified in the WorldView-2 data. Image Source: Sentinel-2: Contains modified Copernicus Sentinel data [2016].

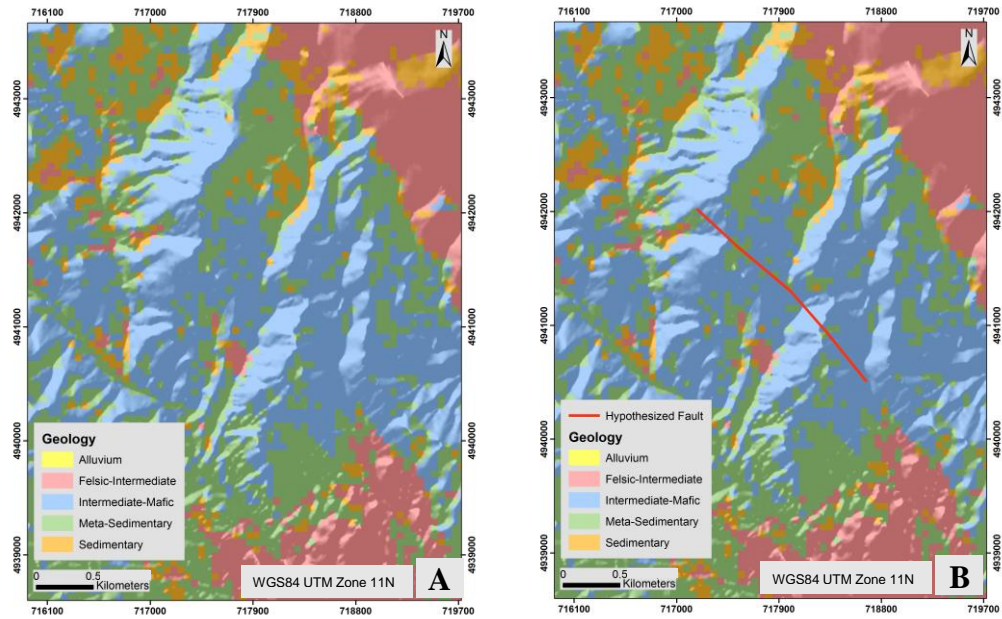


**Figure 28:** Sentinel-2 Minimum Distance (MD) classification of the western study area. The MD results have an overall accuracy of 71.36% and a kappa coefficient of 0.58. Maps A and B are identical, except map B is overlain by the hypothesized fault that was identified in the WorldView-2 data. Image Source: Sentinel-2: Contains modified Copernicus Sentinel data [2016].

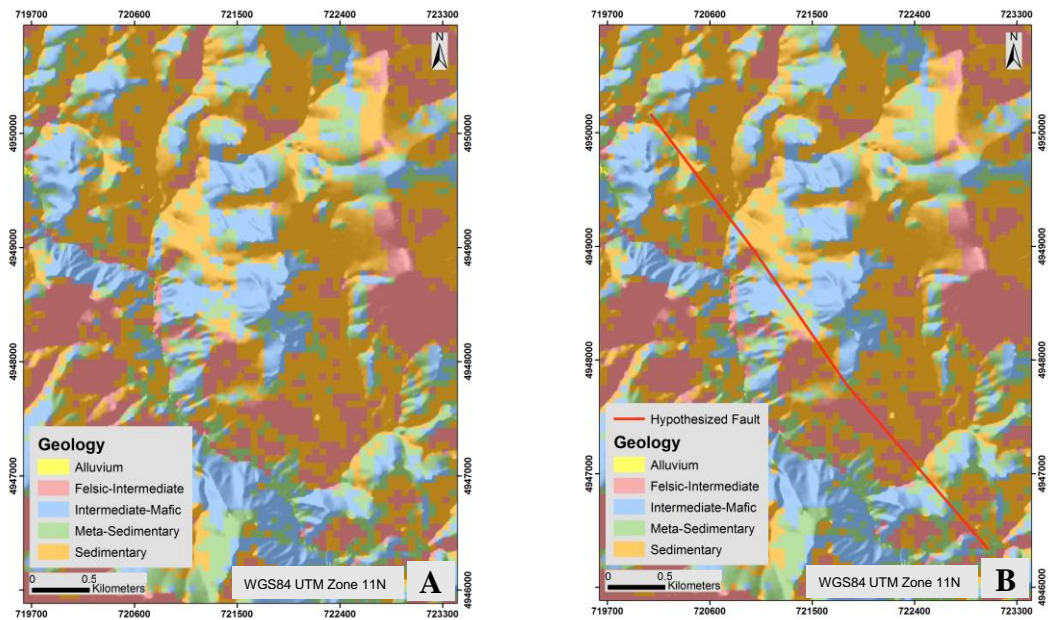


**Figure 29 (Previous Page):** Sentinel-2 Minimum Distance (MD) classification of the eastern study area. The MD results have an overall accuracy of 71.36% and a kappa coefficient of 0.58. Maps A and B are identical, except map B is overlain by the hypothesized fault that was identified in the WorldView-2 data. Image Source: Sentinel-2: Contains modified Copernicus Sentinel data [2016].

### NAIP

In the natural color NAIP results for the western study area (Figure 30), lineaments of lithologic changes between the lighter and darker colored lithologies were identified, as well as a shift in the drainage course that corresponds to its intersection with the hypothesized fault. Changes in vegetation were not observed in this result, nor were any lithologic offsets. In the natural color NAIP result for the eastern study area (Figure 31), lineaments were also observed as changes in light and dark lithologies on either side of the hypothesized fault, as well as an increased amount of vegetation that corresponded with the location of the hypothesized fault. No lithologic offset was observed, nor were any changes in drainage courses corresponding to the hypothesized fault.

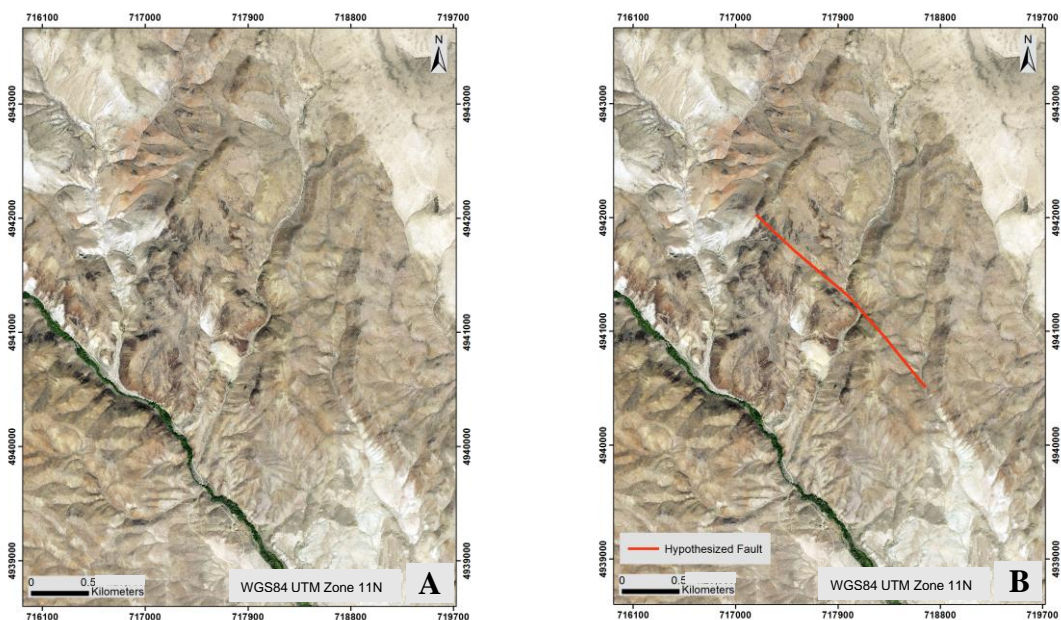


**Figure 30 (Previous Page):** Natural color NAIP imagery of the western study area; band 3 (red), band 2 (green), band 1 (blue). Maps A and B are identical, except the map B is overlain by the hypothesized fault that was identified in the WorldView-2 data. Image Source: NAIP: U. S. Department of Agriculture, Farm Service Agency.

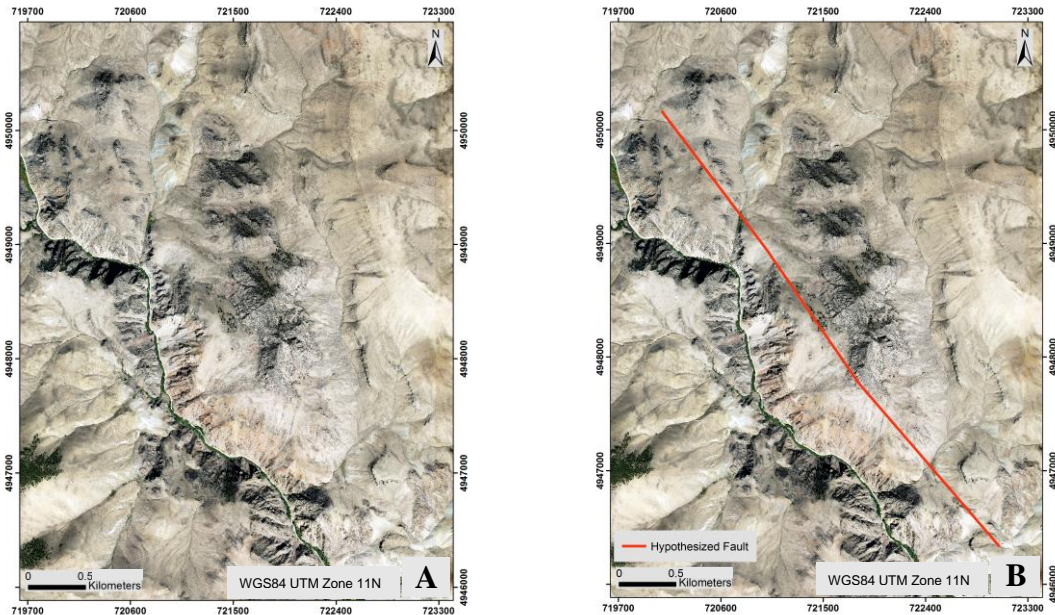


**Figure 31:** Natural color NAIP imagery of the eastern study area; band 3 (red), band 2 (green), band 1 (blue). Maps A and B are identical, except the map B is overlain by the hypothesized fault that was identified in the WorldView-2 data. Image Source: NAIP: U. S. Department of Agriculture, Farm Service Agency.

In the NDVI result for the western study area (Figure 32), lineaments were observed as increased vegetation health that corresponded to the hypothesized fault and a sudden change in the drainage course was enhanced by the presence of healthy vegetation. In the NDVI result for the eastern study area (Figure 33), lineaments were also observed as increased vegetation health that corresponded with the location of the hypothesized fault, but no shifts in drainage courses were observed.

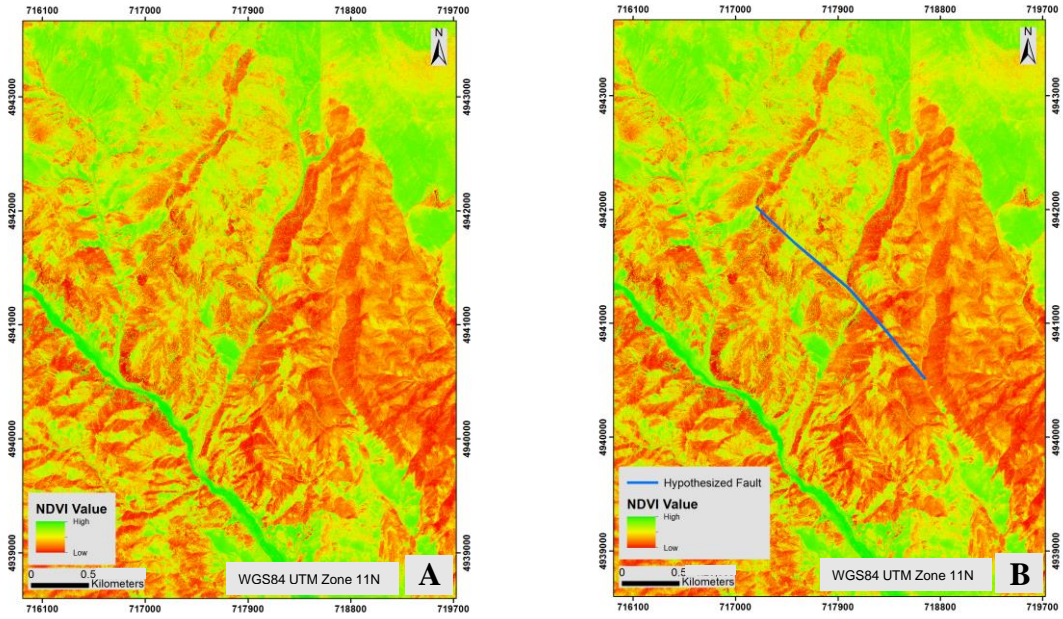


**Figure 32:** NAIP Normalized Difference Vegetation Index of the western study area with a histogram equalize stretch applied. High NDVI values are shown in green and low values are shown in red. Maps A and B are identical, except map B is overlain by the hypothesized fault that was identified in the WorldView-2 data. Image Source: NAIP: U. S. Department of Agriculture, Farm Service Agency.

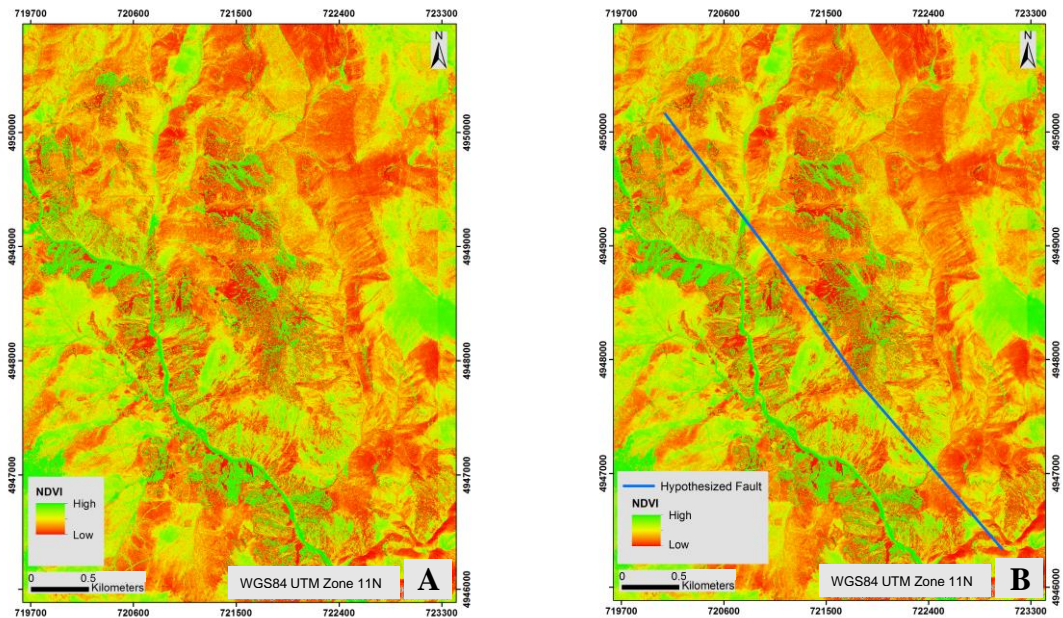


**Figure 33 (Previous Page):** NAIP Normalized Difference Vegetation Index of the eastern study area with a histogram equalize stretch applied. High NDVI values are shown in green and low values are shown in red. Maps A and B are identical, except map B is overlain by the hypothesized fault that was identified in the WorldView-2 data. Image Source: NAIP: U. S. Department of Agriculture, Farm Service Agency.

In the decorrelation stretch results for both areas, vegetation appeared with a red coloration, and the surface lithologies were blue, purple, green and yellow. In the western study area (Figure 34), there are lineaments in the apparent lithologies, where linear contacts between the light and dark colored pixels correspond to the hypothesized fault. The drainage course was expressed by a meander of yellow pixels that passed through an area dominated by blue and purple pixels. Changes in this drainage course were observed and correspond to its intersection with the hypothesized fault. No changes in vegetation were observed. In the eastern study area (Figure 35), lineaments were observed as changes in pixel colorations that are divided by the location of the hypothesized fault. Changes in vegetation were also observed as anomalous red pixels that corresponded with the location of the hypothesized fault. There were no observable lithological offsets or shifts in drainage patterns. In the east areas, high decorrelated near infrared values tended to be present on the northeastern side of the fault as well as in Darling Creek, to the west. Excluding Darling Creek, on the western side of the west study areas, decorrelated near infrared values were generally lower in the western study area than the eastern area. When comparing these results to Google Earth imagery, high decorrelated near infrared values correspond to stands of trees.

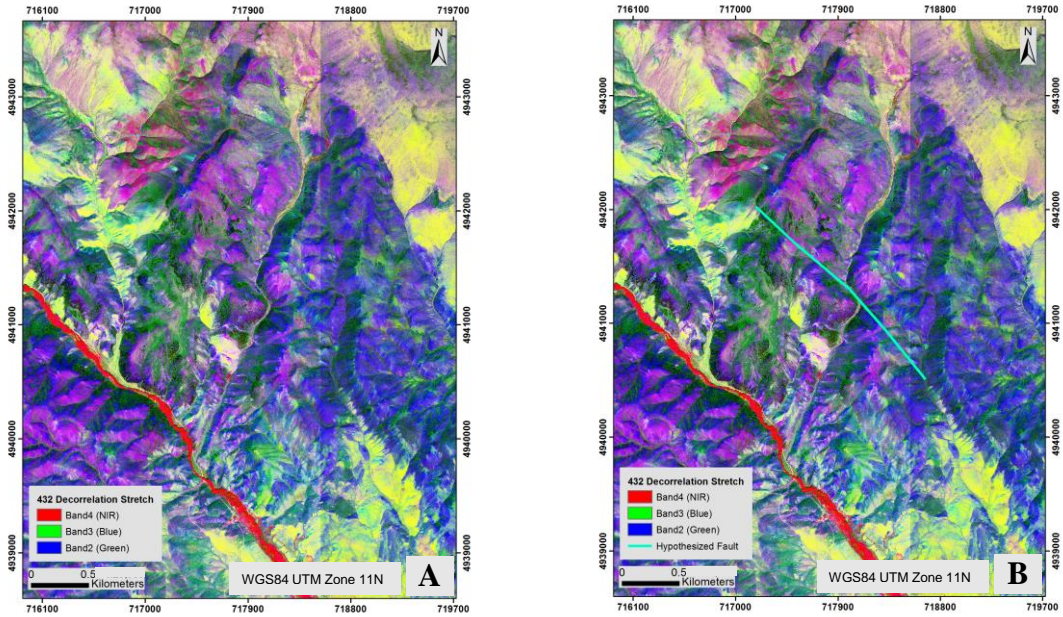


**Figure 34:** NAIP decorrelation stretch image of the western study area, using band 4, band 3, and band 2, with a histogram equalize stretch applied. The color representation on these RGB composite images are the decorrelated band 4 in red, the decorrelated band 3 in green, and the decorrelated band 2 in blue. Maps A and B are identical, except map B is overlain by the hypothesized fault that was identified in the WorldView-2 data. Image Source: NAIP: U. S. Department of Agriculture, Farm Service Agency.

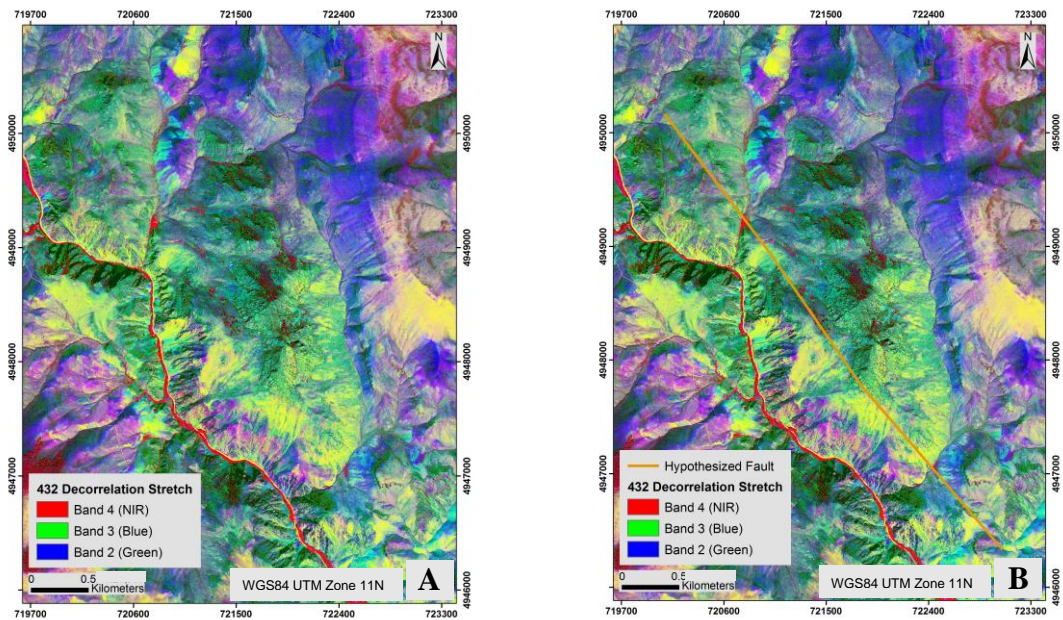


**Figure 35 (Previous Page):** NAIP decorrelation stretch image of the eastern study area, using band 4, band 3, and band 2, with a histogram equalize stretch applied. The color representation on these RGB composite images are the decorrelated band 4 in red, the decorrelated band 3 in green, and the decorrelated band 2 in blue. Maps A and B are identical, except map B is overlain by the hypothesized fault that was identified in the WorldView-2 data. Image Source: NAIP: U. S. Department of Agriculture, Farm Service Agency.

## Field Results

In spite of our identification of a promising locality, in the remote sensing data, near the bend in Spring Creek, field investigation was not able to confirm any evidence of significant, active faults within this area. Several volcanic units may have been offset by a fault, but there were no surficial features near the hypothesized fault trace that are consistent with the fault having recent activity.

## Discussion

### Remote Sensing

Considering all the remote sensing results, neither area is a likely candidate for the fault of interest. There is almost equal evidence of the presence of a fault in both areas, except the western study area has a prominent bend of the drainage while there is no observable drainage offset in the eastern study area. When the Spring Creek drainage (Figure 4a) was observed in the field, there was no evidence of a fault with young surface displacement. There is somewhat greater evidence of lineaments in the eastern study areas, but those lineations are more likely related to the topographic characteristics of the area than modern fault activity. The evidence observed for both areas is summarized in Table 10.

Pieces of evidence are observed in every remote sensing result for the east area except WorldView-2, OSAVI, and Sentinel-1, but clear evidence of lithologic offset is not observed in either area. There are some pieces of evidence observed in the west study

**Table 10:** A cumulative overview of the remote sensing results

<u>Evidence</u>	<u>West Study Area (Positive Results)</u>	<u>East Study Area (Positive Results)</u>
Lineaments	13	15
Offset Rock	Confirmed: 0 Possible: 2	Confirmed: 0 Possible: 4
Topographic Discontinuities	1	0
Depressions along Fault Trace	2	2
Scarps or Cliffs	0	0
Shifts in Drainage	14	0
Changes in Vegetation	2	5

area’s WorldView-2 New Iron Index, WorldView-2 Non-Homogenous Feature Index, but the results are ambiguous and, so they cannot be confidently used as evidence. There is also ambiguous evidence in the east area’s ASTER and Sentinel-2 classifications, but the results are subtle and may be remnants of erosion that give the appearance of offset.

There are vegetation anomalies at both the east and west study areas, but these patterns are much more defined in the east study area, which is supported by the results from the WorldView-2 Improved Vegetation Index, WorldView-2 OSAVI, NAIP NDVI, NAIP Decorrelation stretch, and the natural color NAIP images. In the western study area, the same processes were used to identify vegetation patterns, but no clear results were observed in the results from WorldView-2 OSAVI, the NAIP decorrelation stretch, or the NAIP natural color image. These vegetation indices are much clearer in the NAIP NDVI results than they are in the WorldView-2 New Vegetation Index, or the WorldView-2 OSAVI.

ASTER and Sentinel-2 have similar results, with some minor differences. The overall quality of their classifications is shown in Table 11. The accuracy differences between these sensors are likely the result of the differences in spectral responses

<b>Table 11:</b> Comparison of classification accuracies between ASTER and Sentinel-2 results.		
<u>Classification Method</u>	<u>ASTER</u>	<u>Sentinel-2</u>
SVM	94.83%	90.13%
MLA	96.22%	89.09%
MD	72.21%	71.36%

between the two sensors. Even though Sentinel-2 has better spatial resolution than ASTER, the spectral range and number of bands is smaller for Sentinel-2 and so it's hard to differentiate subtle spectral differences between lithologies. This is particularly the case, because the ASTER sensor has 6 SWIR bands, the parts of the spectrum that minerals have a greater diversity of responses to. The ASTER sensors advantage is supported by the accuracy represented in the confusion matrices, where it outperforms Sentinel-2 in each classification technique, shown in Table 11.

Despite any differences in results, the spectral patterns are more valuable than the actual classification. For these purposes, we applied some of the traditional geological assessment techniques to the spectral patterns, just like we would with a geological map. This includes forming hypotheses based on systematic truncations in the spectral patterns, lineaments in the spectral patterns, and topographic relationships to the spectral patterns. Even if a pixel is misclassified, the classifications are binned out using algorithms that assess the spectral values and so different results between the methods gives us more

information because that means there is a spectral difference that was observed at those locations.

The results from the WorldView-2 Improved Vegetation Index and the Non-Homogeneous Feature Index are unclear, because they appear to be affected by shadowing. Initially, there appeared to be some spectral patterns related to lithologic composition in the indices, but when were compared to the aspect and to Google Earth images, it was clear that these patterns corresponded to shadows. In the WorldView New Iron Index, the lighter pixels clearly correlate to shadows and the north-facing aspects of the hills. In the Non-Homogeneous Feature Index, dark pixels correlated to northern aspects, large shadows cast by topography, and even the smaller shadows cast by trees. Light pixels tended to correlate to washes and drainages areas where vegetation is very limited and intermediate pixel values correlate to areas with scrub or sparse vegetation. Each of these results could very well result from the extent of shadowing.

In the WorldView Improved Vegetation Index and OSAVI results, lineaments and changes in vegetation were observed in both study areas. The brightest pixels in these results correspond to trees, intermediate pixels relate to scrubby vegetation, and the darkest pixels correspond to shadows. In the east area, there is a linear vegetation anomaly that trends nearly parallel to the hypothesized fault and terminates as it intersects it. In the western area, linear vegetation patterns were present that trend parallel to the hypothesized fault, along its trace, but as with the other results, this was likely a result of topography. In the False Color Composite image produced from the WorldView-2 imagery, we also saw these patterns of vegetation in the east area, but they are probably a result of the presence of trees in the stable, unshaded topographic highs.

Topographic discontinuities were only observed in the western study area, but this may be because the topography has greater relief, but still, no scarps or cliffs were observed in either study area. The topographic evidence of faulting (topographic discontinuities, linear depressions, and shifts in drainage course) may be present in the western study area, but this likely because any topographic effects and erosional characteristics are enhanced by the topographic relief and greater number of drainages in the west. There is topographic evidence (i.e. a linear depression) in the east as well, but using these techniques, I was unable to determine if these are evidence of a fault or if they are simply a product of topography or erosion related to a lithologic contact. Both areas have drainages that cross the hypothesized fault, but it is only in the west where we observe a drainage with a significant bend that corresponds to the hypothesized fault location, but when this area was investigated in the field, we were unable to identify any evidence of a significant fault that might result in a such a dramatic drainage shift.

Unfortunately, no reliable results were produced from the Sentinel-1 data. There are high brightness values in the Sentinel-1 data, along much of the Lost River fault system, and even though high brightness values may indicate the presence of a fault, these results are considered inconclusive because there is also a correspondence between high brightness values and some drainage channels and rockslide and talus accumulations. Additionally, it is possible that these may be false positive results due to the multiple collection angles used to acquire the data (i.e. horizontal and vertical collection). Generally, Sentinel-1 has been used to produce interferograms after large magnitude earthquake events. Sentinel-1 does not have the temporal resolution required

for identifying small magnitude fault activity to form any real conclusions based on these results.

### Study Limitations

The volcanic rocks of the Challis Volcanic Group impose difficulties for remote sensing studies. The spectral qualities of its different components tend to fall into one of two groups, Felsic-Intermediate and Intermediate-Mafic. Beyond those two groups, there is no distinct difference that I have been able to interpret in any of the imagery. Beyond the spectral similarities of its different units, the Challis Volcanic Group in this area includes extruded rock types, such as rhyolite and dacite, as well as explosive components (i.e. ash). This means that the rocks are not necessarily stratified and so things like apparent offset or lineations of these rocks, which make up a significant portion of our area of interest, cannot immediately be determined with remote sensing as representative of a fault, and so additional observations must be made on the ground to confirm their legitimacy. This is problematic, considering that the Challis Volcanic Group rocks are the dominant lithologies in the area where this fault would most likely be located. The only significant presence of other lithologies being in the east and west study areas that were discussed in this research and the entire area is much too large to ground truth within the timespan that we have available to perform this research.

A major concern that arises from the spectral similarities within the Challis Volcanic Group's felsic units that dominate the entirety of the region between the two study areas. If we predict that the location of the fault based on the mean earthquake depth, then the fault would likely be somewhere between these two areas of interest, several kilometers from where lithologic differences were observed with the techniques

we had available. Despite this issue, the east and west study areas were the best targets for this study, because there is spectral variation to observe. Both areas are still within the reasonable range where we might expect to find the fault, and so they remain candidate locations of the fault.

It is possible that additional ROI classes might improve the results, but the fact is that there is not an available geological map at a reasonable scale in either area of interest and so designating ROIs with a greater diversity is not a reasonable task. Additionally, the application of spectral scanners to identify the detailed spectral reflectance curves for the area could be applied to further hone the differences, but that is a very time consuming and detailed task, especially considering the logistics of transporting the equipment necessary into such a difficult area to access. Even if these ROI or spectral reflectance curves could be produced, delineating features with remote sensing is essentially a task of identifying significant compositional differences, such as high versus low silica content. It is unlikely that the available remote sensing platforms' spectral resolution that is available for sensing short wave infrared wavelengths could realistically delineate the subtle differences in composition that would be present in the felsic rocks. This is supported by observing the spectral responses from the ASTER PCA. The ASTER sensor has the greatest diversity of short wave infrared response and there did not appear to be a practical amount of pixel variance in the results, which would be required to perform a successful delineation of lithologies.

Some of the spectral patterns that were observed are unreliable, because aspect may influence some the results, especially for the imagers derived from the WorldView-2 and NAIP sensors. Because of the sun's position in the south, the northern aspects are

shadowed. These shadows reduce the reflectance that is recorded by the sensor and affect vegetation patterns. Those shadows are translated over into the results from the indices and false color composites from these sensors. This influence is especially present in the western study area, where there is greater topographic relief with more prominent east-west trending ridges and thus more extensive shadowing. This does not appear to be an influential factor in classification results for Sentinel-2 or ASTER data. This is probably because the ROIs reference multiple aspects.

The goal for Sentinel-1 processing was to be able to identify changes in elevation that have occurred due to ground movement along a possible fault. The problem that we encountered is that the Sentinel-1 satellite has only been in orbit since 2014 and it does not appear that enough change has accumulated in the northern portions of the Lost River fault within that time frame. Interferograms were generated with the greatest gap in time that was available, but even the areas along the known northern segments of the Lost River fault system did not show any detectable change on interferograms or change detection modules. The only identifiable change that was observed is interpreted as landslides. Perhaps, if this is a case of fault creep, in several years, once the gap in data collection is larger, these changes along the fault system will be observable. At this point, it does not appear to be possible to detect.

### Geological Explanations

The lack of a prominent surface expression of an active fault associated with recent seismicity north of Challis may be explained by the presence of a blind fault. Thus, a surface expression of the fault may not have yet formed. In the southern portion of the Lost River fault system, the fault is almost exclusively observed as a geographically

localized, linear fault trace that follows the range-front. However, as the fault trace continues north, the trace is observed as several sub-parallel strands across the Lost River Valley, consisting of at least two southwest-dipping segments of the Lost River fault system (Warm Spring and Challis segments) as well as the separate, northeast-dipping Lone Pine fault that forms the southwestern margin of the valley. If slip along the Lost River fault system and related faults in this northern locality is shared among several synthetic and antithetic fault strands, then it is reasonable that there could be less slip along the northern segments of the fault. This could, in turn, help explain a relatively minor surface expression of faulting north of Challis. Further remote sensing investigation of a previously undocumented fault northeast of the Challis segment of the Lost River fault system was investigated to evaluate the viability of the alternative hypothesis for the northern expression of Basin and Range faulting in the area. These results are described below.

#### Recommendations for Future Research

In the future, more work is required to resolve the significance of this linear cluster of seismicity and the structures with which it is associated. We believe that the Sentinel-1 data could be a key indicator for the location of the fault, if it has reached the surface. In several years, or after a larger seismic event has occurred in our area of interest, if the interferograms are produced it is possible that it might result in the detection of a fault that is related to the seismicity.

Another recommendation is that researchers may conduct transects across the region of interest using unmanned aircraft vehicles or boots on the ground observations. If the fault does have a surface expression, it is possible that it could be detected by

collecting and analyzing high-resolution data or visual transects of the region between the two study areas. If the same transects were conducted at multiple time intervals, especially those conducted with unmanned aircraft vehicles, they could be compared to observe subtle topographical changes. Additionally, as unmanned aircraft vehicle technology advances, flying the entire area between those two study areas may become a reasonable endeavor.

## Chapter 4: Geologic Scouting Using Unmanned Aircraft Systems

### Introduction

Because of the lack of success in identifying an active fault in the northern study area, we expanded our remote sensing study to a previously undocumented fault northeast of the Challis segment of the Lost River fault system (Figure 36), using an unmanned aircraft system (UAS). Within this southern study area, we sought to explore the alternative hypothesis that within the northern Lost River fault system, the main fault splays into several fault strands that share lower slip magnitudes. For this southern study area, we used a Parrot Disco delta wing UAS, which is a low-cost option for scouting for areas that can later be targeted either on foot or with more sophisticated sensors.

We collected data over the suspected surface expression of a fault, northeast of the Challis segment of the Lost River fault system. This fault system has had significant fault activity in modern history, and so it is important that the geologic hazards associated with it are understood. In 1983, a Mw 6.9 earthquake occurred along the Lost River fault system's Thousand Springs segment, near Borah Peak. In this scouting mission, we collected data east of Challis, over a suspected surface expression of the fault system, approximately 25 km north of the epicenter of the Borah Peak event (Figure 36). The eastern strand of the Challis segment of the Lost River fault appears to continue beyond the mapped terminus, continuing north of the city of Challis.

The goal of this study was to assess the functionality of using this low cost UAS platform as a tool for geological remote sensing and to evaluate the character of the Lost River fault system near its northern mapped terminus. It is often the case that faults occur over large lengths of land, which may include challenging terrain that makes it a time-

consuming endeavor to access the entire area. Having a tool such as the Parrot Disco to identify areas where a fault expresses itself on the surface can save researchers time and resources in their investigations.

In concert with traditional field mapping, the implementation of UAS surveys for geologic scouting has the potential to revolutionize geologic mapping. The ability to efficiently cover large areas of land is especially helpful for research in areas like east-central Idaho, where the ground is typically overlain by snow from October through May, or even longer. Another advantage of using UAS research is that the aircraft view provides a perspective that allows for features to be delineated, which may not be apparent otherwise. By performing this this scouting mission and processing the data collected, we can assess the functionality of this system as a tool for geologic scouting as well as to collect data over the suspected surface trace of the fault so that we can identify locations that can be targeted with higher quality sensors so that the structure can be precisely characterized.

UAS-based remote sensing produces data from a perspective that cannot be achieved from land based observations (Matthews, 2008). The process used to stitch UAS data into continuous datasets and create 3D models, Digital Surface Models (DSMs), and orthophotos is called structure from motion (SfM) and has been increasingly used by geologists for computer-based mapping (Westoby et al., 2012; Pavlis and Mason, 2017). The general workflow for UAS data processing produces georeferenced DSM and orthorectified imagery as a tool for observation and spatial analysis (Westoby et al., 2012; Bemis et al., 2014). Additionally, the workflow used to create DSMs and

orthoimagery from UAS data can also produce a 3D model, creating a revolutionary way of visualizing landscapes and performing 3D mapping (Pavlis and Mason, 2017).

In order to produce these models, each location in the study area must have an overlap of three images (Westoby et al., 2012). Often issues in the imagery make photos unusable, such as over exposure or blurriness. To ensure the completeness of the model, it is often considered best practice to collect as many images as is feasibly possible for each location, so that unusable photos will not produce holes in the resultant model (Westoby et al., 2012). Hackney and Clayton (2015) describe how the quality of the output products is largely a result of the quality of the GCP; stating that GCP should be distributed throughout the model, especially around the areas of interest, in order to reduce errors related to lens warping and registration errors. Pavlis and Mason (2017) applied these techniques to mapping of geologic structures based on UAS data that was processed to create a 3D model. They described a range of applications that lightweight, low-cost UAS platforms may have for the future of geology, beyond geologic mapping, such as: planning safe routes in the field, hazard detection, and to effectively act as a “field assistant” for geological scouting.

UAS data is collected using fixed wing or rotor platforms. Fixed wing platforms, such as the delta wing Parrot Disco platform that was used in this workflow, collect data over large areas more efficiently than rotor platforms because they glide at higher altitudes, with greater power efficiency but the height at which they typically fly results in data with comparably lower spatial resolution than their rotor counterparts (Remondino et al., 2011; Siebert and Teizer, 2014; Hackney and Clayton, 2015). Rotor platforms have shorter flight durations but have better maneuverability than fixed wing

platforms and can operate at lower altitudes, collecting imagery with higher spatial resolution (Remondino et al., 2011; Siebert and Teizer, 2014). This makes fixed-wing platforms more realistic for scouting large areas that can later be targeted for higher resolution data collection with a rotor platform.

## Methods

The Parrot Disco delta wing UAS is an inexpensive and simple platform, requiring minimal skill to operate. Unlike some platforms that require a pilot with a lot of experience to safely fly, the Parrot Disco can be flown using automated flight plans and can even land itself. Currently, Parrot sells its Disco for less than \$1,000 and includes everything except for the cellphone or tablet that is required to view flight data, create automated flight missions, and keep firmware up to date. The affordability and user-friendly nature of this UAS means that any work done with it can be easily replicated.

The area of interest for this study (Figure 36) is characterized by relatively gentle topography near the proposed terminus of the eastern strand of the Challis segment of the Lost River fault system. It is a vegetated high desert area, covered in sagebrush and grasses. Data was collected along the suspected fault trace, at approximately 50 m above ground level (AGL). The automated flight plan for the Parrot Disco was created using Parrot's FreeFlight Pro app. The Parrot Disco platform does not follow terrain, and so after deciding what height we wanted to fly for data collection, we compared our flight path to topographical maps to ensure that flight altitudes for each waypoint ensured that safe flying heights were maintained (e.g. if the UAS is launched from the ground and instructed to fly at a height of 50 meters, if it flew over a 50 m tall hill, the flight height as it passed over the hill would be 100 meters, to maintain the goal of flying 50 meters AGL). Additionally, the flight plan was paused while the drone was in flight when it

reached areas of interest and the drone was put into loiter mode, so that it circled over areas interest to ensure that these areas had enough overlap to construct a complete model. Compared to prior flights that did not involve “loitering” along the flight path, this method was critical for generating sufficient overlap of images.

The camera is nose-mounted, and the camera angle can be adjusted from 0° (horizontal, toward the skyline) to 83° (pointed toward the ground). In the camera settings for the mission, data collection type was set to video for each waypoint, and the maximum camera angle (83°) was used. The frames from the video were extracted and used as images and processed using structure from motion. The reasoning for using video data collection rather than image data collection, even though we are extracting images from the video, is the data collection rate. For image data collection, this UAS platform is only capable of collecting one 1 image every 8 seconds, which results in data that does not meet the overlap requirements for processing the data using structure from motion.

For this workflow, we conducted 2 flights that recorded video data. The videos were brought into Adobe Premiere where the landing and launch portions of the flights were cropped out and the two flights were consolidated into one video file and exported to an h.264 .mp4 format. The h.264 video file was brought into Pix4D, where we extracted 1 frame for each second in the video, which resulted in 2,512 total images. The initial data processing and quality report were processed in Pix4D, along with the point cloud densification.

At this point in the processing, the data did not have any spatial reference, and so ground control points were introduced into the model. The model was compared to NAIP imagery and locations were chosen that could be clearly seen both in the NAIP imagery

and in the model. These locations were digitized as points in ArcMap and the “Add XY data” tool was used to extract their northing and easting values. To get the elevation data, the National Elevation Dataset (NED) was brought into ArcMap, and the “Extract Raster Value to Points” tool was applied to the points, adding the corresponding NED values to the attribute table field.

Using the Ground Control tool in Pix4D, 3D ground control points (GCP) for each of the 8 locations was placed in the correct position in the corresponding images from the UAS data collection, and the northing, easting, and elevation values were included for each GCP. The model was reoptimized, the initial processing, quality report, and point cloud densification were rerun and the digital surface model (DSM) and orthophoto were produced. Finally, using ArcMap, the data at the edges of the model that was relatively poor quality (i.e. blurred or distorted) was masked out of the final DSM and orthophoto.

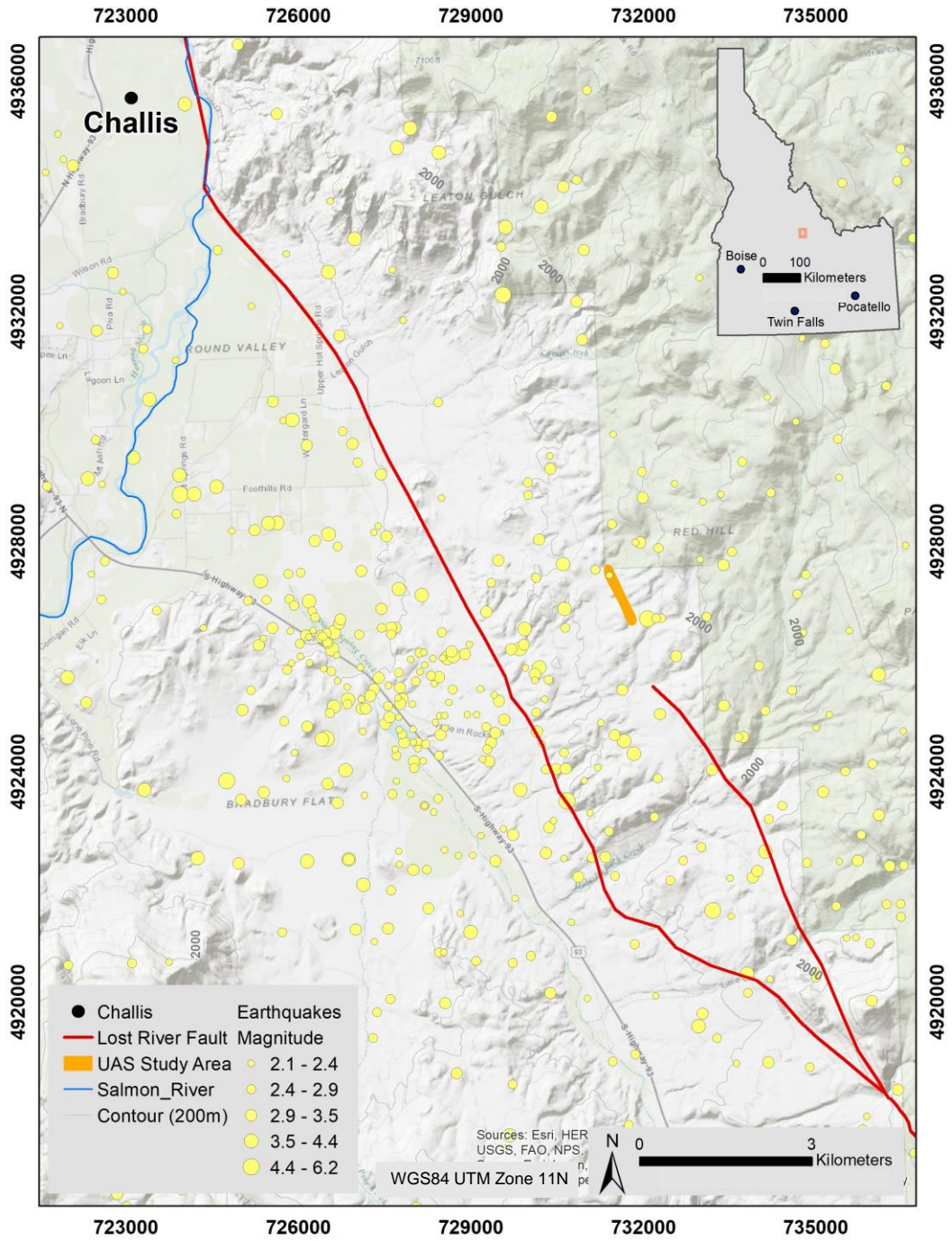


**Figure 36:** Map showing the study area for UAS data collection in relation to the Lost River fault system

## Results

An orthophoto (Figure 37) and DSM (Figure 38) were produced from the UAS data collection. A quality report was generated during the initial processing, which communicated that the final data product has an area of 0.67 km<sup>2</sup> and a 7.41 cm ground sampling distance (GSD) and that 2,144 of the 2,512 extracted image frames were included in the model. Out of the 8 GCP, 6 of those had sufficient overlap to be included in the model, resulting in an RMS error, of 0.22 m, based on those 6 points.



**Figure 37:** The orthophoto produced using Pix4Dmapper 4.0, from the UAS data collection. The arrows point to locations where linear vegetation patterns were observed.

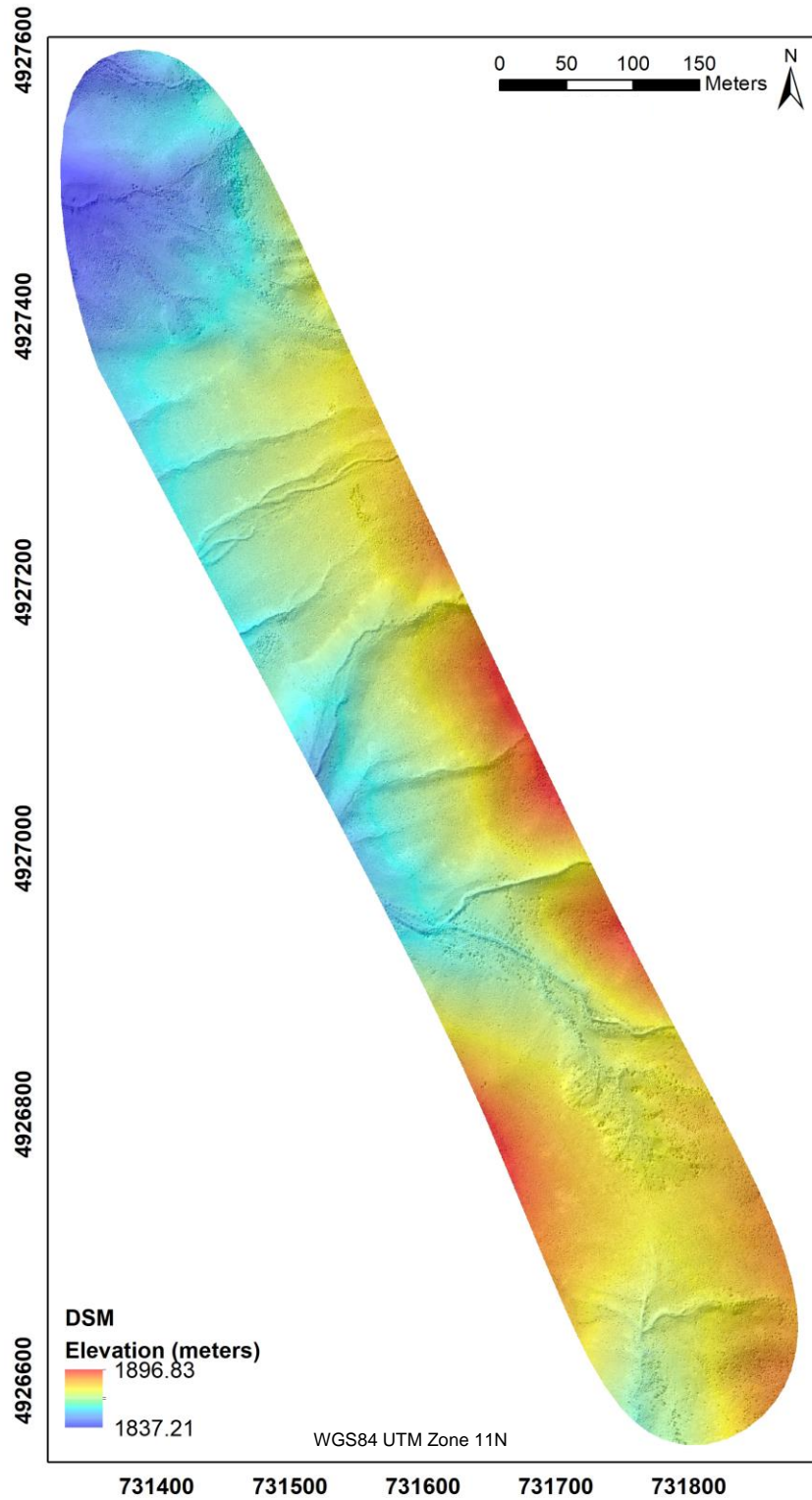


**Figure 38:** The DSM produced using Pix4Dmapper 4.0, from the UAS data collection.

## Discussion

Based on the orthoimage (Figure 39) and DSM (Figure 40) from this scouting mission, there appears to be an unidentified trace of the Lost River fault system that was identified in the study area. The suspected fault was identified on the basis of changes in slope that are observed in the DSM and in the vegetation patterns. This feature does not form a prominent scarp in surficial deposits, suggesting that it is likely not the locus of a highly active fault. However, the result is consistent with the hypothesis that along the northern extent of the Lost River fault system, several faults share the overall slip, and each fault has a lower magnitude of slip. This may explain the lack of a prominent surface expression of faulting north of Challis.

If more time were available to conduct fieldwork in the southern study area, it would have been advantageous to collect additional data at a lower altitude over the areas along the trace that were approximately located. By doing this, we could have supplemented our results with a higher resolution dataset, so that more locations along the trace may have been well located. The biggest challenge to this investigation was the low accuracy of our GCP. The elevations included in the GCP are based on the NED dataset, which has a resolution of 10 m, resulting in several meters of error in the vertical component of the model. The northing and easting values for our GCP were based values extracted from the NAIP dataset, with a resolution of 1 m, resulting in 0.22 m of error. Because of this and minimal interaction between the well located portions of the fault and the topography, our location errors were too high to confidently calculate the strike and dip of the fault. If more time were available for additional trips to the field, it would have been valuable to conduct an additional flight, after initial results were processed. This would have allowed us to place markers in the field around where the fault is well

located, with precise GPS locations. This would have greatly reduced location errors in the dataset, allowing us to precisely identify the strike and dip of the fault plane. Figure 41 shows the hypothesized fault trace overlain onto 10 m topographic contours, based on the national elevation dataset, supporting that there is not enough information present to confidently construct structure contours for the fault.

Qualitative comparisons between the trend of the hypothesized fault trace and the Central strand of the Challis segment of the Lost River fault system support that this trace represents a previously unrecognized continuation of the Central strand of the Challis segment, as opposed to it being a separate strand of the fault system. The method presented here provides evidence that data collected with UAS platforms and processed using SfM techniques is an effective tool for identifying geologic structures. This supports the claim of Pavlis and Mason (2017) that lightweight UAS platforms are an effective tool for geologic scouting. This type of surveying may prove to be useful for geology because of its efficiency, cost effectiveness, and simple workflow

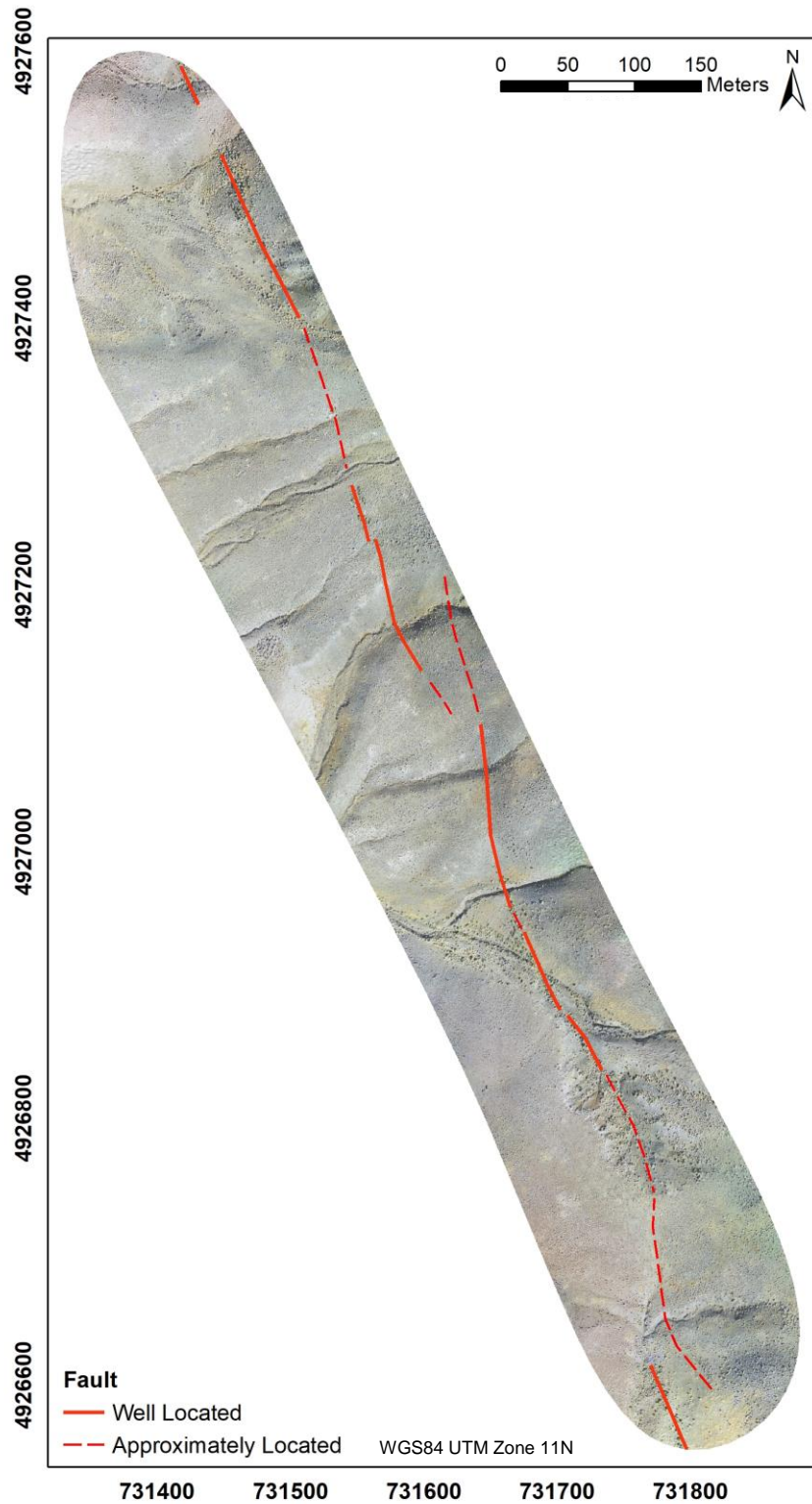


**Figure 39:** The hypothesized fault trace, overlain with the orthophoto result.

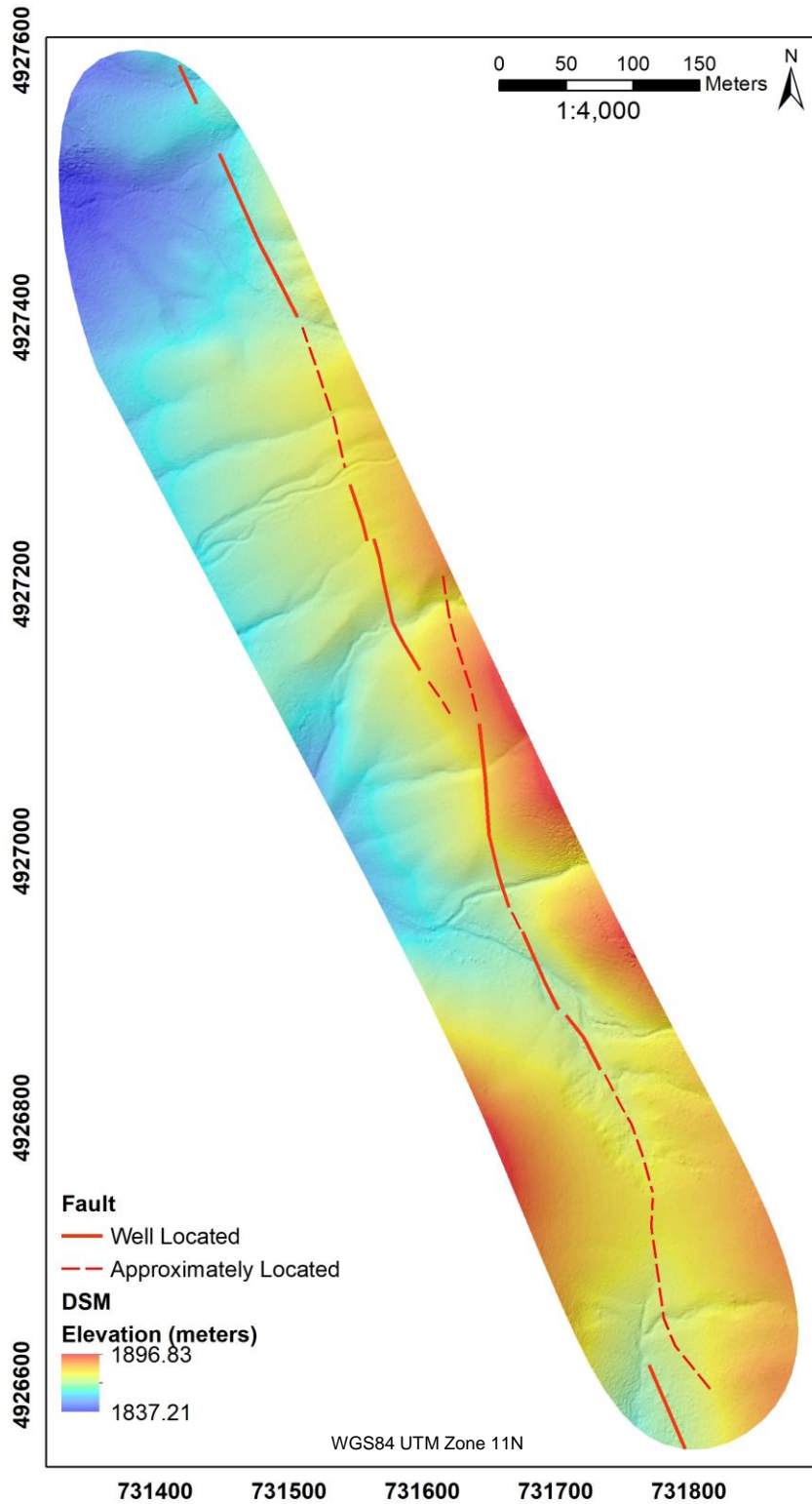


**Figure 40:** The hypothesized fault trace, overlain with the DSM result.

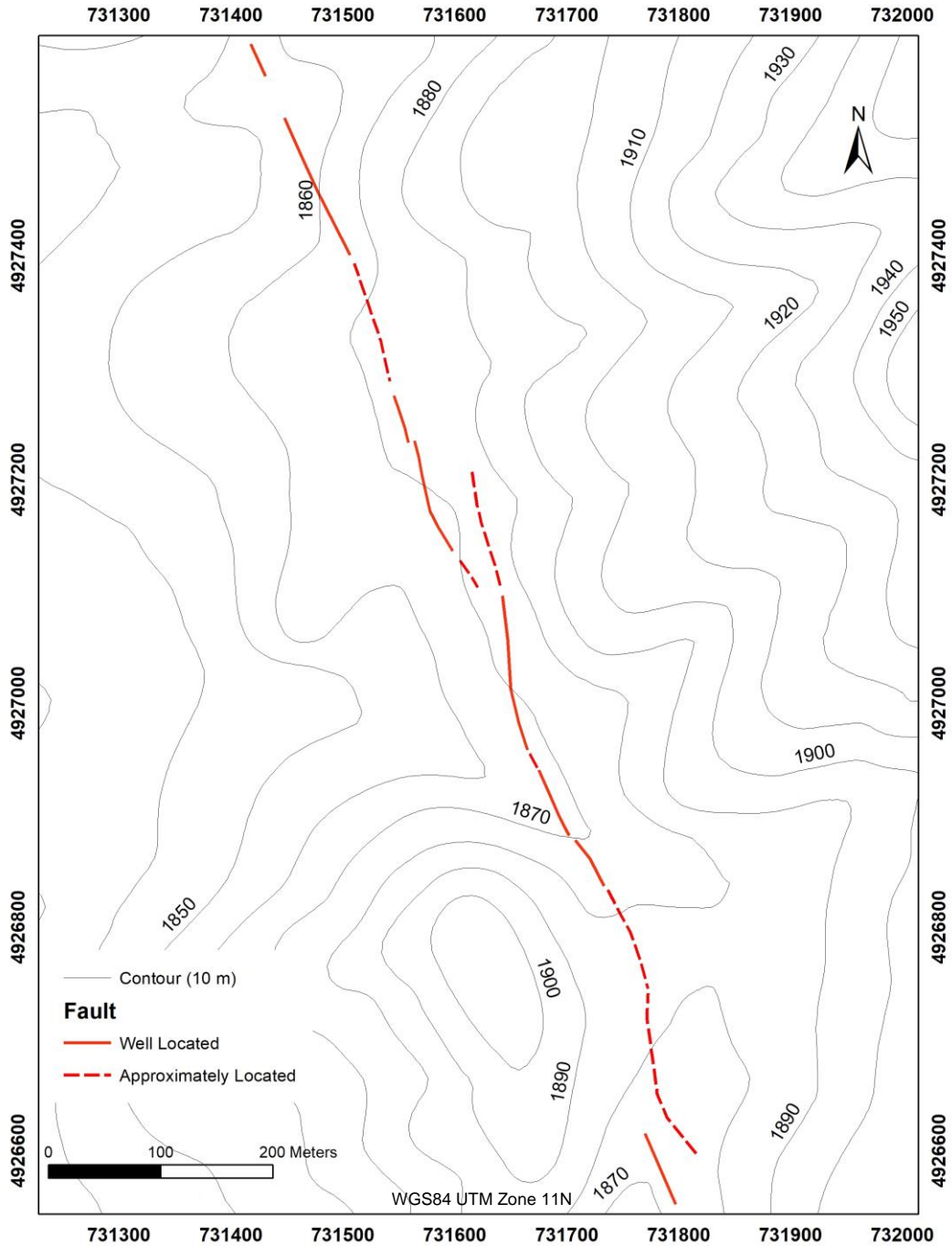


**Figure 41:** The hypothesized fault trace overlain with 10 m topographic contours, based on the National Elevation Dataset (NED).

## Chapter 5: Recommendations for Future Work

The seismicity north of Challis, Idaho, in 2014-2016 was not of a sufficient magnitude to produce a surface rupture. The linear dispersion supported the hypothesis that historically larger magnitude events might have occurred along an unidentified fault which might have produced a surface expression. Though an active fault was not located in the northern study area that could be related to the seismicity, this research demonstrates a successful method for delineating geologic structures using satellite data. Multiple parallel faults are present near the northern terminus of the Lost River fault system which is likely the result of a horsetail fault structure. Surface expressions of these faults diminish toward their northern termini and so the seismicity is likely either occurring on a blind fault or a fault with a minimal surface expression. Further evidence of these patterns was observed in the southern study area, where a low-cost method of geologic scouting was implemented using an unmanned aerial system (UAS). In this research, a previously unidentified trace of the Lost River fault system was observed. This fault is only well located along approximately 50% of its trace and is located ~1 km north of the closest mapped strand of the fault, providing further evidence for the presence of a horsetail structure and for the pattern of decreased surface expressions as the Lost River fault system approaches its northern terminus.

There are several ways that the results may have been improved, such as using a less generalized set of regions of interest (ROI), to have had more time in the field to collect data, and implementing a tool to detect lineaments. Additionally, if we had more time available, it would have been useful to collect UAS transects so that we could observe

high-resolution elevation and spectral data, by producing data products similar to those described in Chapter 4.

The Challis Volcanic Group, which dominates the northern study area, is notoriously difficult to work in because the units look very similar to each other, despite having a range of chemical compositions. The low abundance of phenocrysts make it difficult to infer the chemical compositions of the units. This makes it unrealistic to identify the appropriate analogous examples from other regions for comparison to the units that were observed in the field, since we lacked necessary information related to their compositions (e.g. mineral assemblages or alkali-lime indices). Without having appropriate analogs for comparison, adapting spectral information from the ASTER spectral library is not appropriate for delineating individual units. Another challenge is that the tuffaceous units of the group have been reworked by surficial processes and so their composition is not necessarily uniform throughout their exposures. Using spectral scans of rock samples from the area, which produces highly detailed spectral curves that vary based on the chemical composition, could have facilitated the observation of each unit's spectral characteristics, allowing us to produce a spectral library for the unit of the Challis Volcanic Group that are represented in the northern study area.

The spectral ranges and spatial resolution for short wave infrared (SWIR) and thermal infrared (TIR) bands for the sensors available were not ideal for observing subtle surface expressions of faults. The best sensor that was available to us with responses in these ranges is the ASTER data, which has six SWIR bands, with a spatial resolution of 30 m, and five TIR bands, with a spatial resolution of 90 m. Perhaps if a hyperspectral sensor was available with a greater number of SWIR and TIR bands, even with similar spatial

resolution, we would have been able to improve our results. Higher resolution data would have also given us an advantage. Even the national agricultural imagery program (NAIP) data, which only collects data in the very near infrared (VNIR) range, produced highly detailed results that were just as informative for our purposes as the platforms with more appropriate spectral ranges. As unmanned aerial systems (UAS) become more efficient, high resolution multispectral data may be collected along the entire northern study area. Modern SWIR sensors are too heavy to be flown on UAS platforms. Once the weight-carrying capacity and weight of SWIR sensors converge, UAS-based lithological studies will become a more practical and advantageous endeavor.

The classification results might have been improved by developing more diversity in the regions of interest. In order to simplify the lithologic diversity that was present on the geologic map, regions of interest were grouped into the following compositions: (1) mafic to intermediate, (2) felsic to intermediate, (3) metamorphosed sedimentary, (4) sedimentary, and (5) alluvium. In hindsight, it may have been advantageous to develop multiple classes to represent the metamorphosed sedimentary and sedimentary compositions. The sedimentary rocks will have spectral compositions that respond to their constituent minerals. Based on the descriptions of lithologic units from the geological map (McIntyre and Hobbs, 1987), ROI diversity may have been better represented if those two classes had instead been developed into the following eight classes: (1) quartzite, (2) feldspathic quartzite, (3) quartzite with phyllite, (4) pebbly quartzite, (5) calcic sedimentary, (6) siliceous sedimentary, (7) mudstone, and (8) argillite. Often several compositions are present within a particular lithologic unit and so

field observations and corresponding GPS locations would be needed to identify locations to include.

The PCI Geomatica software includes their “Line” tool, which is used for lineament extraction. This tool was designed for radar data, but can also be applied to spectral data to automatically detect lineament features, based on the pixel patterns. We have just become aware of this unit very recently and if more time was available to conduct this component, it could have been applied to the Sentinel-1, Advanced Spaceborne Thermal Emission and Reflection Radiometer (ASTER), and Sentinel-2 data. Landsat 8 was not implemented in the workflow thus far, but we would have also liked to incorporate it into this work for lineament extraction.

In the southern study area, we used a low cost UAS for initial scouting to rapidly detect surface expressions of potential faults. This was successful because we were able to collect data at such a high resolution that our results allowed us to confidently identify the surface expression of a previously unrecognized fault. The goal of this research was to efficiently scout the area. Because of the time constraints involved in this method, highly accurate ground control points were not established in the field. This resulted in an error of 5-10 m for the elevation and 0.22 m of error for the latitude and longitude. The well located portions of the fault had limited interaction with the topography and so 5-10 meters of error may contribute a significant amount of error to strike and dip calculations. If more time were available in the field, it would have been advantageous to have included precisely located GCP around the area where the fault is well location. To improve upon this scouting approach a more expensive UAS with RTK would provide

higher accuracy and combined with ground control it would allow for calculating strike and dip of the fault plane.

## Chapter 6: Conclusions

The linear trend of seismicity north of Challis, Idaho, supports the hypothesis that prehistorically larger magnitude events might have occurred along an unidentified fault with the capacity to produce a surface expression. However, the seismicity in 2014-2016 was not of a sufficient magnitude to produce a surface rupture. Though a fault that could be responsible for the recent seismicity was not located in the northern study area, this research demonstrates a method for investigating geologic structures using satellite data.

This northern portion of the Lost River fault system is likely representative of a horsetail fault. Near the southern terminus of the Lone Pine fault, the system begins to splay and several parallel strands of the Challis Segment of the fault system are observed, as well as the Willow Creek Hills strand of the Lost River fault system and the Lone Pine fault. These components of the fault system become less topographically pronounced as they near their northern termini. If multiple faults are accommodating slip and their surface expressions become less pronounced toward their northern termini, seismicity may be occurring along a blind fault, rather than being due to the limitations of the study. Alternatively, in the northern study area, if the fault tip has reached the surface, there may not have been enough displacement accumulated along the fault to form a recognizable surface expression.

Further evidence of a northward decrease in displacement was observed in the southern study area, where a low-cost method of geologic scouting was implemented

using an unmanned aerial system (UAS). In this research, a previously unidentified component of the central Challis strand of the Lost River fault system was observed. Though the United States Geological Survey has accepted an ~8.2 km surface trace ~1 km to the south of our southern study area. No surface expression of a fault has been located between the central Challis segment and our study area. The surface expression of the fault we have identified is only well located along approximately 50% of its trace. This supports our hypothesis that there is a trend of diminished surface expression as the faults in this system approach their northern termini. Additionally, along the surface expression that we have identified, the trace may include multiple sections, rather than a single linear feature, but this cannot be determined without more accurate topographical data.

## References

- Anders, M.H., and Schlische, R.W., 1994, Overlapping faults, intrabasin highs, and the growth of normal faults: *The Journal of Geology*, p. 165–179.
- Bales, R.C., Hopmans, J.W., O’Geen, A.T., Meadows, M., Hartsough, P.C., Kirchner, P., Hunsaker, C.T., and Beaudette, D., 2011, Soil moisture response to snowmelt and rainfall in a Sierra Nevada mixed-conifer forest: *Vadose Zone Journal*, v. 10, p. 786–799.
- Bemis, S.P., Micklethwaite, S., Turner, D., James, M.R., Akciz, S., Thiele, S.T., and Bangash, H.A., 2014, Ground-based and UAV-based photogrammetry: A multi-scale, high-resolution mapping tool for structural geology and paleoseismology: *Journal of Structural Geology*, v. 69, p. 163–178.
- Bennett, E.H., 1986, Relationship of the trans-Challis fault system in central Idaho to Eocene and Basin and Range extensions: *Geology*, v. 14, p. 481–484.
- Bennett, R.A., Wernicke, B.P., Niemi, N.A., Friedrich, A.M., and Davis, J.L., 2003, Contemporary strain rates in the northern Basin and Range province from GPS data: *Tectonics*, v. 22.
- Bishop, B.D., Dietterick, B.C., White, R.A., and Mastin, T.B., 2014, Classification of plot-level fire-caused tree mortality in a redwood forest using digital orthophotography and LiDAR: *Remote Sensing*, v. 6, p. 1954–1972.
- Chen, P., Liew, S.C., Lim, R., and Kwoh, L.K., 2011, Mapping coastal ecosystems of an offshore landfill island using WorldView-2 high resolution satellite imagery, *in* Proceedings of the 34th International Symposium on Remote Sensing of Environment, Sydney, Australia, v. 1015, p. 1015.

- Chen, N., Ni, N., Kapp, P., Chen, J., Xiao, A., and Li, H., 2015, Structural Analysis of the Hero Range in the Qaidam Basin, Northwestern China, Using Integrated UAV, Terrestrial LiDAR, Landsat 8, and 3-D Seismic Data: *IEEE Journal of Selected Topics in Applied Earth Observations and Remote Sensing*, v. 8, p. 4581–4591.
- Colgan, J.P., 2013, Reappraisal of the relationship between the northern Nevada rift and Miocene extension in the northern Basin and Range Province: *Geology*, v. 41, p. 211–214.
- Crone, A.J., and Haller, K.M., 1991, Segmentation and the coseismic behavior of Basin and Range normal faults: examples from east-central Idaho and southwestern Montana, USA: *Journal of Structural Geology*, v. 13, p. 151–164.
- Crone, A.J., Machette, M.N., Bonilla, M.G., Lienkaemper, J.J., Pierce, K.L., Scott, W.E., and Bucknam, R.C., 1987, Surface faulting accompanying the Borah Peak earthquake and segmentation of the Lost River fault, central Idaho: *Bulletin of the Seismological Society of America*, v. 77, p. 739–770.
- Dadon, A., Peeters, A., Ben-Dor, E., and Karnieli, A., 2011, A Semi-automated GIS Model for Extracting Geological Structural Information from a Spaceborne Thematic Image: *GIScience & Remote Sensing*, v. 48, p. 264–279.
- Dickinson, W.R., 2006, Geotectonic evolution of the Great Basin: *Geosphere*, v. 2, p. 353–368.
- Digital Globe, 2016, WorldView-2 Satellite Sensor:  
<https://www.digitalglobe.com/about/our-constellation>.
- Dinger, J.S., Zourarakis, D.P., and Currens, J.C., 2007, Spectral enhancement and automated extraction of potential sinkhole features from NAIP imagery - initial

- investigations: *Journal of Environmental Informatics*, v. 10, p. 22–29.
- Exelis Visual Information Solutions Inc., 2017a, Broadband Greenness:  
<https://www.harrisgeospatial.com/docs/BroadbandGreenness.html>.
- Exelis Visual Information Solutions Inc., 2017b, Geology Indices Background:  
<https://www.harrisgeospatial.com/docs/BackgroundGeologyIndices.html>.
- Exelis Visual Information Solutions Inc., 2017c, Miscellaneous Indices Background:  
<https://www.harrisgeospatial.com/docs/BackgroundOtherIndices.html>.
- Falkowski, M.J., Evans, J.S., Naugle, D.E., Hagen, C.A., Carleton, S.A., Maestas, J.D., Khalyani, A.H., Poznanovic, A.J., and Lawrence, A.J., 2017, Mapping tree canopy cover in support of proactive prairie grouse conservation in western North America: *Rangeland Ecology & Management*, v. 70, p. 15–24.
- Fonstad, M.A., Dietrich, J.T., Courville, B.C., Jensen, J.L., and Carbonneau, P.E., 2013, Topographic structure from motion: a new development in photogrammetric measurement: *Earth Surface Processes and Landforms*, v. 38, p. 421–430.
- Gabr, S., Ghulam, A., and Kusky, T., 2010, Detecting areas of high-potential gold mineralization using ASTER data: *Ore Geology Reviews*, v. 38, p. 59–69, doi: 10.1016/j.oregeorev.2010.05.007.
- Gad, S., and Kusky, T., 2007, ASTER spectral ratioing for lithological mapping in the Arabian–Nubian shield, the Neoproterozoic Wadi Kid area, Sinai, Egypt: *Gondwana Research*, v. 11, p. 326–335, doi: 10.1016/j.gr.2006.02.010.
- Gawthorpe, R.L., and Leeder, M.R., 2000, Tectono-sedimentary evolution of active extensional basins: *Basin Research*, v. 12, p. 195–218.
- Gesch, D., Oimoen, M., Greenlee, S., Nelson, C., Steuck, M., and Tyler, D., 2002, The

- national elevation dataset: Photogrammetric engineering and remote sensing, v. 68, p. 5–32.
- Gomez, C., Delacourt, C., Allemand, P., Ledru, P., and Wackerle, R., 2005, Using ASTER remote sensing data set for geological mapping, in *Namibia: Physics and Chemistry of the Earth, Parts A/B/C*, v. 30, p. 97–108.
- Grebby, S.R., 2011, Novel applications of airborne LiDAR and multispectral data for high-resolution geological mapping of vegetated ophiolitic rocks and sedimentary cover, Troodos Range, Cyprus: Diss., University of Leicester, 2011.
- Grebby, S., Naden, J., Cunningham, D., and Tansey, K., 2011, Integrating airborne multispectral imagery and airborne LiDAR data for enhanced lithological mapping in vegetated terrain: *Remote Sensing of Environment*, v. 115, p. 214–226.
- Guerrieri, L., Baer, G., Hamiel, Y., Amit, R., Blumetti, A.M., Comerci, V., Di Manna, P., Michetti, A.M., Salamon, A., and Mushkin, A., 2010, InSAR data as a field guide for mapping minor earthquake surface ruptures: ground displacements along the Paganica Fault during the 6 April 2009 L’Aquila earthquake: *Journal of Geophysical Research: Solid Earth*, v. 115.
- Hackney, C., and Clayton, A., 2015, 2.1. 7. Unmanned Aerial Vehicles (UAVs) and their application in geomorphic mapping.
- Hamza, B.A., He, Y., Krim, H., and Willsky, A., 2005, A multiscale approach to pixel-level image fusion: *Integrated Computer-Aided Engineering*, v. 12, p. 135–146.
- Jawak, S.D., Luis, A.J., Panditrao, S.N., Khopkar, P.S., and Jadhav, P.S., 2013, Advancement in landcover classification using very high resolution remotely sensed 8-band WorldView-2 satellite data: *International Journal of Earth Sciences and*

- Engineering, v. 6, p. 1742–1749.
- Jet Propulsion Laboratory, 2004, The Advanced Spaceborne Thermal Emission and Reflection Radiometer: California Institute of Technology,.
- Kamal, M., Phinn, S., and Johansen, K., 2015, Object-based approach for multi-scale mangrove composition mapping using multi-resolution image datasets: Remote Sensing, v. 7, p. 4753–4783.
- Knight, J.F., Tolcser, B.P., Corcoran, J.M., and Rampi, L.P., 2013, The effects of data selection and thematic detail on the accuracy of high spatial resolution wetland classifications: Photogrammetric Engineering & Remote Sensing, v. 79, p. 613–623.
- Knipling, E.B., 1970, Physical and physiological basis for the reflectance of visible and near-infrared radiation from vegetation: Remote sensing of environment, v. 1, p. 155–159.
- Kruse, F.A., 2002, Combined SWIR and LWIR mineral mapping using MASTER/ASTER: Geoscience and Remote Sensing Symposium, IEEE International, v. 4, p. 2267–2269.
- Link, P.K., and Janecke, S.U., 1999, Geology of East-Central Idaho: Geologic Roadlogs for the Big and Little Lost River, Lemhi, and Salmon River Valleys: Guidebook to the Geology of Eastern Idaho, p. 295–334.
- Manakos, I., Manevski, K., Kalaitzidis, C., and Edler, D., 2011, Comparison between atmospheric correction modules on the basis of Worldview-2 imagery and in situ spectroradiometric measurements: EARSeL SIG Imaging Spectroscopy Workshop, p. 1–12.
- Mandanici, E., and Bitelli, G., 2016, Preliminary Comparison of Sentinel-2 and Landsat 8

- Imagery for a Combined Use: Remote Sensing, v. 8, p. 1014.
- Matthews, N.A., 2008, Aerial and close-range photogrammetric technology: providing resource documentation, interpretation, and preservation: US Department of the Interior, Bureau of Land Management.
- McCaffrey, R., King, R.W., Payne, S.J., and Lancaster, M., 2013, Active tectonics of northwestern US inferred from GPS-derived surface velocities: Journal of Geophysical Research: Solid Earth, v. 118, p. 709–723.
- McIntyre, D.H., and Hobbs, S.W., 1987, Geologic map of the Challis quadrangle, Custer and Lemhi Counties, Idaho: Department of the Interior, U.S. Geological Survey.
- Van der Meer, F.D., Van der Werff, H.M.A., and Van Ruitenbeek, F.J.A., 2014, Potential of ESA's Sentinel-2 for geological applications: Remote Sensing of Environment, v. 148, p. 124–133.
- MicroImages Inc., 2015, Broadband Vegetation Indices: Remote Sensing of Environment 34: 71-73.
- Mielke, C., Boesche, N.K., Rogass, C., Segl, K., and Kaufmann, H., 2014, Multi-and hyperspectral satellite sensors for mineral exploration, new applications to the SENTINEL-2 and ENMAP mission: EARSeL 34th Symposium Proceedings, p. 16–20.
- Mielke, C., Bösche, N.K., Rogass, C., Segl, K., Gauert, C., and Kaufmann, H., 2014, Potential applications of the Sentinel-2 multispectral sensor and the Enmap hyperspectral sensor in mineral exploration: EARSeL Proceedings, v. 13, p. 93–102.
- Ninomiya, Y., 2004, Lithologic mapping with multispectral ASTER TIR and SWIR data: Remote Sensing, International Society for Optics and Photonics, p. 180–190.

- Ninomiya, Y., and Fu, B., 2010, Regional scale lithologic mapping in western Tibet using ASTER thermal infrared multispectral data: *International Archives of the Photogrammetry, Remote Sensing and Spatial Information Science*, v. 38, p. 454–458.
- Ninomiya, Y., Fu, B., and Cudahy, T.J., 2005, Detecting lithology with Advanced Spaceborne Thermal Emission and Reflection Radiometer (ASTER) multispectral thermal infrared “radiance-at-sensor” data: *Remote Sensing of Environment*, v. 99, p. 127–139.
- Pavlis, T.L., and Mason, K.A., 2017, *The New World of 3D Geologic Mapping: GSA Today*, v. 27.
- Payne, S.J., McCaffrey, R., King, R.W., and Kattenhorn, S.A., 2012, A new interpretation of deformation rates in the Snake River Plain and adjacent basin and range regions based on GPS measurements: *Geophysical Journal International*, v. 189, p. 101–122.
- Payne, S.J., Zollweg, J.E., and Rodgers, D.W., 2004, Stress triggering of conjugate normal faulting: Late aftershocks of the 1983 Ms 7.3 Borah Peak, Idaho, earthquake: *Bulletin of the Seismological Society of America*, v. 94, p. 828–844, doi: 10.1785/0120030122.
- Pierce, K.L., and Morgan, L.A., 2009, Is the track of the Yellowstone hotspot driven by a deep mantle plume?—Review of volcanism, faulting, and uplift in light of new data: *Journal of Volcanology and Geothermal Research*, v. 188, p. 1–25.
- Potter, C.S., and Li, S., 2014, High Resolution Mapping of Soils and Landforms for the Desert Renewable Energy Conservation Plan (DRECP): National Aeronautics and

Space Administration.

- Pour, A.B., and Hashim, M., 2012, The application of ASTER remote sensing data to porphyry copper and epithermal gold deposits: *Ore Geology Reviews*, v. 44, p. 1–9, doi: 10.1016/j.oregeorev.2011.09.009.
- Puetz, A.M., Lee, K., and Olsen, R.C., 2009, WorldView-2 data simulation and analysis results: *SPIE Defense, Security, and Sensing, International Society for Optics and Photonics*, p. 73340U–73340U.
- Qiu, J.-T., Zhang, C., and Hu, X., 2015, Integration of concentration-area fractal modeling and spectral angle mapper for ferric iron alteration mapping and uranium exploration in the Xiemisitan Area, NW China: *Remote Sensing*, v. 7, p. 13878–13894.
- Remondino, F., Barazzetti, L., Nex, F., Scaioni, M., and Sarazzi, D., 2011, UAV photogrammetry for mapping and 3d modeling—current status and future perspectives: *International Archives of the Photogrammetry, Remote Sensing and Spatial Information Sciences*, v. 38, p. C22.
- Rodgers, D.W., Ore, H.T., Bobo, R.T., McQuarrie, N., and Zentner, N., 2002, Extension and subsidence of the eastern Snake River Plain, Idaho: Tectonic and Magmatic Evolution of the Snake River Plain Volcanic Province: *Idaho Geological Survey Bulletin*, v. 30, p. 121–155.
- Rowan, L.C., 1998, Analysis of simulated advanced spaceborne thermal emission and reflection (ASTER) radiometer data of the Iron Hill, Colorado, study area for mapping lithologies: *Journal of Geophysical Research: Atmospheres*, v. 103, p. 32291–32306.

- Rowan, L.C., and Mars, J.C., 2003, Lithologic mapping in the Mountain Pass, California area using Advanced Spaceborne Thermal Emission and Reflection Radiometer (ASTER) data: *Remote Sensing of Environment*, v. 84, p. 350–366, doi: 10.1016/S0034-4257(02)00127-X.
- Ruisi, Z., Min, Z., and Jianping, C., 2011, Study on geological structural interpretation based on Worldview-2 remote sensing image and its implementation: *Procedia Environmental Sciences*, v. 10, p. 653–659.
- Senske, D.A., Head, J.W., Stofan, E.R., and Campbell, D.B., 1991, Geology and structure of Beta Regio, Venus: Results from Arecibo radar imaging: *Geophysical Research Letters*, v. 18, p. 1159–1162.
- Siebert, S., and Teizer, J., 2014, Mobile 3D mapping for surveying earthwork projects using an Unmanned Aerial Vehicle (UAV) system: *Automation in Construction*, v. 41, p. 1–14.
- Strand, E.K., Bunting, S.C., and Farris, C., 2013, Fine-scale remote sensing applications to support vegetation and fire management planning and implementation: *NPS Report*, p. 3.
- Susong, D.D., Janecke, S.U., and Bruhn, R.L., 1990, Structure of a fault segment boundary in the Lost River fault zone, Idaho, and possible effect on the 1983 Borah Peak earthquake rupture: *Bulletin of the Seismological Society of America*, v. 80, p. 57–68.
- Swetnam, T.L., Guertin, D.P., Kimoto, A., and Canfield, E., 2013, Riparian vegetation characterization of the Lower Santa Cruz River and Ciénega Creek through remotely sensed multi-sensor data fusion: *Pima County Regional Flood Control District*.

- Tagestad, J.D., and Downs, J.L., 2007, Landscape Measures of Rangeland Condition in the Bureau of Land Management Owyhee Pilot Project: Shrub Canopy Mapping, Vegetation Classification, and Detection of Anomalous Land Areas: Pacific Northwest National Laboratory and Environmental Molecular Sciences Laboratory.
- Tarantino, C., Lovergine, F., Pasquariello, G., Adamo, M., Blonda, P., and Tomaselli, V., 2012, 8-band image data processing of the worldview-2 satellite in a wide area of applications: INTECH Open Access Publisher.
- United States Census Bureau, 2015, Population Facts for Custer County, Idaho: QuickFacts.
- Upadhyay, P., Kumar, A., Roy, P.S., Ghosh, S.K., and Gilbert, I., 2012, Effect on specific crop mapping using WorldView-2 multispectral add-on bands: soft classification approach: *Journal of Applied Remote Sensing*, v. 6, p. 63521–63524.
- van der Werff, H., and van der Meer, F., 2016, Sentinel-2A MSI and Landsat 8 OLI provide data continuity for geological remote sensing: *Remote Sensing*, v. 8, p. 883.
- van der Werff, H., and van der Meer, F., 2015, Sentinel-2 for mapping iron absorption feature parameters: *Remote Sensing*, v. 7, p. 12635–12653.
- Westoby, M.J., Brasington, J., Glasser, N.F., Hambrey, M.J., and Reynolds, J.M., 2012, “Structure-from-Motion” photogrammetry: A low-cost, effective tool for geoscience applications: *Geomorphology*, v. 179, p. 300–314.
- Yu, Q., Gong, P., Clinton, N., Biging, G., Kelly, M., and Schirokauer, D., 2006, Object-based detailed vegetation classification with airborne high spatial resolution remote sensing imagery: *Photogrammetric Engineering & Remote Sensing*, v. 72, p. 799–811.

Zhang, X., Pazner, M., and Duke, N., 2007, Lithologic and mineral information extraction for gold exploration using ASTER data in the south Chocolate Mountains (California): ISPRS Journal of Photogrammetry and Remote Sensing, v. 62, p. 271–282.